

**MOLECULAR DYNAMIC SIMULATION OF THERMO-MECHANICAL  
PROPERTIES OF ULTRA-THIN POLY(METHYL METHACRYLATE) FILMS**

A Dissertation

by

CARLOS ARDENIS SILVA HERNANDEZ

Submitted to the Office of Graduate Studies of  
Texas A&M University  
in partial fulfillment of the requirements for the degree of

DOCTOR OF PHILOSOPHY

May 2010

Major Subject: Mechanical Engineering

**MOLECULAR DYNAMIC SIMULATION OF THERMO-MECHANICAL  
PROPERTIES OF ULTRA-THIN POLY(METHYL METHACRYLATE) FILMS**

A Dissertation

by

CARLOS ARDENIS SILVA HERNANDEZ

Submitted to the Office of Graduate Studies of  
Texas A&M University  
in partial fulfillment of the requirements for the degree of

DOCTOR OF PHILOSOPHY

Approved by:

Co-Chairs of Committee,	Tahir Çagin
	Ed Marotta
Committee Members,	Jaime Grunlan
	Anastasia Muliana
Head of Department,	Dennis O'Neal

May 2010

Major Subject: Mechanical Engineering

## ABSTRACT

Molecular Dynamic Simulation of Thermo-Mechanical Properties of Ultra-Thin  
Poly(Methyl Methacrylate) Films. (May 2010)

Carlos Ardenis Silva Hernandez, B.S., IUPFAN; M.S., Texas A&M University

Co-Chairs of Advisory Committee: Dr. Tahir Çagin  
Dr. Ed Marotta

The thermal conductivity of PMMA films with thicknesses from 5 to 50 nanometers and layered over a treated silicon substrate is explored numerically by the application of the reverse non-equilibrium molecular dynamics (NEMD) technique and the development of a coarse-grained model for PMMA, which allows for the simulation time of hundreds of nanoseconds required for the study of large polymer systems.

The results showed a constant average thermal conductivity of 0.135 W/m\_K for films thickness ranging from 15 to 50 nm, while films under 15 nm in thickness showed a reduction of 30% in their conductivity. It was also observed that polymer samples with a degree of polymerization equal to 25% of the entanglement length had 50% less thermal conductivity than films made of longer chains. The temperature profiles through the films thickness were as predicted by the Fourier equation of heat transfer.

The relative agreement between the thermal conductivity from experiments (0.212 W/m\_K for bulk PMMA) and the results from this investigation shows that with the proper interpretation of results, the coarse-grained NEMD is a useful technique to study transport coefficients in systems at larger nano scales.

## DEDICATION

To my *mother*, for *believing*. And understanding that grandchildren have to wait until I finish school.

To my *father*, for *inspiring*. You are greatly missed.

To my *brother*, for *supporting*. Graduate school can be funded on a student salary but it is a lot easier if you know you are always covered.

To *Ed* and *Tahir*, for *guiding*. And for their patience, put to the test after several semesters hearing “*this is it! I graduate this semester*”

To *all others*. The ones who came and left, who are too many to remember; and the ones who came and stayed, because they are too precious to forget.

## TABLE OF CONTENTS

	Page
ABSTRACT .....	iii
DEDICATION .....	iv
TABLE OF CONTENTS .....	v
LIST OF FIGURES .....	viii
LIST OF TABLES .....	x
1. INTRODUCTION.....	1
1.1 Atomistic Simulations and Thermo-mechanical Properties.....	1
1.2 Length and Time Scales .....	3
1.3 Current Status of the Question .....	4
1.4 Objective .....	10
1.5 Overview .....	10
2. MOLECULAR DYNAMICS SIMULATION.....	12
2.1 Introduction .....	12
2.2 Molecular Dynamics and Monte Carlo Methods .....	12
2.3 Statistical Ensembles.....	13
2.3.1 Isothermal-Isobaric Ensemble or (NpT) .....	14
2.3.2 Isoenthalpic-Isobaric Ensemble (NpH).....	15
2.4 Force Fields .....	16
2.5 Thermodynamic Properties from MD .....	21
2.6 Software for MD Simulations .....	22
3. COARSE GRAINED MOLECULAR DYNAMICS .....	24
3.1 Introduction .....	24
3.2 Literature Review .....	24
3.3 Coarse Grained Parameterization.....	28
3.3.1 Bead Representations .....	28
3.3.2 Force Field.....	31
3.3.3 Results and Refinement of the CG Force Field.....	39
3.3.3.1 Results from the 2k Samples.....	41

	Page
3.3.3.2 CG Force Field Refinement .....	44
3.3.3.3 Results from the 18k Samples .....	48
3.4 Atom-to-bead and Bead-to-atom Mapping Algorithms .....	53
3.5 Summary of Results and Final Parameters .....	56
4. HEAT CONDUCTION IN SOLIDS .....	59
4.1 Introduction .....	59
4.2 Literature Review .....	59
4.3 MD Simulations and Thermal Conductivity .....	67
4.3.1 The Green-Kubo Formulation .....	68
4.3.2 Non-equilibrium MD Simulations .....	71
4.4 Proposed Approach .....	72
4.4.1 Energy Gradient .....	72
4.4.2 One-dimensional Analysis of Heat Flux Through a Wall with Heat Generation.....	74
4.4.3 Entropy and Interpretation of Results .....	77
5. SAMPLE GENERATION, CONDITIONING AND NUMERICAL PROCEDURE .....	79
5.1 Introduction .....	79
5.2 Sample Generation: The Amorphous Builder .....	79
5.3 Sample Conditioning.....	83
5.3.1 Coarse Grained Models .....	83
5.3.2 Substrate and Free-surface .....	84
5.3.3 Conditioning Procedure.....	87
5.4 Sample Dynamics.....	92
5.4.1 Energy Gradient .....	96
5.4.2 Data Generated.....	99
6. RESULTS AND ANALYSIS .....	100
6.1 Introduction .....	100
6.2 Temperature Profiles .....	100
6.3 Thermal Conductivity .....	106
6.4 Energy .....	111

	Page
7. CONCLUSIONS.....	114
7.1 Summary .....	114
7.2 Conclusions .....	115
REFERENCES.....	117
APPENDIX.....	127
VITA .....	145

## LIST OF FIGURES

FIGURE	Page
1 Change in the vibrational spectra of nanoclusters as a function of number of atoms.....	6
2 PMMA monomer .....	7
3 Bonded interactions described by classical MD force fields .....	18
4 CG-PMMA model: 6-beads .....	29
5 CG-PMMA models: 4a/b, 3a/b and 2 beads .....	30
6 Bonds and angles for the 4-beads models. ....	31
7 Angles and bonds statistical distribution for the 6-bead and 2-bead models .....	34
8 Statistical distribution for the angle between beads 1-2-3 on the 6-beads model as a function of the center of bead 3.....	36
9 Bead rotation for van der Waals forces estimation .....	37
10 Curve fitting for van der Waals interaction energy.....	38
11 Variation of density as function of pressure for PMMA.....	43
12 Change in density with pressure of the 6-bead model for different L-J potentials .....	46
13 6-beads model density as a function of pressure (left) and temperature (right) before (blue) and after (red) refining of the van der Waals parameters .....	46
14 CG models selection.....	48
15 Change in density as a function of pressure for the 3a bead model.....	51
16 Time evolution of radial distribution function for the 6 bead CG model ..	52



FIGURE	Page
17 Bead-to-atom restoration process.....	54
18 Original and restore atomistic description a PMMA chain.....	56
19 Temperature distribution on a wall with uniform heat generation $q'''$ .....	75
20 The 4-bead CG model of PMMA.....	84
21 Simulation to estimate the bead-SiO <sub>2</sub> substrate interaction.....	85
22 The Lennard-Jones wall potentials at the substrate and free surface.....	87
23 f50 sample (50nm) in a non-periodic unwrapped representation, showing the hot particles added to the substrate.....	90
24 Variation of energy with respect to time on a NPH simulation.....	94
25 Heat balance on the polymer film during NpH simulation.....	96
26 Temperature profiles for the f50 sample.....	101
27 Shifted temperature profiles for the f50 sample.....	102
28 Temperature profiles and curve fit for the f37 sample.....	104
29 Temperature profiles and curve fit for the f5 sample.....	104
30 Thermal conductivity as a function of film thickness.....	107
31 Thermal conductivity of the f15 sample as a function of the degree of polymerization.....	108
32 Experimental thermal conductivity of PMMA film samples by Kim [71]	109
33 Density of film samples as a function of thickness.....	110
34 Kinetic energy as a function of thickness for the f50 sample, 15 ns.....	111
35 Potential energy as a function of thickness for the f50 sample, 15 ns.....	112
36 Kinetic and potential energies as a function of thickness for the f10 sample, 15 ns.....	113

**LIST OF TABLES**

TABLE		Page
1	Run time for 1000 ps of both MD (atomistic) and CG-MD. 2k sample ....	42
2	MD results for the 2k samples and from Sane et al. 2001 [8].....	43
3	Numerical results from MD. 2k samples .....	47
4	Run time for the 18k samples.....	50
5	Numerical results from MD. 18k samples .....	51
6	Bond parameters for the CG force field.....	57
7	Angle parameters for the CG force field.....	57
8	Pair parameters for the CG force field .....	58
9	Summary of film samples generated with the Amorphous Builder .....	82
10	Summary of film samples after decompression .....	89
11	Coarse grained MD simulation performance on <i>Hydra</i> supercomputer ....	93
12	Change in energy with time and temperature for the NpH simulations.....	95
13	Calculated thermal conductivities for the PMMA films. ....	108

## 1. INTRODUCTION

### 1.1 Atomistic Simulations and Thermo-mechanical Properties

One of the common denominators of most sciences is the search for a connection between the observable, macroscopic behavior and the fundamental laws governing said behavior at the most elemental level. Physics is perhaps the most known example of a pursue for a *theory of everything* able to link the Newtonian laws of the observable universe and the unusual particle behavior predicted by quantum mechanics.

Material science is also advancing towards a more comprehensive understanding of how the elemental particles and structures affect the properties of a given substance. It was barely over a century ago that the fundamental structure of matter began to be discovered and up to that point, material science was based on experiments and trial and error. Few decades later, with the development of quantum mechanics and the birth of computer science, the first simulations of simple atomic ensembles showed that numerical prediction of physical behavior was possible and the gap between theory and experiments began to reduce. The exponential growth of computer power and the improvement of the models that represent atoms allowed for simulations of more complex systems, showing a true potential for *numerical experiments* as a tool to narrow down the number of possibilities to try out in the laboratory.

The current state of the art in both computer power and simulation techniques allow for research of complex, evolved systems; but nonetheless, there still are definite limits to what can be done in a computer simulation. One of the limits is closely related

---

This dissertation follows the style of ASME Journal of Heat Transfer.

to the computer power available: the bigger the computer, the bigger the system and the longer the simulation that can be ran. We are still *climbing* the slope in which computational chemistry investigators are likely waiting for the next development on processors or memory technology to start running virtual models they have thought of few years in advance. Another, more definite limit has to do with the current *brute force* approach to computer simulations. Even if we were able to simulate a single biological cell in a computer system big enough to contain the description of every single subatomic particle in the cell, the mountain of information produced will be of little practical use. And by no mean the system will be able to model how the cell *lives*.

Molecular dynamic simulations will keep growing in parallel with computer science, but there are problems of interest in computational chemistry that investigators would like to solve today instead of waiting for the computer power to arrive in the future. The increasing interest in nanotechnology and materials research provides a constant stream of questions in which computer simulations are clearly applicable but not fully developed at this point in time. The current challenge, besides selecting within the large number of topics of interest which one to work in, seems to be how to match the constantly changing computer resources available with the optimal simulation technique to investigate a particular problem, so as to put said problem on *this side* of the practical application limit. The current challenge is to find the best approximation to calculate materials properties at a reasonable computer cost.

## 1.2 Length and Time Scales

In order to introduce the problem of scales in the context of the present investigation, we will use as example the computer simulation of polymers. On a given polymer chain, the shortest distance between atoms is the bond length, in the order of  $\sim 1 \text{ \AA}$ . The persistence length, defined as the length over which correlations in the direction of the tangent are lost, is typically around  $\sim 10 \text{ \AA}$  (or 1 nm). The coil diameter, which varies for different polymers, is in the order of  $\sim 100 \text{ \AA}$ . The contour length and other typical measurements of a complete polymer chain can be in the order of thousands of angstroms (hundreds of nanometers) depending on the degree of polymerization ( $N_p$ ) and molecular weight among other parameters. For the simulation of mechanical properties like viscosity, where the degree of polymerization and chain entanglement are important, *several* chains should be consider in the simulation box. A large system also prevents simulation artifacts caused by a simulation box being too small or undesirable effects due to boundary conditions. A simulation of Poly(methyl methacrylate), known also as PMMA, in a box with a 10 nm side, will require the description of more than 140000 individual atoms. The simulation of an element on a Pentium Penryn microchip [1] with a *feature size* of 45 nm will require million of atoms. Models of micron-size crystals or thin films (1 micron = 1000 nm) including the description of every atom, requires hundreds of millions atoms and is beyond the practical application of molecular dynamic simulations. It is obvious the size or length scale of a system is an issue, but it is only half of the problem.

A bigger problem is the broad range of time scales involved in the simulation. The vibration of atomic bonds and angles has a characteristic time of approximately  $\tau \sim 10^{-13}$  s, while changes torsional configurations usually occur with a time constant of  $\omega^{-1} \sim 10^{-11}$  s [2]. The time a polymer coil needs to equilibrate its configuration is at least a factor of the order of  $N_p^2$  larger, resulting in  $\tau \sim 10^{-7}$  to  $10^{-4}$  s. When the chain length exceeds the entanglement length for the specific polymer or the temperature of the simulation is close to the glass transition temperature, the relaxation times are even larger. The simulation of few polymer chains with degree of polymerization in the order of the entanglement length will require the solution of the Newton's equations of motion approximately  $10^5$  times ( $10^5$  atoms) in every time step and  $10^5$  time steps just to reach relaxation before any external potential, like a mechanical force or thermal gradient, is imposed to the simulation in order to study the system reaction.

The relaxation times required in computer experiments for fully atomistic systems of a relative larger size involving thermal equilibration at relevant temperatures renders the *brute force* traditional MD impractical. A different approach is required.

### 1.3 Current Status of the Question

Areas of research like MEMS and nanotechnology, where length scales in the order of nanometers, has been attracting the attention of scientists and engineers because at such scales the thermo-mechanical properties of materials differ from bulk properties: molecular structure and interactions, as well as surface effects, are responsible for changes in the behavior of materials and open the possibility for new applications. As an

example, Figure 1 shows how the vibrational spectra of nanoclusters diverge from the bulk behavior when the size of the cluster is reduced to few atoms [3]. The change of properties as a function of size opens the potential for new applications like the use of ultra-thin polymer films (< 100 nm thickness) for large data storage in microelectronics [4] or the development of new semiconductors and thermo-electric materials with high figures of merit [5].

Experimental research in ultra-thin polymer films is challenging due to the difficulties in processing of the samples and measuring in the very small length scales, the later usually requiring indirect methods subject to post processing of data and significant uncertainties. In that regard classical MD simulations has become a suitable tool to aid experimental research as theoretical models, with different configurations and constituent elements, can be tested on the computer and screened out in order to perform the resource consuming experiments only on potentially favorable samples.

A number of studies have demonstrated the application of molecular simulation methods, both MD and Monte Carlo, to predict mechanical properties of polymers. Specifically, PMMA has received a lot of attention because it is inexpensive, amorphous at room conditions and has a relatively high glass transition temperature ( $T_g$ ), making it suitable for many applications. Numerical studies on prediction of PMMA properties like  $T_g$  [6,7] and bulk response [8] have shown good agreement with experimental data, though limitations in size of the computational model and timescale of the simulation are still of concern. Nevertheless, MD simulations have been use to gain insight in the study of local chain dynamics of Poly(propylene) and PMMA [9], the energetic/structural

analysis, cooperativity and stereochemistry on  $T_g$  and bulk properties of Poly(methyl acrylate) and PMMA [10, 11, 12], the  $\alpha$ ,  $\beta$  and stress relaxation modes of PMMA [13, 14] and even the study of the chemical kinetics of thermal degradation through Reactive Molecular Dynamics [15].

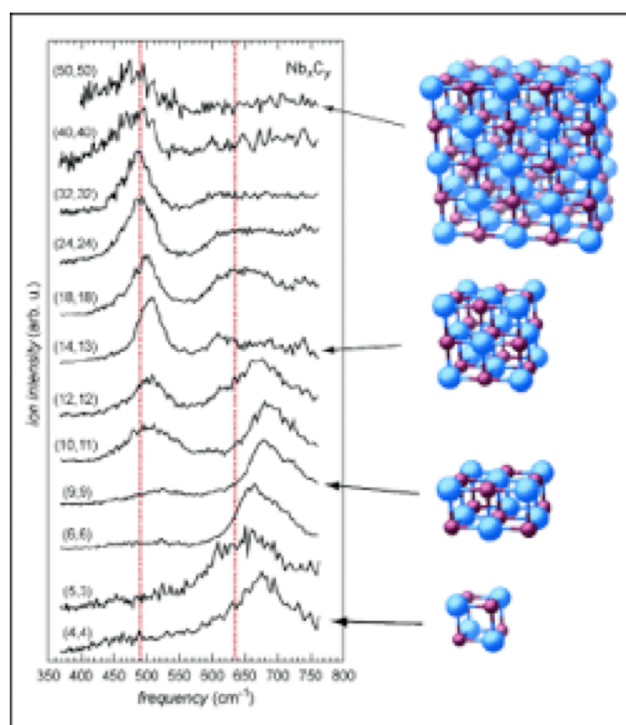


Figure 1: Change in the vibrational spectra of nanoclusters as a function of number of atoms [3].

MD studies of PMMA, whose repeat unit is shown in Figure 2, has also been performed in solutions like PMMA in benzene [16] and blends like PMMA and Poly(tetrafluorethylene) interfaces [17], PMMA and Poly(vinyl alcohol) [18] and PMMA and Poly(ethylene oxide) [19]. Results obtained from these simulations have been encouraging since they agree rather well with laboratory experiments.



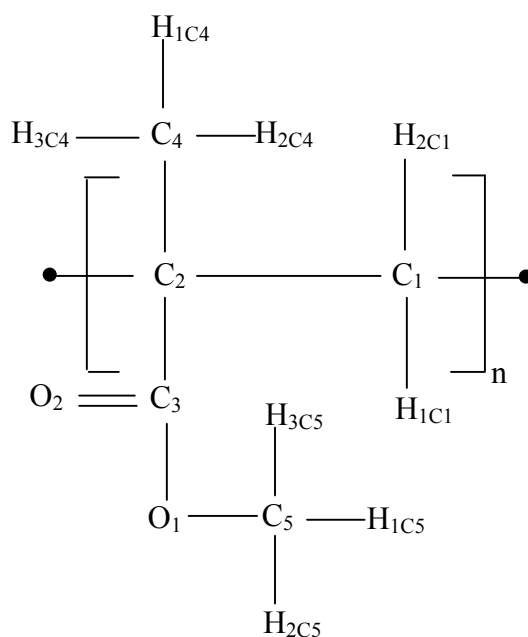


Figure 2: PMMA monomer.

There have been some experimental efforts to study the properties of thin films of PMMA, most of them motivated on the apparent dependence of  $T_g$  on the thickness, stereochemistry of the polymeric film and nature of the substrate. Bulk isotactic PMMA (i-PMMA) exhibit a  $T_g$  near  $60^\circ\text{C}$  while the syndiotactic chain (s-PMMA) shows  $T_g$  around  $130^\circ\text{C}$ . When the thickness of a PMMA film is reduced below 100 nanometers, the difference between  $T_g$ 's of both chain tacticities tends to cancel as  $T_g$  of the i-PMMA increases while that of s-PMMA reduces. Dielectric spectroscopy in PMMA films embedded in aluminum electrodes [20, 21] showed the aforementioned  $T_g$  difference and how the  $\alpha$ - and  $\beta$ -relaxation processes change with film thickness. Studies of PMMA films in silicon oxide, gold-covered silicon and freely standing films [22] replicated the

same behavior and showed the influence of the substrate in  $T_g$ : In free standing PMMA films the  $T_g$  reduction begins with thickness around 100nm while films on a substrate show constant  $T_g$  down to 30nm thickness. Other experimental efforts studied the effect of film hydration level [23] and the influence of nanoparticles on the morphology of thin films [24].

Even though there is clear experimental evidence of the change in  $T_g$  and other properties as the thickness of PMMA films is reduced to nanometer scale, a limited number of numerical studies on polymeric thin films were found in literature. MD simulations have been used to give possible explanations for the change in properties but the calculations were performed using a limited-size unit cell under periodic boundary condition.

The key problem is that a model with a 3-D periodic boundary condition cannot capture all the dynamics of a thin film. A film, and specially a polymeric film, would be properly modeled as a system with a periodic 2-D boundary condition in the in-plane coordinates and a finite dimension (thickness) in the through-plane coordinate; however, such model would require a very large number of molecules and would be computationally demanding. A thin film with thickness of 40nm represented by a 20x20x40nm cell with 2-D periodic boundary condition on the 20nm sides will contain  $1.82 \times 10^6$  atoms thicknesses over 100nm will triple these requirements, pushing the limits of feasible MD simulations.

A proposed solution for the *size of the model* problem is the use of a technique called coarse-grain molecular dynamics (CG MD). This technique originated from MD

studies on bio-molecules like DNA [25] or the representation of Malto-Oligosaccharides and water solutions [26] among many others. Molecules with such complex structures limited MD simulations with fully atomistic description and therefore structural units like a glucose monomer or a water molecule were represented with only few (or even one) *super-atoms* or *beads*. This representation reduced the number of total atoms in the system by an order of magnitude while retaining most of the atomistic effects that play a role in the dynamics of interest, thus creating a bridge between the atomistic description of MD and observable macroscopic behavior. On the downside, a CG model is particular of each material and no general procedure is available to develop such coarse structures, and a force field for the CG model needs to be developed before attempting any MD simulation.

CGMD has been successfully applied in several fields of material science like the study dynamic failures [27] or diffusion phenomena in polymers [28]. In these investigations, the proper description of the physics behind the object of study required model sizing beyond the limits of conventional MD. The study of thermal transport on polymeric thin films is also a field that could benefit from the application of CG MD to model large samples and macroscopically observable phenomena.

The amount of investigations in this particular area is limited and it is the goal of the present study to fulfill this gap in the research literature.

## 1.4 Objective

The objective of this work is to determine the thermal conductivity ( $k$ ) in ultra thin films of PMMA with thicknesses ranging from 5 to 50nm and to study the effect of the film thickness in the thermal transport coefficient. We also want to provide insight on the physical phenomena affecting the specific heat at constant pressure, the coefficient of thermal expansion and the bulk compliance. To this effect a computational modeling procedure based on a CG MD simulation will be developed to predict the thermo-mechanical properties of the polymer within the geometric constraint of a thin film. The effect of the film thickness on the properties and how they differ from the bulk properties will be also investigated.

The combination of a coarse grain (CG) model of PMMA with the implementation of computer code to calculate thermal transport would allow for MD simulations large enough to realistically represent the proposed ultra-thin films and the study of their thermo-mechanical properties.

## 1.5 Overview

A general review of the theory of molecular dynamics simulations is presented in Section 2. This section includes literature review, applications and limitations of the method. Section 3 introduces the formalism of coarse-grained modeling of large systems and the procedure followed to developed CG models for PMMA, as well as a description of the tools used for mapping between atomistic and CG representations. Section 4 presents the details of the thermal conductivity simulation, the methods currently found

in published literature and the approach used in this work. The step-by-step procedure followed to construct, condition and simulate the PMMA film models is presented in Section 5; while Section 6 presents the result for mechanical and thermal properties of the PMMA films, compare them to experimental values from literature, and explore further in the advantages and limitations of the CG modeling. Section 7 presents the concluding remarks and further questions arising from the present study. A literature survey on recent experimental investigations in the area of thin films of PMMA is presented in the Appendix.

## 2. MOLECULAR DYNAMICS SIMULATION

### 2.1 Introduction

In this section, the description of the Molecular Dynamics and Monte Carlo methods for molecular simulation are presented. MC methods are briefly described as most of the work in this investigation is based on MD simulations, which are presented in a more detailed manner. The section contains the description of the statistical ensembles and force fields used in the MD simulation of the PMMA films, and concludes with a short explanation on how to calculate properties from the simulation and the software platforms used in this work.

### 2.2 Molecular Dynamics and Monte Carlo Methods

Molecular Dynamics (MD) and Monte Carlo methods are forms of computer algorithms commonly used in the simulation of ensembles of particles with known interaction such as atoms and molecules. In MD, atoms and molecules are allowed to interact by approximating their physics through a *force field* and by solving the equations of motion, so that snapshots of the atomic structures and their evolution in time can be obtained allowing for the calculation of physical properties. Since no experimental technique can provide access to the timescales and motion with atomic resolution, MD simulations are informally referred to as virtual microscopy [29].

The Monte Carlo (MC) method is more an algorithm than a simulation technique, and it is based on random sampling to calculate results. This method is used in systems

with a large number of coupled degrees of freedom such as fluids and disordered materials, and when it is infeasible to compute an exact result using a deterministic algorithm. In molecular studies MC methods are used to randomly assign torsion angles that are later tested and selected/discarded to obtain the most *favorable* molecular configurations. MC is also used to solve molecular problems by generating states according to the appropriate Boltzmann probabilities instead of trying to solve the dynamics of the system, thus relying in statistical mechanics (Markov Chain) to generate a new state based on a previous one.

MC is a stochastic method and it is used to study systems in *equilibrium*. For problems involving non-equilibrium phenomena like diffusion, a Dynamic Monte Carlo method [30] can be implemented; however, MD is a better methodology to use.

Molecular dynamics simulation involves the solution of differential equations where time is a variable and is the logical choice for problems where the transport coefficients need to be calculated. MD is therefore the method used in this investigation.

### **2.3 Statistical Ensembles**

In statistical thermodynamics an *ensemble* is an idealization of a large number of copies of a system, considered all at once and where each represents a possible microscopic state the system might be in. If these microscopic states also appear on a single sample - with the same probability- over a long period of time, the system is said to follow the *Ergodic hypothesis*, and is this assumption that allows MD simulations of a single system to produce ensemble averages corresponding to macroscopic properties.

Different macroscopic constraints lead to different types of ensembles. In the *Micro-canonical ensemble* or NVE, all the systems in the ensemble are required to have the same number of particles, volume and total energy and is akin to the simulation of a thermally isolated system in pure Newtonian dynamics. In the *Canonical ensemble* or NVT, all the systems exchange energy with a large heat reservoir so as to maintain a fixed temperature. In the *Grand-canonical ensemble* the exchange of particles is allowed.

In this investigation, there are two ensembles that are of particular interest: The *Isothermal-isobaric ensemble* or NpT used for the calculation of properties at constant pressure, and the *Isoenthalpic-isobaric ensemble*, where the energy is allowed to fluctuate as a response to boundary conditions imposed to the systems.

### 2.3.1 Isothermal-Isobaric Ensemble (NpT)

The NpT ensemble is useful for the study of problems under constant pressure, such as most of chemical reactions. The partition function for this ensemble can be written as a weighted sum of the partition function  $Z(N, V, T)$  of the canonical ensemble

$$\Delta(N, p, T) = \int Z(N, V, T) e^{\left(-\frac{pV}{k_B T}\right)} C dV \quad (1)$$

where  $C$  is a normalization factor and  $k_B$  is the Boltzmann constant. The characteristic state function of this ensemble is the Gibbs free energy

$$G(N, p, T) = -k_B T \ln \Delta(N, p, T) \quad (2)$$



In this investigation the NpT ensemble will be used to calculate the dynamics of the PMMA samples at ambient temperature and pressure while allowing for the volume of the films to fluctuate. The classical implementation of this ensemble uses Nose-Hoover thermostat that slows down or accelerates all particles depending on the sign of difference between the instantaneous kinetic energy of the systems and the desired value given by the imposed temperature. Consequently, the NpT dynamics can be used to condition the samples at the desired ambient temperature but cannot be used when temperature is the desired *response* that one wants to obtain from the system.

### 2.3.2 Isoenthalpic-Isobaric Ensemble (NpH)

The NpH ensemble was introduced in 1980 [31] as a method to model adiabatic systems under constant pressure. Since the volume of the systems is allowed to change, the internal energy of the system is no longer conserved and the energy of the adiabatic contraction/expansion has to be accounted for. The conserved quantity is, consequently, the sum of the kinetic and potential energy of the system plus the boundary work, resulting, which is the enthalpy of the system

$$H = U + pV \quad (3)$$

The characteristic state function of this ensemble is the entropy of the system, calculated from the partition function  $\Gamma(N,p,H)$

$$S(N,p,H) = k_B \ln \Gamma(N,p,H) \quad (4)$$

The implementation of this ensemble in MD has no thermostat controlling the temperature and therefore can be used in *non-equilibrium* MD to obtain the temperature response of the system to an imposed heat flux. The NpH ensemble is used in this investigation to run the dynamics of the virtual experiments where heat is applied to the substrate of the films.

## 2.4 Force Fields

The force field is defined in molecular dynamics as the description of the terms by which the particles in the simulation will interact. This description has the form of potential functions that reproduce, to a certain degree of physical accuracy, the behavior observed at the molecular level. Force fields are usually derived from experimental observations as well as *quantum mechanics* calculations and can range from *hybrid* classical/quantum force fields that explicitly describe the electrons in the system to *all-atom* force fields with parameters for every atom or *coarse-grained* force fields that are usually employed in large systems and long time simulations. Besides the form of the potential, there also specific parameters so that a single potential (*harmonic*, for example) can be applied to the description of the bond interaction of several bond types in a model. Force field potentials are advantageous as they allow a fast and simple calculation of inter-atomic forces, but also have limitations as they are empirical approximations and need to be validated for each specific system.

In this investigation, and in particular in this section, we will describe the characteristics of *all-atom* force fields as these are the ones used for the initial simulation

in this work. The details of the functional form used for the coarse-grained model are given in Section 3.

Force fields in classical MD usually have the descriptions of two types of interactions: the bonded interactions of atoms linked by covalent bonds and the non-bonded term describing the van der Waals and electrostatics interactions.

$$\begin{aligned} E_{\text{bonded}} &= E_B + E_A + E_T + E_I \\ E_{\text{non-bonded}} &= E_{\text{vdw}} + E_Q \end{aligned} \quad (5)$$

The bond stretching ( $E_B$ ) and bending ( $E_A$ ) are usually modeled as harmonic oscillators of the form (for bond stretching)

$$E_B = \frac{1}{2} K_B (r - r_0)^2 \quad (6)$$

where  $r$  is the distance between bonded atoms,  $r_0$  is the bond equilibrium position and  $K_B$  and is a proportionality constant, from experimental observations or quantum calculations, that allows the harmonic potential form to be fitted to different sets of bonded atoms pairs. A different form of the bond potential, from the COMPASS class2 force field [32] is

$$E_B = K_2 (r - r_0)^2 + K_3 (r - r_0)^3 + K_4 (r - r_0)^4 \quad (7)$$

where  $K_2$ ,  $K_3$  and  $K_4$  accounting for the second, third and fourth order influence of the bond distance into the potential energy. COMPASS stands for Condensed-phase Optimized Molecular Potential for Atomistic Simulation Studies and it is an *ab-initio*

force field used for condensed phase of inorganic oxides material. For that particular application a 4<sup>th</sup> order influence of the bond stretch on the potential energy might be important, but for simulation of bead-spring representation of polymer, for example, such potential is computationally expensive and adds little to the approximation of the physical description. The same concept applies to the bond bending  $E_A$ , where the variable is the angle from between two consecutive bonds instead of the inter-atomic distance  $r$ .

The last two terms in the first part of eq. (5) are the torsion ( $E_T$ ) and inversion ( $E_I$ ) potentials, which describe the torsion angle ( $\phi$ ) between bonds and the inversion or *improper* angles ( $\alpha$ ,  $\psi$ ) in 4-atom groups. Figure 3 depicts these interactions along with the bond stretch ( $r$ ) and bending ( $\theta$ )

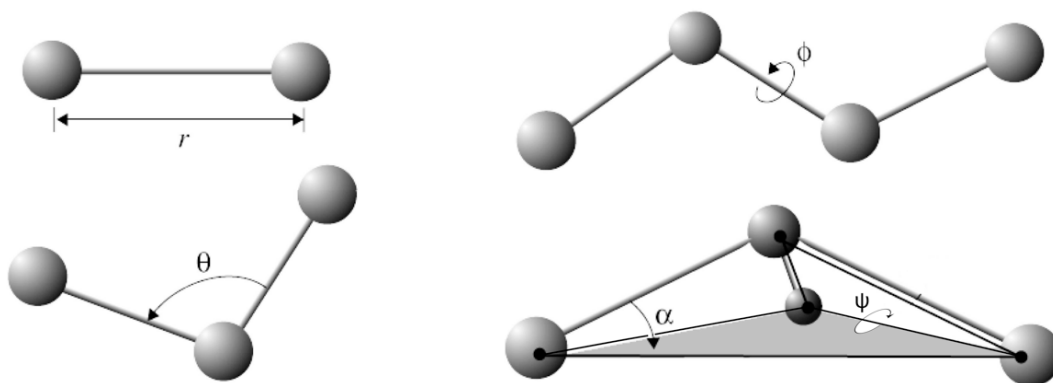


Figure 3: Bonded interactions described by classical MD force fields.

The torsion potential can take the form of an *harmonic* interaction following the equation

$$E_T = K_T [1 + d \cos(n\phi)] \quad (8)$$

where  $K_T$ ,  $d$  and  $n$  are proportionality constants. The COMPASS class2 potential for torsions consists of 6 terms where each is a summation of a series of cosines accounting for middle-bond-torsion, end-bond-torsion, angle-torsion and bond-bond terms. It is evident the complexity of the force field description is dictated by the system one is intended to model and the desired accuracy in the description of the physical phenomena.

The non-bonded atomic interactions in eq. (5) consist of the van der Waals ( $E_{vdw}$ ) and electrostatic ( $E_Q$ ) potentials. Even though these potentials are usually one order of magnitude smaller their bonded counterpart, non-bonded interactions encompass the influence of *all-atoms* within a defined cut-off radius and its calculation during computer simulations require the generations of neighbors lists and accounts for large percentage (more than half) of the total CPU time. In order to reduce the computational resources required for a given model, it is important to select the simpler non-bonded potential offering a good description of the interactions.

When a single charge is assigned to each atom, electrostatic interactions are usually represented by a Coulombic pairwise from

$$E_Q = \frac{Cq_i q_j}{r} \quad (9)$$

where  $q$  are the charges of pairs  $i, j$  respectively and  $C$  is a constant. The formulation for charge dipoles is far more complex and requires calculation of energy, forces and torque.

The van der Waals interaction is the most relevant part of the non-bonded interactions, and usually the most computer-consuming during the MD simulations. In general,  $E_{vdW}$  takes the form of a Lennard-Jones 12-6 potential described by

$$E_{vdW} = 4\epsilon \left[ \left( \frac{\sigma}{r} \right)^{12} - \left( \frac{\sigma}{r} \right)^6 \right] \quad (10)$$

where  $\sigma$  is the diameter or value where  $E_{vdW}$  equals zero,  $\epsilon$  is the depth of the potential well and  $r$  is the distance between the two particles. Alternative forms of the non-bonded interactions are the Buckingham exponential-6 and the Morse potentials described by eq. (11) and (12) respectively:

$$E_{vdW} = A e^{-\frac{r}{\rho}} - \left( \frac{C}{r} \right)^6 \quad (11)$$

$$E_{vdW} = D_o \left[ e^{-2\alpha(r-r_o)} - 2e^{-\alpha(r-r_o)} \right] \quad (12)$$

where  $r$  is the distance between the pair and  $A$ ,  $\rho$ ,  $C$ ,  $D_o$  and  $\alpha$  are all constants, defined to yield a good fit between the potential used in the computer simulation and the real, observable behavior of the atoms or molecules.

A comprehensive list of the force fields used in classical MD can be found in [33].

## 2.5 Thermodynamic Properties from MD

MD simulation can describe the dynamics of many types of systems under different sets of imposed conditions. For each one of these a set properties can be estimated ranging from static properties as density to dynamic, non-equilibrium properties like diffusion coefficients. The detailed formulation of how to calculate the properties is usually extensive, dependent on the system nature and can be found in classical MD literature, consequently is left outside of this section for brevity. We will limit this section to the basic equation used for the calculation of the thermodynamic properties on the PMMA samples, both in atomistic and coarse grained representations.

The density change as a function of temperature was used to calculate the coefficient of thermal expansion (CTE) while the density change with respect to pressure was used to estimate compressibility ( $K_T$ ) of the PMMA samples, calculated from:

$$CTE = -\frac{1}{\rho} \left( \frac{\partial \rho}{\partial T} \right) \quad (13)$$

$$K_T = \frac{1}{\rho} \left( \frac{\partial \rho}{\partial P} \right) \quad (14)$$

The constant-pressure specific heat ( $C_p$ ) was calculated using the total energy change as function of temperature with the data obtained from temperature annealing cycles at constant atmospheric pressure.

$$C_p = \left( \frac{\partial E}{\partial T} \right) \quad (15)$$

## 2.6 Software for MD Simulations

There is a very extensive list of software platform that can be used for MD simulations. A comprehensive list is available in [34]. In this investigation, two platforms were used for the simulation of PMMA films: Materials Studio and LAMMPS.

Materials Studio [35] is a software environment with a graphic user interface developed by Accelrys Inc. and is an updated version of the Cerius2 platform. Materials Studio runs in Microsoft Windows environment and is perhaps the most popular commercial software for molecular modeling and simulation providing outstanding visualizations, quantum calculation tools, classical MD simulations with COMPASS, CVFF, PCFF Dreiding and Universal force fields plus a series of statistical tools for post processing. Even though this program has many advantages, there are *licensing* limitations when it runs in parallel systems over a large number of processors. Moreover, many of the tools available in the program are not necessarily applicable to our specific polymer system. We used Materials Studio for the generation of the PMMA samples through the *Amorphous Builder* module.

LAMMPS [36] is an open-source, classical molecular dynamics code that model ensemble of particles in any state and ranging from atomic, polymeric, biological, coarse grained and granular systems. It is designed for parallel computers that can compile C++ and supports MPI message-passing library. LAMMPS algorithm is based on the spatial decomposition of the simulation domain and has been used to run systems up to millions of particles in top supercomputers as the 65000-processors IBM Blue Gene Light in Lawrence Livermore National Laboratory.



LAMMPS integrates Newton's equations of motion for collection of particles that interact via short/long range forces and with a variety of initial and boundary conditions. LAMMPS' capability of implementing a user-defined force field represents one of the main reasons why this code was selected. LAMMPS performance on large multi-processor simulations was the other reason, as it is expected the bigger film samples will require several processors in order to run in a reasonable amount of physical time.

### 3. COARSE GRAINED MOLECULAR DYNAMICS

#### 3.1 Introduction

This section presents the details of the coarse-grained (CG) molecular dynamics simulation. The methodologies commonly found in published literature are introduced, as well as the details of the procedure followed in this work to obtain the bead representation of PMMA. The results from the CG models are then compared to those from MD simulation of fully atomistic descriptions of PMMA. The summary of the parameters for the PMMA coarse models concludes the section.

#### 3.2 Literature Review

Atomistic simulations are the best way to explore materials properties, but the size and time scales required in the modeling of some applications, like the study of polymer systems or bio-molecules, renders these simulations too resource-expensive and non-practical. The continuous improvement in computer technology allows for a steady increase in MD capability to handle large problems, but if one desires to push the simulation limits without waiting for the next computer breakthrough, then the logical thing to do is to simplify the models so that properties can be calculated with the lesser amount of calculations.

One of the first attempts to simplify large systems was the *united atoms* approach where the hydrogen atoms of CH, CH<sub>2</sub> and CH<sub>3</sub> molecules are collapsed into the corresponding carbon atoms, allowing for simulations that are about one order of

magnitude longer than an explicit atomic system of comparable size [37]. A more generic model is the Kremer-Grest [38] or *bead-spring* model proposed in 1985, where a single bead replaces each monomer thus retaining only the most basic features of a polymer chain but allowing for much faster/larger simulations. The Kremer-Grest model has been used to investigate numerous problems in polymer physics such as the relaxation in polymer solutions and rheological properties of complex fluids, proving the applicability of coarse representations to solve physical problems. Based on these successful results Bennemann et al. [39] proposed a refined version of the model in 1998, in which the chains contain N identical monomers and all monomers, bonded and non-bonded, interact through a truncated and shifted Lennar-Jones potential defined as

$$E_{vdW} = 4\varepsilon \left[ \left( \frac{\sigma}{r} \right)^{12} - \left( \frac{\sigma}{r} \right)^6 \right] + C(r_{cut}) \quad (16)$$

where  $\varepsilon$  and  $\sigma$  are the depth of the potential well and the distance where the potential is zero, respectively, and  $r$  is the inter-monomer distance, with  $r_{cut}$  being the cut-off distance equal to  $2^{1/6}\sigma$ . For distance above the cut-off the interaction is 0. Neighbor monomers along the chain interact through finitely extendible nonlinear elastic (FENE) potential described as

$$E_{FENE} = -(33.75)\varepsilon \ln \left[ 1 - \left( \frac{r}{1.5\sigma} \right)^2 \right] \quad (17)$$

The idea of Bennemann et al. was to include most of the attractive part of the van der Waals potential so that simulations of thermodynamic processes like phase behavior of

polymer solutions and thin films with film-air interface could be modeled without the need to modify the CG representation. This model had been used extensively to study the reduction of glass transition in polymer films [39, 40], the effect of solid interfaces, both smooth and amorphous [41] and dynamics of polymer in confined geometries [42-44].

An alternative approach to the bead-spring models is to trace the trajectories of fully atomistic simulations and derive the coarse-grained model parameters from statistical data. This concept was introduced in 1998 by Tshöp et al. [45, 46] in the study of Bisphenol-A polycarbonate (BPA-PC). Tshöp et al. divided the monomer in two spheres, one representing the isopropylidene group and the other representing the carbonate group; they obtained the sphere and force field parameters by following the general procedure:

- Select a temperature  $T$
- Generate long atomistic chains as random walks
- Determine the positions of the geometrical center of the two groups (beads) during fully atomistic simulations
- Generate the probability distributions for distances ( $l$ ), angles ( $\alpha$ ), torsions ( $\varphi$ ), etc.
- Calculate the Boltzmann factors of the generalized intra-chain interaction potential  $E$  using the proportionality (as example, for the bond distance  $l$ )

$$P(l) \propto \exp\left\{\frac{-E_l(l)}{k_B T}\right\} \quad (18)$$

- Repeat the above steps for different temperatures
- Run melt simulations with the above simplified model adjust inter-chain van der Waals potential until experimental density is recovered.

Results from simulations using the previous methodology showed a good agreement with experimental results obtained from neutron scattering and viscosimetric data. They also showed a minimal effect of temperature on the parameters for bonded beads as well as a flat torsion angle distribution, indicating torsion interaction between beads have no effect on the resulting CG structure. The advantage of this method is that once the bead centers are selected, there are no parameters to *adjust* as the bonded interaction factors are calculated directly from statistical distributions, rendering a CG model that offers a better representation of the atomistic system.

A similar CG methodology has been used in the study of bio-molecules. The MARITNI force field [47, 48] for example, was developed for the CG simulation of large lipid layer systems and has been recently extended to model proteins. Molinero et al [26] developed a M3B force field for the study of malto-oligosaccharides in water mixtures by dividing the monomer in 3 beads, each one located in *carbon centers* (carbon atoms) that were of relevant importance describing the chain topology. The results from this study showed very good agreement with experimental data on the helical distribution of the chain as well as glass transition temperatures of the polymer

and its water mixtures. A methodology for reverse mapping was also presented showing that the atomistic structure could be recover from the coarse grained model. The overall improvement in simulation speed of the M3B CG model over fully atomistic was  $\sim 7000$  times, mainly due to the substitution of the Ewald summation for van der Waals potential by the less computer-intensive Spline approximation allowed with the CG model.

### **3.3 Coarse Grained Parameterization**

There is no general formulation to construct a coarse grain model from fully atomistic description. The size of the model and the properties of interest are the key parameters defining the coarse grain strategy, which is mostly related to the number of atoms per bead and the position of the beads. The PMMA monomer would be ideally represented by 3 or 2 beads making CG-PMMA model one order of magnitude smaller than fully atomistic description (ratio of 15:2). The beads would be located either in the position of the center of mass of the group of atoms each bead replaces or in the position of the atom that best represent the topology of the polymeric chain.

#### *3.3.1 Bead Representations*

The PMMA repeating unit, showed in Figure 1, consists of 15 atoms distributed in the C-C backbone, the methyl and the methacrylate side groups. The presence of 8 H atoms suggests initial coarsening by collapsing the H atoms into the corresponding C atoms, following the unified atom model. The procedure naturally follows by reducing the side

groups into the backbone and finally collapsing the backbone itself, hence representing the entire monomer unit by a single bead. However, such representation cannot carry tacticity information and fails to represent the topology of the PMMA chain, potentially limiting the model to include, for example, the plasticizing effect of the long methacrylate group. For the purposes of the present work, the one-bead-per-monomer representation was considered too simplistic and therefore not investigated.

Figure 4 shows the schematic of the first CG model in which the PMMA repeating unit is reduced to from 15 atoms to 6 beads. All H and the O atom in the O=C double bond were collapsed into their corresponding C atoms. The resulting beads have mass and charge equal to the sum of the masses and charges of the respective atoms. The centers of the beads were assigned at the position of the C atoms with the exception of bead 4, made of single O atom.

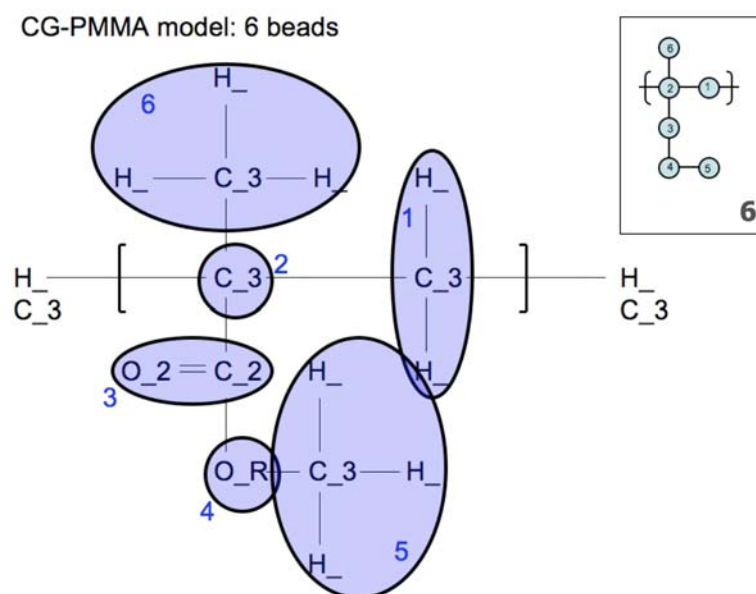


Figure 4: CG-PMMA model: 6-beads.

Using the 6-beads model as a starting point, two models of 4-beads, two of 3-beads and a 2-beads model were generated by further coarsening, as depicted in Figure 5. The masses and charges were assigned as in the 6-beads model but the center of the newly formed beads was assigned at the center of mass (CoM) of the collapsing units. The CoM was selected because in the 6-bead model all beads, except bead 3, had similar molecular weight.

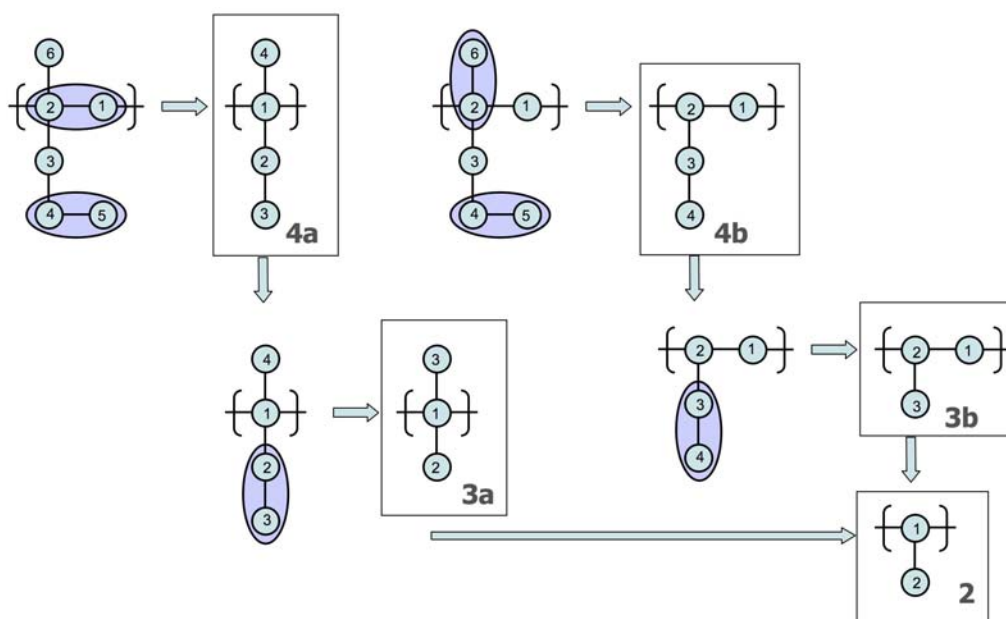


Figure 5: CG-PMMA models: 4a/b, 3a/b and 2 beads.

Once the bead models were defined, the next step was to identify all the parameters to be included in the CG force fields. Figure 6 presents the bonds and angles for both 4-bead models.



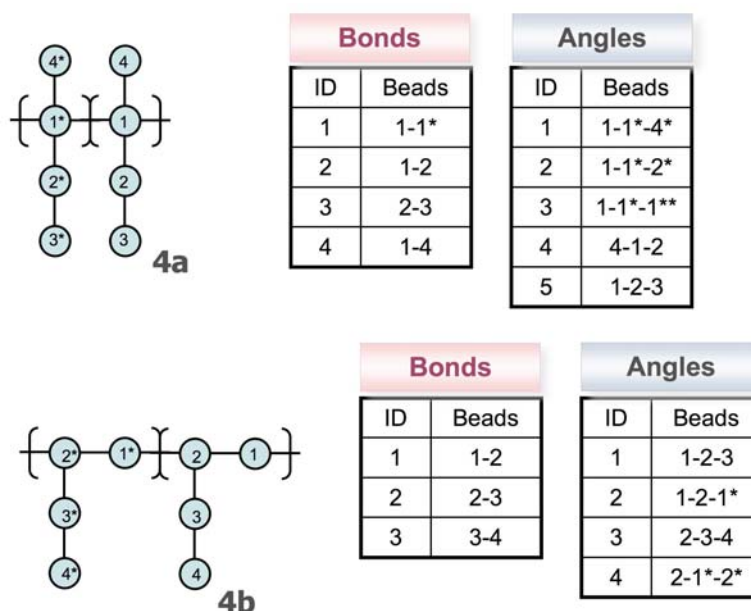


Figure 6: Bonds and angles for the 4-beads models. The fully atomistic description of PMMA has 6 bonds and 10 angle types.

### 3.3.2 Force Field

A main ingredient in MD calculations is the description of forces between atoms –or beads– as they move relative to each other. This description is characterized by a force field, considered a collection of energy terms describing the interactions between the particles of a system. The potential energy,  $E$ , of a generic force field for an arbitrary geometry of molecules is typically characterized by the following terms:

$$E = E_B + E_A + E_T + E_I + E_{vdw} + E_Q \quad (19)$$

The first four terms represents bond interactions, namely, bond stretching ( $E_B$ ), bending ( $E_A$ ), torsion ( $E_T$ ), and inversion ( $E_I$ ). The last two terms represents non-bond

interactions, possessing van der Waals ( $E_{vdw}$ ) and electrostatic ( $E_Q$ ) character. Different functional forms may be used for these energy terms.

The choice of the force field has a major impact in the results of the calculation. A large number of atomistic force fields, optimized to represent different types of physical systems, are available in the literature. In a previous work [8] three force fields commonly used to represent amorphous PMMA, namely, Universal Force Field, Dreiding Force Field [49] and COMPASS [32] were examined and compared to experimental results. It was shown that Dreiding Force Field better represented the cell parameters of the orthorhombic cell of PMMA crystals; therefore Dreiding force field was used in this investigation for the atomistic MD simulations. It is worth noting other force fields that have been used in recent PMMA literature: Polymer Consortium Force Field (PCFF) from MSI/Accelrys [6, 7, 9, 10, 11, 12, 19], AMBER [7, 16] and Constant Valence Force Field (CVFF) [15] among others.

Coarse-grained force fields are not readily available in literature as coarsening is particular of every molecular system. We developed our CG FF using statistical analysis [45] of fully atomistic simulations of PMMA. The details of the simulations follow:

- 17 models of a single PMMA chain with 25 monomers and different tacticity each (13 atactic, 3 syndiotactic and 1 isotactic) were individually simulated on an infinite box.
- Dreiding Force Field was used for bonded interactions, with non-bonded van der Waals forces calculated by the exponential-6 expression [49]. Electrostatic forces

were also included with initial charges estimated by the Gasteiger charge equilibration method.

- Models were subjected to 3 short cycles of temperature annealing from 300 K to 700 K in 85 picoseconds (ps), followed by 1000 ps of NVT dynamics at 300 K. Atoms' trajectory were recorded every 0.1 ps during the last 400 ps of the simulation.
- Models were generated in Material Studio and Cerius2 from Accelrys Software Inc., while simulations were run in LAMMPS.

Using the trajectory from the MD simulation we calculated the bonds and angles at every time step and ran statistical evaluation. Figure 7 shows the typical bond and angle distribution for the 6-bead and 2-bead models.

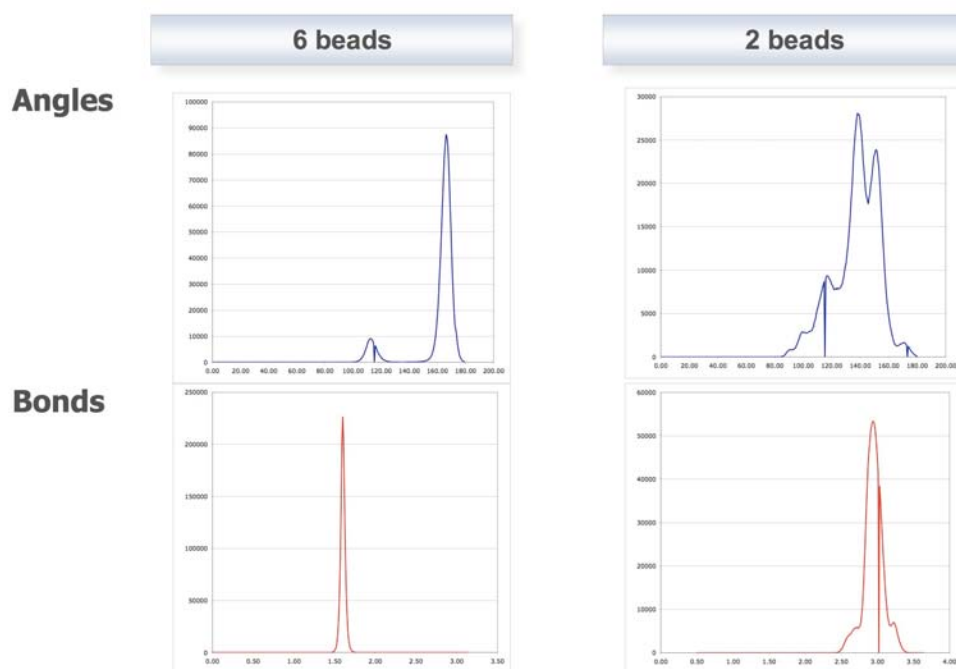


Figure 7: Angles and bonds statistical distribution for the 6-bead and 2-bead models. In general bonds show a sharper distribution. Data tends to spread as coarsening increases.

As the degree of coarsening in the models increases, the concept torsion loses its physical meaning. On a 3-beads model the torsion between 4 consecutive beads affects atoms that are located 7 or more bond-lengths apart, torsionally unrelated at atomistic level. Moreover, the reduction of the degrees of freedom oversimplifies the bead-torsion data, rendering distributions that were too scattered to be useful. Similar results were found in previous investigations from our own research group [50] and published literature on amorphous polymers, where the torsions distribution on coarse-grained models was rather flat [48]. Both torsions ( $E_T$ ) and improper interactions ( $E_I$ ) were neglected in the present work.

Harmonic oscillators were selected for the bond ( $E_B$ ) and angle ( $E_A$ ) portions of the CG-FF, according to the equations:

$$E_B = \frac{1}{2} K_B (r - r_0)^2 \quad (6)$$

$$E_A = \frac{1}{2} K_\theta (\theta - \theta_0)^2 \quad (20)$$

where  $r$  and  $\theta$  are the distance and angle between connected CG beads,  $r_0$  and  $\theta_0$  are the CG bond and angle equilibrium positions; and  $K_B$  and  $K_\theta$  are the constants obtained by fitting Gaussian distribution curves to the trajectory data using the equation:

$$K_i = \frac{RT}{\sigma_i^2} \quad (21)$$

with  $R$  as the universal gas constant,  $T$  the temperature (300 K for our simulations) and  $\sigma$  the standard deviation of the  $i$  set of data.

Gaussian distribution fitted well most of the data with the resulting constants for the 6-beads model being quantitatively similar to those from Dreiding Force Field, and the constants for the coarser models being 1/2 to 1/3 of the Dreiding values. All this was expected as the 6-beads model resembles the united atom model, while the coarser 4, 3 and 2-beads representations reduced the fast atomic modes, weakening the force constants and allowing for bigger simulation time-steps.

The only exception in the Gaussian curve fitting was C=O group, or bead 3, of the 6-beads model. Both C and O atoms have similar molecular weight and therefore we initially assigned the bead 3 center at the CoM. After running MD and evaluating the data we observed the bond angle between bead 3 and the polymer backbone had a wide, bimodal-like distribution that affected the data for the coarser models. This unusual distribution for the 6-beads model was due to the rotation of the C=O double bond

around the methacrylate group axis. To alleviate the problem, the center of bead-3 was re-assigned to the C atom. The resulting distributions had a better Gaussian fit as shown in Figure 8.

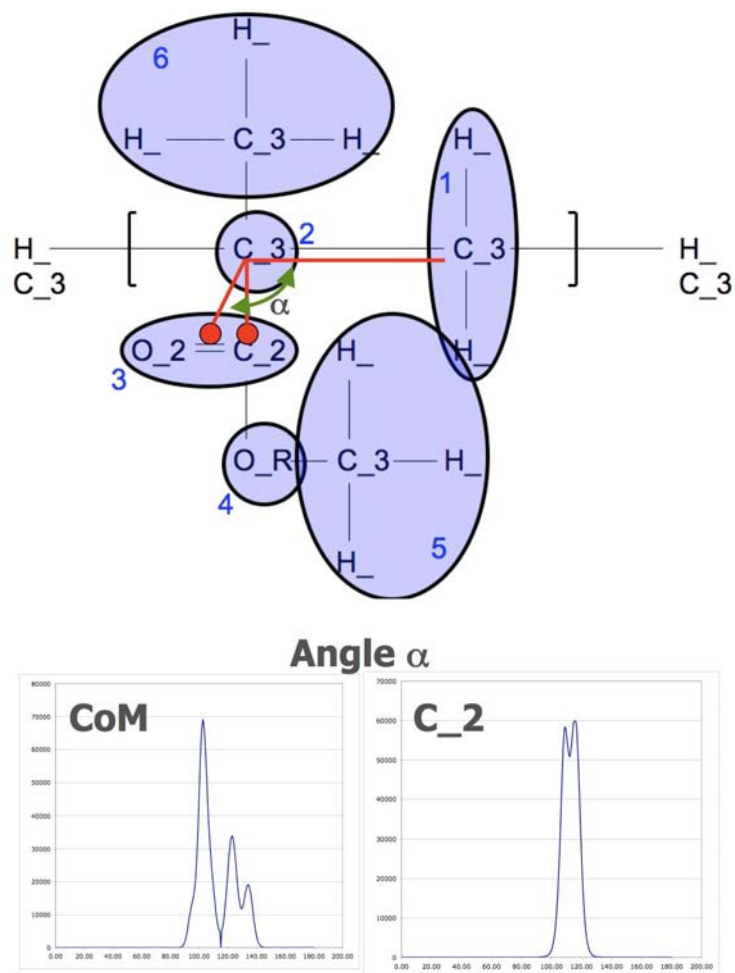


Figure 8: Statistical distribution for the angle between beads 1-2-3 on the 6-beads model as a function of the center of bead 3.

Non-bonded interactions in the form of van der Waals ( $E_{vdW}$ ) and electrostatic ( $E_Q$ ) interactions were included in our CG FF description. Van der Waals forces, which can be calculated by running atomistic MD of all beads pair combinations at a given spacing and totaling  $E_{vdW}$  as function of distance, were calculated here by using a

custom code that systematically rotated each bead around its axis, as depicted in Figure 9, and calculated all atomistic  $E_{vdW}$  using the exponential-6 form of the Dreiding Force Field.

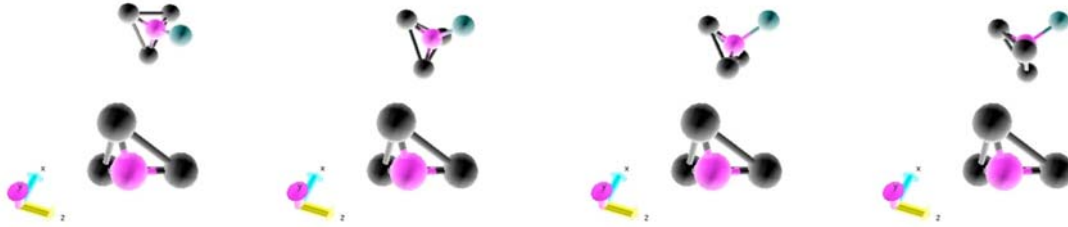


Figure 9: Bead rotation for van der Waals forces estimation.

The procedure was repeated at different bead-to-bead distances and all beads pair combinations. The data collected was analyzed to obtain the median and standard deviation of  $E_{vdW}$  as a function of distance; and finally the data was fitted using both Lennard-Jones 12-6 and Morse expressions for long-range interactions. Figure 10 shows the typical results and curve fitting, with the Morse potential (red line) allowing better fit to the calculated data (blue line) than the Lennard-Jones 12-6 (green line). The Morse expression in eq. (12) permits a better, 3-parameter fitting ( $K_{vdW}$ ,  $\alpha$  and  $r_0$ ) to the data sets and was therefore used as initial approximation for the CG FF.

$$E_{vdW} = K_{vdW} \left[ e^{-2\alpha(r-r_0)} - 2e^{-\alpha(r-r_0)} \right] \quad (12)$$

It is important to clarify that first, we decided for the rotation approach instead of the MD simulation because we wanted to test all the possible relative orientations of the beads in the pairs. The MD approach would likely explore only the preferred orientations for the particular conditions (T, P, etc.) of the dynamics. Second, we regarded the van der Waals constants calculated by the rotation method as a first approximation, with further refining performed by comparing with published literature data after MD simulation of a fully atomistic PMMA system.

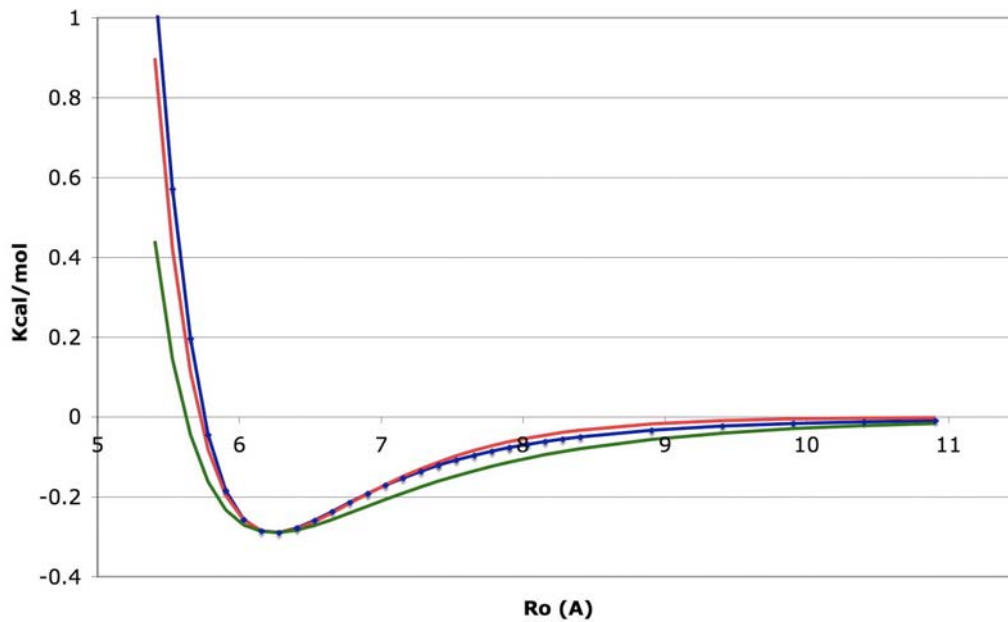


Figure 10: Curve fitting for van der Waals interaction energy. Calculated data showed in blue, Morse in red and Lennard-Jones 12-6 in green.

Electrostatic interaction were calculated using the relation:

$$E_Q = \frac{Cq_i q_j}{r} \quad (9)$$

where C is an energy conversion constant,  $q_i$  and  $q_j$  are the charges in the two atoms and r is the distance. In our coarse grained models, bead charges were calculated by adding



the charges of all the atoms constituent of the bead after a Gasteiger charge equilibration was performed on the atomistic sample. All beads had a single charge.

### *3.3.3 Results and Refinement of the CG Force Field*

Two atomistic samples of PMMA were generated using the amorphous builder module in Materials Studio: one with 3 atactic chains of 50 monomers each for a total of 2256 atoms, and one with 8 atactic chains of 150 monomers each and 18016 atoms. Samples were called 2k and 18k respectively. The 2k sample was used to refine the CG FF and correlate our results with those of Sane et al [8], who used the same polymer structure in their investigation. The larger 18k sample was used for verification of the CG models performance.

Samples were generated with initial density of 0.5 g/cc (experimental bulk density of PMMA is 1.180 g/cc) in a box with 3-D periodic boundary condition. Atomic charges were assigned using Gasteiger equilibration. Both samples were exported to LAMMPS data files and atomistic MD was performed according to the following procedure:

- NVT dynamics at fixed volume and a temperature annealing cycle from 300 K to 700 K and back to 300 K in steps of 50 K. 5 picoseconds (ps) of dynamics were run at each temperature step followed by energy minimization, for a total of 85 ps of dynamics in the cycle. Three temperature cycles were performed.

- The simulation box and atoms' positions were rescaled to reduce the volume of the sample, thus increasing density. Atom's velocities were randomly re-assigned and the complete procedure was repeated.

All simulations ran with Dreiding Force Field and exponential-6 van der Waals interactions. Cut-off was 30 Å for both van der Waals and electrostatic calculations. Simulation box volume was reduced 15% to 5% in each volume cycle and it took approximately 8 cycles to obtain a compressed sample with density slightly above the bulk density. The compressed sample was then subjected to 300 ps of NPT dynamics at 300 K, where pressure was brought down to atmospheric pressure in 10 pressure steps. This procedure prevented the sample to expand uncontrollably when the restriction of fixed volume was removed during the production MD.

PMMA has a molecular weight of entanglement ( $M_e$ ) of 10 kg/mol [51] and therefore the entanglement length  $N_e$  can be approximated to 100 monomers. Using the Rouse model [37] for non-entangled melts and the reptation model for entangled polymers, the relaxation times for the 2k ( $N=50$ ) and the 18k ( $N=150$ ) samples were estimated at 25 and 340 nanoseconds (ns), respectively. During the conditioning process the samples were subjected to a total  $\sim 2.5$  ns (2500 ps) of dynamics. Since the samples were generated in an amorphous configuration and went through high temperature annealing cycles, we regarded the 2k sample as relaxed on a first approximation. This approximation was validated with the 18k samples.

### 3.3.3.1 Results from the 2k Samples

The conditioned 2k sample, with initial density of 1.110 g/cc, was mapped into the 6 CG models previously defined (6, 4a, 4b, 3a, 3b and 2-beads) and subjected to the following set of MD:

- Temperature trip 1: NPT dynamics at atmospheric pressure and a temperature annealing cycle from 300 K to 600 K and back to 300 K in steps of 50 K. 30 picoseconds (ps) of dynamics were run at each temperature step followed by energy minimization, for a total of 390 ps of dynamics in the cycle.
- Pressure trip 1: NPT dynamics at 300 K and a pressure cycle from 1 to 15000 times the atmospheric pressure (1.5 GPa) and back to 1 atm in a total of 17 steps. 30 picoseconds (ps) of dynamics were run at each pressure step followed by energy minimization, for a total of 510 ps of dynamics in the cycle.
- Pressure trip 2: Same as pressure trip 1.
- Temperature trip 2: Same as temperature trip 1.

Atomistic MD simulations were performed with Dreiding Force Field as described in the previous section, while coarse-grained used the CG force fields defined in section 3.3.2. For all the dynamics, the boundary condition used was a 3-D periodic box and the simulation time step was 1 femto second (fs). Total simulation time was 1800 ps, with Table 1 showing the CPU time required for a quad-core workstation (Intel® Xeon®, 2.00 GHz) to run 1000 ps of dynamics in LAMMPS. It can be readily

seen the CPU time requirement improved by one order of magnitude with the reduction of models size obtained through CG.

Table 1: Run time for 1000 ps of both MD (atomistic) and CG-MD. 2k sample.

Model	Number of particles (N)	Run time (hrs)
Atomistic	2256	25.58
6-beads	900	4.85
4a-beads	600	2.05
4b-beads	600	2.45
3a-beads	450	1.28
3b-beads	450	1.90
2-beads	300	0.85

In order to verify the correct implementation of the Dreiding Force Field in the simulation of PMMA in LAMMPS, we compared our atomistic results with those of Sane et al. Figure 11 shows the variation of density as a function of pressure, while Table 2 presents bulk density, coefficient of thermal expansion (CTE) and bulk modulus for both the 2k sample and Sane at al.

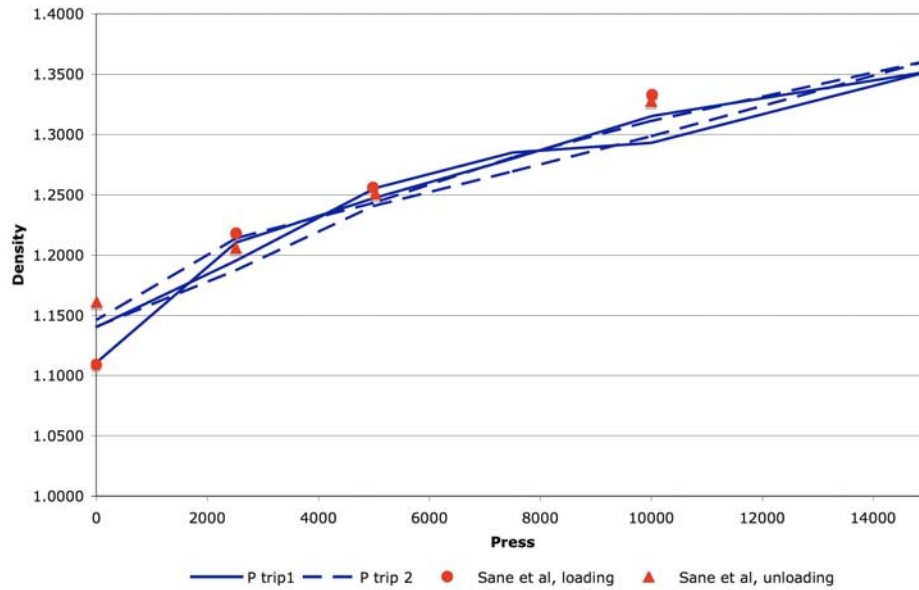


Figure 11: Variation of density as function of pressure for PMMA.

Table 2: MD results for the 2k samples and from Sane et al. 2001 [8].

	2k atomistic sample	Sane et al	Experimental*
Bulk density (g/cc)	1.146	1.162	1.180
CTE (K-1)	$1.92 \times 10^{-4}$	$1 \times 10^{-4}$	$2.53 \times 10^{-4}$
Bulk compliance (GPa-1)	0.115	0.168	0.110

(\*) Data from the Polymer Handbook (1989)

The above results show that our implementation of Dreiding Force Field in LAMMPS was successful as the 2k model results match well the published data. It is interesting to note in Figure 10 that after a first pressure loading/unloading cycle, the density of the sample at atmospheric pressure increased to a value closer to the experimental bulk density. Sane et al. observed this phenomenon and considered the initial pressure cycle part of the sample conditioning. The 2k model showed the same behavior during the pressure trip 1, while the pressure trip 2 returned to the same initial

density. Even though there seems to be a mismatch at 10000 atm (1.0 GPa), an additional loading cycle performed by Sane (not shown in Figure 10) gave high-pressure densities closer to the 2k model results. Nevertheless, lower densities at higher pressures resulted in a lower value for the bulk compliance of the 2k model, which as shown in Table 2, was closer to the experimental value.

### 3.3.3.2 CG Force Field Refinement

The coarse grained CG models gave results within fair to poor agreement to the atomistic simulation. All the models required some extent of refinement that was performed in an iterative process by modifying the non-bonded van der Waals interactions, following the equations:

$$r_o^{m+1} = r_o^m \left( \frac{\rho_{bead}^m}{\rho_{atom}} \right) \quad (23)$$

$$\alpha^{m+1} = \alpha^m \left( \frac{K_{atom}}{K_{bead}^m} \right) \quad (24)$$

$$D_{o_{vdW}}^{m+1} = D_{o_{vdW}}^m \left( \frac{E_{atom}}{E_{bead}^m} \right) \quad (25)$$

where  $D_{o_{vdW}}$ ,  $\alpha$  and  $r_o$  are the van der Waals parameters according to eq. (12),  $\rho$  is the density,  $K$  the bulk compliance and  $E$  the energy of the system. The superscripts  $m$  and  $m+1$  indicate the iteration order. Even though there were three parameters to adjust, they are not linearly independent and therefore most of the refining was done through density

and bulk compliance, according to eq. (23) and (24). Changes in the van der Waals parameters were restricted to  $\pm 2\%$  and were followed by a cycle of CG-MD as described in the previous section.

During the refining process we found that, even though the Morse potential was a closer match for the calculated data on van der Waals potential (Figure 8), it was very difficult to match the density vs. pressure curve of the CG models to the experimental data on PMMA. A better fit was obtained with the traditional Lennard-Jones 12-6 van der Waals potential defined by:

$$E_{vdw} = 4\epsilon \left[ \left( \frac{\sigma}{r} \right)^{12} - \left( \frac{\sigma}{r} \right)^6 \right] \quad (10)$$

where  $\sigma$  is the diameter or value where  $E_{vdw}$  equals zero,  $\epsilon$  is the depth of the potential well and  $r$  is the distance between the two particles. This model yields a stronger attractive potential over the range of 6.5 to 11 Å thus improving the density and bulk compliance of the CG samples, and since it has only 2 adjustable parameters it was easy to obtain a good fit to the experimental values. This iterative process was repeated until agreement was obtained or the model was discarded. As an example, Figure 12 shows the change of density with pressure curve for the 6 bead models at different L-J van der Waals potentials, while Figure 13 presents the change on the density results of the 6-beads CG model before and after refining.

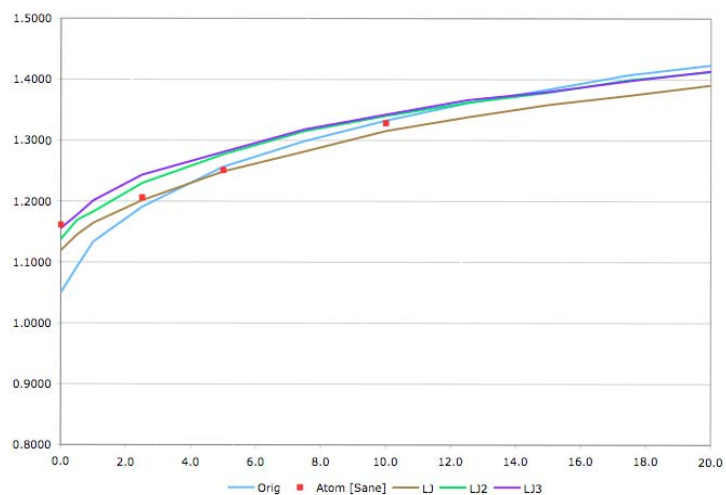


Figure 12: Change in density with pressure of the 6-bead model for different L-J potentials. Atomistic simulation from Sane et al. shown as dots.

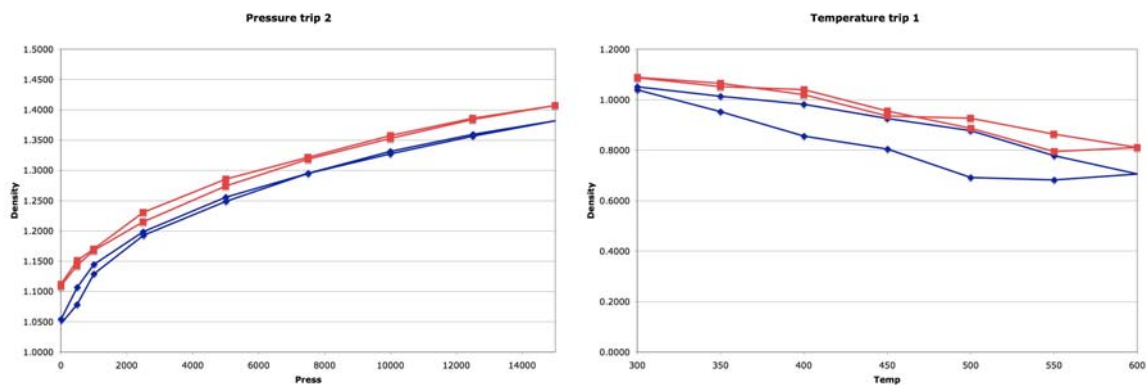


Figure 13: 6-beads model density as a function of pressure (left) and temperature (right) before (blue) and after (red) refining of the van der Waals parameters.

From the six coarse grained models of PMMA initially developed, only the 6, 4b and 3a models yielded good fit with atomistic results by modifying the parameters of the non-bonded interactions. In the other three models, the 4a, 3b and 2 beads, the fitting of



one parameter offset another (as they are interdependent) and agreement with published data was not reached. Table 3 shows the numerical results for all the CG models and atomistic (for comparison purposes). Figure 14 shows the CG models that were selected.

Table 3: Numerical results from MD. 2k samples.

Model	Bulk density (g/cc)	CTE ( $K^{-1}$ )	Bulk comp. ( $GPa^{-1}$ )
Atomistic	1.146	$1.92 \times 10^{-4}$	0.115
6 beads	1.158	$5.31 \times 10^{-4}$	0.161
4a-beads	1.151	$3.57 \times 10^{-4}$	0.206
4b-beads	1.158	$4.34 \times 10^{-4}$	0.165
3a-beads	1.139	$5.67 \times 10^{-4}$	0.179
3b-beads	1.140	$3.09 \times 10^{-4}$	0.194
2-beads	1.129	$5.24 \times 10^{-4}$	0.284

CG models 4a, 3b and 2 were considered soft, with density increasing too much as function of pressure, hence their high bulk compliance. Moreover, the density at atmospheric pressure of the 2-bead model was low and could not be increased by adjusting the van der Waals parameters without compromising other results. The CTE was, in general, twice the value of both atomistic and experimental experiments. At this point we cannot explain these results, but they might be related to the fact that bonded interactions parameters in the CG models were calculated by running dynamics at 300 K. The temperature dependency of bond and angle parameters of the CG models was not investigated.

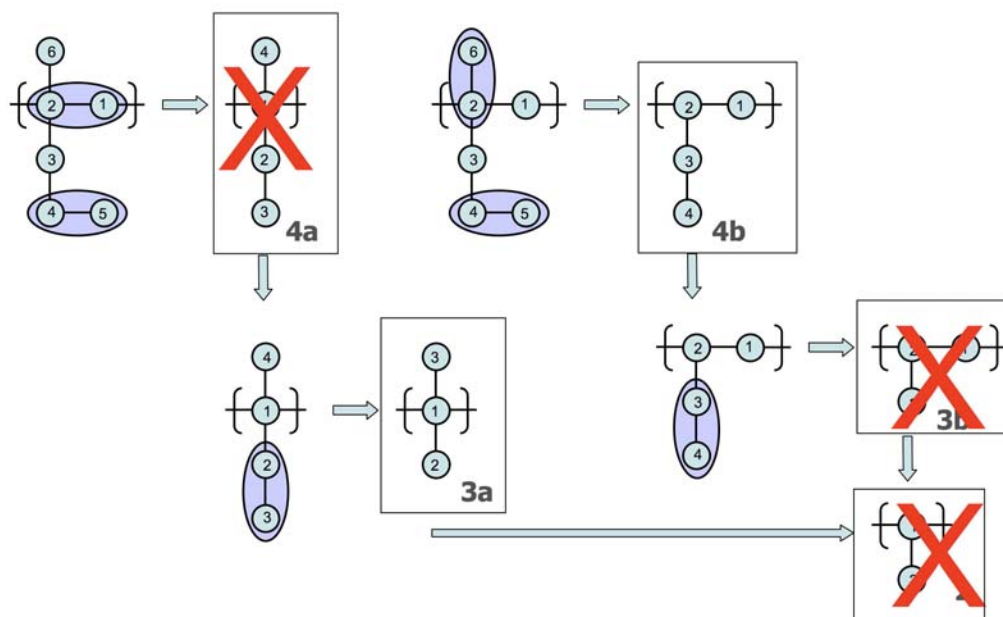


Figure 14: CG models selection.

### 3.3.3.3 Results from the 18k Samples

As mentioned in section 3.3.3, PMMA samples were subjected to 2.5 ns of dynamics during the conditioning process but the reptation model indicates these samples require  $\sim 340$  ns to completely relax. Such a long MD for an atomistic representation would take several days in a cluster-like supercomputer; therefore the 3 coarse-grained models selected in the previous section were implemented by generating 4 copies of the 18k sample:

- Copy 1, generated and conditioned as explained in section 3.3.3
- Copies 2, 3 and 4, generated as in section 3.3.3 then mapped to the 6, 4b and 3a models, respectively, for conditioning. The samples were equilibrated following the same procedure as sample 1, but then the copies was subjected to  $\sim 340$  ns of NPT dynamics at 1 atm and 300 K. The samples were then subjected to pressure

and temperature trips as in section 3.3.4.1 and results were compared to experimental data.

During the long conditioning process the simulation time step was increased to optimize the computational resources. Previous investigations [52] had shown that for a reasonably accurate integration of the equations of motions in a typical all-atom system a time step of 0.5-2.0 fs is required. This is chiefly due to the requirements of the harmonic oscillator use to represent bonded interactions where the frequency is defined as:

$$f = \frac{1}{2\pi} \sqrt{\frac{k}{m}} \quad (26)$$

where  $m$  is the mass (or reduced mass when using two particles) and  $k$  the spring constant. The time step of a simulation is chosen so there is at least six integrations points on a single oscillation of the fastest harmonic oscillator. In the CG models, the spring constant of eq. (26) would be equivalent to  $K_B$  and  $K_\theta$  from eq. (6) and (20), and since these constants reduced and the mass of the beads increased as the degree of coarsening increased, it is expected that frequency of the oscillator will reduce with coarsening, allowing for a larger time step.

The fastest oscillator on the 6, 4b and 3a CG models required time steps of 2.85, 5.67 and 5.73 fs, respectively. Table 4 presents run time and the maximum simulation time step obtained. Conditioning was performed in the Hydra Supercomputer (IBM®

Power5+ processors, 1.9GHz [53] at Texas A&M University, using 16 processors in each run.

Table 4: Run time for the 18k samples. 100 ns of simulation 16 proc MPI parallel simulation.

Model	Number of particles (N)	Run time (hrs)	Time step (fs)	Improv. w.r.t. atom
Copy 1 (atom.)	18016	~ 1000 (*)	1	-
Copy 2 (6)	7200	165.0	2.5	6x
Copy 3 (4b)	4800	46.6	5	21.5x
Copy 4 (3a)	3600	21.1	5	47.4x

(\*) Estimation based on time required for a 2.5 ns dynamics

The combined effect of both the reduction in the number of particles and the increase in time step yielded and overall reduction of computer time of up to 47.4 times the requirements of the fully atomistic simulation. Once the four 18k samples were conditioned, dynamics as described in section 3.3.3.1 were performed to obtain the bulk density, CTE and bulk compliance, with results presented in Table 5.

One important note with respect to the 3a CG model is that during the long dynamics the sample shown a dramatic drop in density after approximately 20 to 25 ns of dynamics at 300 K and atmospheric pressure. After several runs of dynamics at different temperatures, it was found the 3a CG model exhibit melting like behavior at 230 K, temperature at which the density went from  $0.988 \text{ g/cm}^3$  to  $0.316 \text{ g/cm}^3$ . At 330 K the density abruptly reduced to  $0.006 \text{ g/cm}^3$  and the model was deemed unrecoverable. This phase change-like behavior is a consequence of the reduction in the degree of freedom of the model by coarsening, as well as the change in the *free energy space* of

the model due to the curve fitting of the constants for the harmonic oscillators representing the bonded interactions. Figure 15 shows the variations of density with temperature for the 3a CG model, which was discarded for further use. The 6 and 4b and CG were tested up to a temperature of 600 K and they did not show this abnormal behavior.

Table 5: Numerical results from MD. 18k samples.

Model	Bulk density (g/cc)	CTE ( $K^{-1}$ )	Bulk comp. ( $GPa^{-1}$ )
Copy 1 (atom.)*	1.1402	2.01E-04	0.110
Copy 2 (6)	1.1634	5.13E-04	0.154
Copy 3 (4b)	1.1597	3.54E-04	0.157
Copy 4 (3a)	N/A	N/A	N/A

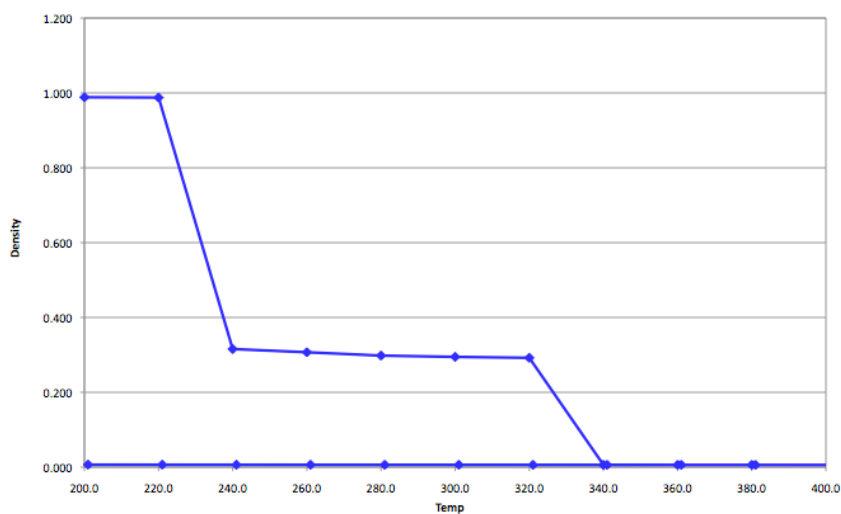


Figure 15: Change in density as a function of pressure for the 3a bead model.

Results in Table 5 show good agreement with the data from Sane et al and the previous 2k samples, indicating that shorter CG MD simulations can provide similar results as the long molecular dynamic runs required by the reptation model to completely relax the PMMA models. This might also be an indication of good implementation of the builder algorithm used to generate the samples, which renders a good amorphous structure to begin with. Figure 16 shows the radial distribution function  $g(r)$  for the 6 bead CG model from 0 to 300 ns every 50 ns, and it can be seen the initial structures are amorphous in nature, as the position of the peaks do not change with time and the shape of the curve is mostly constant. It is important to note all  $g(r)$  curves collapsed to a single curve after 100 ns, indicating the sample was completely relax at this point.

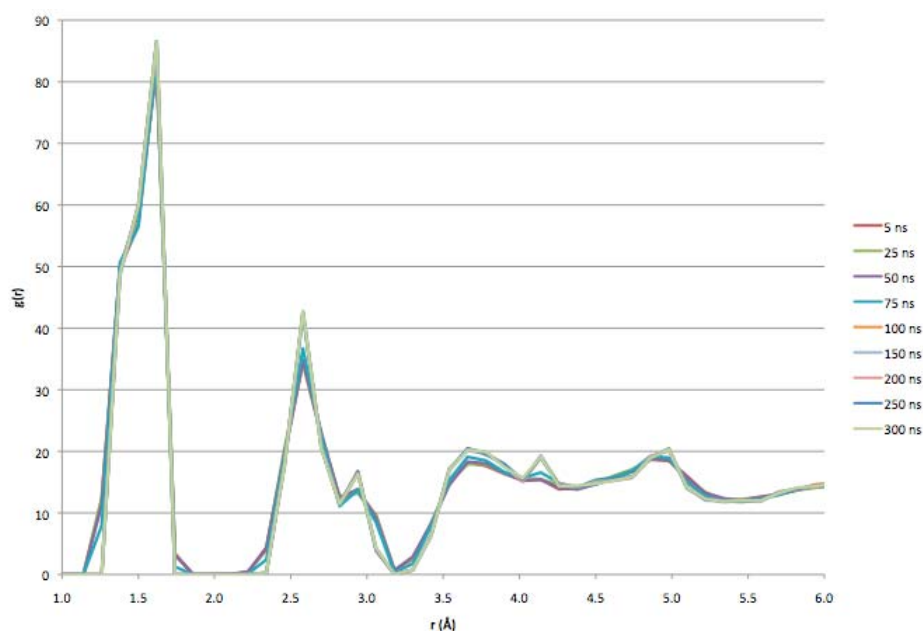


Figure 16: Time evolution of radial distribution function for the 6 bead CG model.

### 3.4 Atom-to-bead and Bead-to-atom Mapping Algorithms

The mapping from atoms-to-beads representations was performed by *collapsing* all the H atoms into the respective C atoms in the 6 CG model, and then by placing beads in the CoM of the groups of atoms in both the 4b and 3a CG models. It is clear then that at any point of the simulation, an atomistic sample can be mapped straightforward into beads if the positions and mass of all the atoms are known.

Mapping from beads-to-atoms is more complex as the coarsening process reduces the information carried by the model and consequently the restoration of the atom's positions requires approximations and in some cases special dynamics. As the degree of coarsening increases, less information is carried and a more inexact atom position restoration is obtained. At the chain level, the CG model carry most of the information needed and the atoms position can be restored with less problem, but at the monomer level, and specifically in the side groups, restoring atoms from a 3a CG model resulted in some cases of atom overlap, which created abnormally large forces during the molecular dynamic simulations of the restores atomic systems.

The procedure used in this investigation was based on vector geometry. Two models of the PMMA monomer were defined such that all bond distances; angles and dihedrals were at their equilibrium position according to the Dreiding FF. Each model corresponded to one of the 2 possible tacticities of the monomer. The beads of the CG model were mapped over these atomistic representations and the direction vectors from beads to atoms calculated. The origin of these direction vectors was always the correspondent bead center and the direction was obtained relative to a *guide vector*,

which usually was aligned with the backbone of the polymer chain. This guide vector was used to construct an orthonormal basis on every bead center, and the direction vectors were rotated in space to match the said basis. Figure 17 shows a schematic of the procedure.

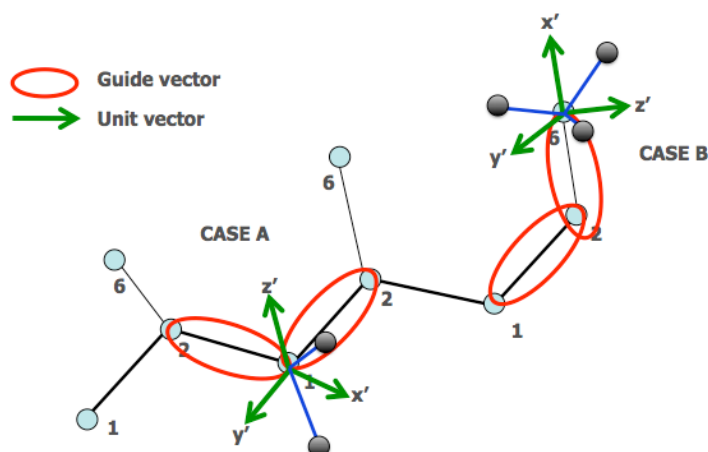


Figure 17: Bead-to-atom restoration process.

In Figure 17, case A, one of the guide vectors from bead 2 (left) to bead 1 was used to define the  $x'$  axis. The second guide vector from bead 2 (right) was used, in conjunction with  $x'$ , to define a plane to which axis  $z'$  has to be perpendicular. Axis  $y'$  was calculated to be perpendicular to both  $x'$  and  $z'$ . With this orthonormal basis the direction vectors of the two H atoms (in dark grey) were rotated and added to bead 1 center in order to obtain the position of the H atoms. In case B, the bead 6 is an *end* bead and therefore the second guide vector used was taken from the backbone of the chain (bead 1 to bead 2) as to guarantee that the restored positions of the 3 H atoms were in the most energetically favorable (lesser energy) configuration. In every monomer the atom's



positions were calculated for both possible tacticities, and the one with bond distances closer to the known atomistic value was selected.

The previous procedure allowed the restoration of atoms' positions with a high degree of accuracy as can be seen in Figure 18 where thin lines describes the original structure of the chain and tubes represent the recovered polymer structure from the 4a CG model. There was, however, an issue with samples containing several chains and higher density, where non-bonded neighbor atoms were prone to overlap and generated abnormal pair forces that render the sample unusable. This problem was observed in around 1.5% of all the atoms restored from the 3a CG model, which was the worst case scenario as the 3 bead model was the one carrying the lesser information about the original chain structure. To work around the problem, a version of LAMMPS with a *truncated* repulsive van de Waals potential was compiled. This allowed to run dynamics in which a strong repulsive force still exists that pushed overlapping atoms apart, but in a controlled manner and without degenerating the sample or creating simulations instabilities beyond recovery. A short run of dynamics, in the order of 100 ps, was enough to restore the overlapping atoms and allow normal dynamics on the sample.

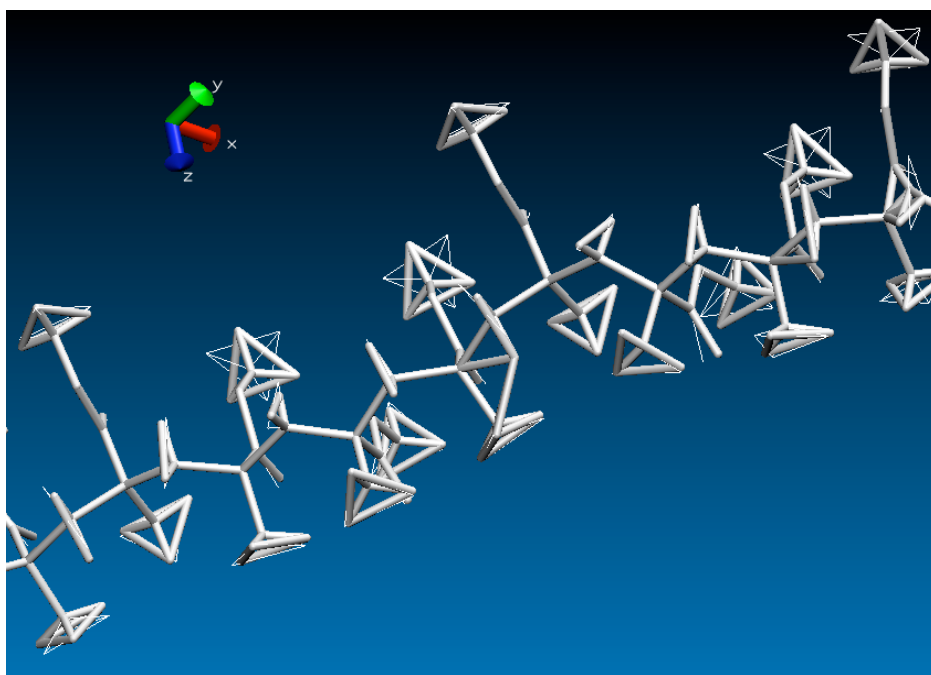


Figure 18: Original and restore atomistic description a PMMA chain.

### 3.5 Summary of Results and Final Parameters

A summary of final parameters for the CG force fields is presented in Tables 6, 7 and 8.

These tables refer to Figures 3 and 4 for bead numbering and notation.

Table 6: Bond parameters for the CG force field.  $K_B$  and  $r_o$  correspond to parameters in eq. (2).

Model	Bond	$r_o$ (Å)	$K_B$
6 Beads	1-2	1.602	493.91
	2-3	1.514	589.08
	3-4	1.347	601.15
	4-5	1.448	679.30
	2-6	1.578	618.09
4b beads	1-2	2.050	216.19
	2-3	2.011	87.27
	3-4	1.835	272.70
3a beads	1-1*	2.659	184.47
	1-2	2.906	90.47
	1-3	2.018	218.30

\* Demarks bead in adjacent monomer

Table 7: Angle parameters for the CG force field.  $K_\theta$  and  $\theta_o$  correspond to parameters in eq. (3).

Model	Angle	$\theta_o$ (rad)	$K_\theta$
6 Beads	1-2-6	1.893	137.86
	1-2-3	1.965	67.77
	1-2-1*	1.846	80.94
	2-1*-1*	2.224	145.56
	6-2-3	1.966	40.71
	2-3-4	2.898	135.68
	3-4-5	2.196	89.91
4b beads	1-2-3	1.388	104.28
	1-2-1*	1.353	87.06
	2-3-4	2.729	49.05
	2-1*-2*	1.842	34.27
3a beads	1-1*3*	2.119	139.2
	1-1*-2*	2.015	97.0
	1-1*-1**	2.771	80.6
	3-1-2	2.247	104.0

\* Demarks bead in adjacent monomer

Table 8: Pair parameters for the CG force field.  $\epsilon$  and  $\sigma$  correspond to parameters in eq. (10). Geometric mixing rule was used to calculate parameter between bead pairs.

Model	Pair	$\epsilon$	$\sigma$
6 Beads	1-1	0.170081	3.749096
	2-2	0.099944	3.444621
	3-3	0.164065	3.956593
	4-4	0.100656	3.009047
	5-5	0.220239	3.818887
4b Beads	1-1	0.182229	3.741522
	2-2	0.347947	4.238085
	3-3	0.175784	3.948600
	4-4	0.284793	4.218887
3a Beads	1-1	0.277676	3.632093
	2-2	0.304457	4.396457
	3-3	0.219484	3.311611

## 4. HEAT CONDUCTION IN SOLIDS

### 4.1 Introduction

This section introduces the formalism of the thermal conduction in solids. The section begins with the classic heat transfer equation in a differential element of an isotropic solid, followed by the nature of the heat carriers (phonons) and the approaches used to account for their effects in the thermal transport at the nano scale. The application of MD simulations in the prediction of thermal transport on nano systems is described, as well as the methodologies found in published literature and the approach followed in this work.

### 4.2 Literature Review

The macroscopic thermal conductivity is defined from Fourier's law of heat flow under non-uniform temperature. The steady state heat flow  $J_q$  is obtained by keeping the system and reservoirs in contact,

$$\vec{J}_q = -\Lambda \vec{\nabla} T \quad (27)$$

where  $\Lambda$  is called the thermal conductivity tensor, and  $\vec{J}_q$  is the heat current produced by the current temperature gradient  $\vec{\nabla} T$ . Fourier's law of heat flow was originally formulated based on experimental observations and can be derived from linear response theory. For isotropic systems, the conventional thermal conductivity  $\lambda$  is given by the average quantity of different directions:

$$\lambda = \frac{1}{3} Tr\Lambda \quad (28)$$

Note that the thermal conductivity calculated here does not include the electronic contribution and no net particle flow persists in the system. For one-dimensional heat transfer along the  $x$ -axis, the Fourier law can be expressed as:

$$q'' = -k \frac{dT}{dx} \quad (29)$$

where  $q''$  is the heat flux by unit of cross-section area,  $k$  is the bulk thermal conductivity and  $T$  the temperature. This law simply states that the heat transfer is proportional to the negative gradient of the temperature and the thermal conductivity of the material.

A more general heat conduction equation can be obtained by performing an energy balance over a differential element. The details of the derivation can be found in most college-level heat transfer textbooks and are omitted here for brevity, but starting with an energy balance over a volume  $V = \Delta x \Delta y \Delta z$ ,

$$\begin{array}{ccccccc} \text{Change in internal} & & \text{Heat conducted} & & \text{Heat conducted} & & \text{Heat generated} \\ \text{energy of material} & & \text{into volume} & & \text{out of volume} & & \text{during time } t \\ \text{within volume during } t & = & \text{during time } t & - & \text{during time } t & + & \text{(C)} \\ \text{(A)} & & \text{(B1)} & & \text{(B2)} & & \end{array}$$

The left hand side term (A) can be expressed as,

$$\frac{dU}{dt} = \Delta x \Delta y \Delta z \rho c \frac{dT}{dt} \quad (30)$$

where  $U$  is the internal energy,  $\rho$  is the density and  $c$  is the specific heat of the element. Terms (B1) and (B2) are obtained by applying the one-dimensional Fourier law, eq. (29) to every dimension. For example, in the x-axis,

$$q_x - q_{x+\Delta x} = -A \frac{dq}{dx} \Delta x = \Delta x \Delta y \Delta z k \frac{d^2 T}{dx^2} \quad (31)$$

where  $A$  is the cross-section area ( $\Delta y \Delta z$ ) and  $q$  were replaced by eq. (29) assuming constant thermal conductivity  $k$ . The term (C) can be expressed as the rate of volumetric heat generation  $q'''$  multiplied by the volume of the element

$$q_{gen} = \Delta x \Delta y \Delta z q''' \quad (32)$$

Combining eq. (30), (31) and (32) for the three-dimensional volume  $V$ , and after simplification and rearrangement, the general heat conduction equation in Cartesian coordinates is defined as

$$\left( \frac{\partial^2 T}{\partial x^2} + \frac{\partial^2 T}{\partial y^2} + \frac{\partial^2 T}{\partial z^2} \right) + \frac{q'''}{k} = \frac{1}{\alpha} \frac{\partial T}{\partial t} \quad (33)$$

where  $\alpha = \rho c / k$  is the thermal diffusivity. In the special case of steady state heat conduction, the right hand side term vanishes and eq. (33) becomes the *Poisson* equation,

$$\left( \frac{\partial^2 T}{\partial x^2} + \frac{\partial^2 T}{\partial y^2} + \frac{\partial^2 T}{\partial z^2} \right) + \frac{q'''}{k} = 0 \quad (34)$$

which can be written for one-dimensional heat transfer as:

$$\frac{d^2 T}{dx^2} + \frac{q'''}{k} = 0 \quad (35)$$

The general heat conduction eq. (33) is a typical parabolic partial differential equation and it is used to describe *diffusion* in various problems like particle diffusion, Brownian motion and modeling of options in financial mathematics, among others. Equation (33) has been proven to provide an accurate description of the heat conduction phenomena in macroscopic systems. However, this equation is based on a *continuum* assumption in which the description of the heat carriers is not included. When the size and/or timescale of the system are comparable to that of the physical mechanisms of heat transport the validity of the Fourier equation is not clear. For example, in electrically insulating materials, the mechanism of heat transfer is lattice vibrations that take the form of quantized elastic waves, or phonons. In electrically conductive materials electrons also participate in the heat transfer. The Fourier equation does not account for these effects and might fail to describe the phenomena at the nano scale. Moreover, the Fourier equation allows for infinite speed of information propagation within the continuum field, which is physically inadmissible [54].

When the characteristic length scale of the system is smaller than phonon mean-free path, an alternative heat transfer model based on the Planck's blackbody radiation theory is used [55]. In this case, the material is considered to be an empty volume with



radiating surfaces from which phonons propagate at a constant velocity, equal to the velocity of sound in the material. The heat flux between the two ends is given by

$$q'' = \sigma(T_1^4 - T_2^4) \quad (36)$$

where  $\sigma$  is the Stefan-Boltzmann constant for phonons and  $T_1, T_2$  the temperatures at the ends. This mode of heat transfer is known as *Ballistic Transport* and is characterized by the absence of phonon-phonon interference and scattering. The scale limit for the application of eq. (36) is known as the *Casimir limit*. Above this limit, sources of thermal resistance such scattering affect the rate of energy transport, thus requiring a combination of both *diffusive* and *ballistic* heat transfer modes.

Several equations can be found in published literature that account in one way or another for heat transfer when the time or length scales of the system are similar in magnitude to that of the heat carriers. The Cattaneo equation [56] for example

$$\bar{q} = -k\nabla T + \tau \frac{\partial \bar{q}}{\partial t} \quad (37)$$

is a modification of the Fourier heat equation that has been upgraded from *parabolic* to *hyperbolic* differential form to solve the problem of the infinite speed of information propagation and whose origins can be traced to the Maxwell's equations of electrodynamics, thus implying the wave nature of heat transport. In this equation  $\tau$  is

the relaxation time  $\tau = \alpha/C$ , with  $C$  being the speed of sound. The hyperbolic heat equation (37) allows for the description of phenomena like thermal resonance and thermal shock [57], where the time scale is so small that diffusion is *limited* by the speed of the carriers; however, this equation is still unable to model the ballistic transport.

The Boltzmann Transport Equation (BTE) can be used to model the heat carriers and is expressed as

$$\frac{\partial f(\mathbf{r}, \mathbf{v}, t)}{\partial t} + \mathbf{v}(\mathbf{r}) \cdot \nabla f(\mathbf{r}, \mathbf{v}, t) = \left( \frac{\partial f(\mathbf{r}, \mathbf{v}, t)}{\partial t} \right)_{\text{scatt}} \quad (38)$$

where  $v$  is the phonon velocity and  $f$  is the distribution of the excitation states of the phonon modes. The function  $f$  takes different forms depending on whether the solution assumes scattering or no-scattering model (the Casimir limit) in its evaluation of the heat flux. The solution of the steady state form of eq. (38) for the phonon distribution function can be integrated using the expression (for the x-axis)

$$q_x = \int v_x f_\omega(x, t) \hbar \omega D(\omega) d\omega \quad (39)$$

where  $v_x$  and  $f_\omega(x, t)$  are the phonon velocities and distribution of states in the x axis,  $D(\omega)$  is the density of states per unit frequency range and  $\hbar \omega$  is the quantized energy associated with a phonon. When eq. (39) is integrated using the definition of thermal conductivity given in eq. (28), the Fourier Law in eq. (29) is obtained.

The effect of the heat carriers can be accounted for by introducing forms of phonon scattering mechanisms in the BTE, and some scattering models for point impurities, normal processes and boundaries has been studied [55, 58]. In the absence of scattering and phonon-phonon interference, the phonon distribution does not follow the statistical behavior and the scattering term of the BTE drops to zero. In this case, the BTE can be used to both derive the Casimir limit phonon distribution function and analyze the ballistic heat transport.

When the characteristic length of a system is in the same order of magnitude as the Casimir limit, both *scattered* and *unscattered* phonons can participate in the heat transport. Forms of the BTE has been developed to account for both transports methods, with the most relevant being the Modified Fourier's Equation [59] and the Equation of Phonon Radiative Transfer (EPRT) [60]. In the macro scale regime, where the thickness of the film is much larger than the phonon scattering-mean free path, EPRT reduces to the Fourier Law. On the other hand, in the micro scale limit, EPRT yields the blackbody radiation law described by eq. (36) at temperatures below the Debye temperature.

The expressions for the heat transfer equation and thermal conductivity previously referenced were developed for crystalline structures and films with defined lattices, both perfect and imperfect, and considering electrons (conductors) or dielectric materials. It was suggested [55] that for materials such as amorphous semiconductors, the elastic description of a solid could be used to solve the phonon-based equations and calculate the heat flux.

In an amorphous glass, the measured thermal conductivity is generally much lower than that of a crystal due to the *structure scattering* [58]. Replacing the known thermal conductivity into the Debye formula

$$k = \frac{1}{3} Cvl \quad (40)$$

where  $C$  is the specific heat and  $l$  the average mean free path, the value of  $l$  can be obtained and shown to be independent of temperature for room temperature or above, and of the order of magnitude of an atomic bond length. At lower temperatures and therefore lower frequencies, the observed mean free path increases and the scattering due to local disorder becomes less relevant as the glass is macroscopically homogeneous. Klemens calculated that thermal conductivity using the equation of kinetic gases and attenuation lengths of both transverse and longitudinal phonon waves

$$k(T) = k(T)_L + k(T)_T \quad (41)$$

where

$$k(T)_L = \frac{AK^2T}{3\pi a\hbar} \int_0^\infty \frac{x^2 e^x}{(e^x - 1)^2} \left\{ 1 + \left( \frac{T}{T_0} \right)^3 x^2 \right\}^{-1} dx \quad (42)$$

$$k(T)_L = 3.29 \frac{AK^2T}{3\pi a\hbar} \quad (43)$$

with eq. (42) being the general case and eq. (43) the limit case of very low temperatures.

For the longitudinal wave contribution

$$k(T)_T = \frac{1}{3} BavC(T) \quad (44)$$

$$k(T)_T = 3.29 \frac{2BK^2T}{3\pi a\hbar} \quad (45)$$

where eq. (44) is the general case and eq. (45) the limit case of very low temperatures. In equations (42) to (45),  $A$  and  $B$  are empirical constants,  $K$  is the Boltzmann constant and  $a$  is the lattice constant. According to this approach, the thermal conductivity of an amorphous glass depends on three empirical constants:  $A$ ,  $B$  and  $T_o$ . These equations showed good agreement when compared to experimental data but that after the empirical constants were fitted.

### 4.3 MD Simulations and Thermal Conductivity

It has been shown that the description of the heat transfer in the micro/nano scale can be non-trivial due to the effect of the heat carriers and boundaries/interfaces. When the size become small, the thermal conductivity is not a property of the material only but also depends on the system dimension and structure [61]. At this scale, heat transfer equations based on the BTE and with the appropriate phonon description are applicable. However, they are not the only approach: Molecular dynamics simulations can be used to describe the heat transfer as the lattice vibrations are explicitly calculated using the interaction energy between the atoms and the equations of motion.

Previous MD studies on the thermal transport have been performed in thin films of Argon molecules [62], diamond [63] and carbon nanotubes [64]. Anomalous heat

conduction in three-dimensional non-linear lattices was recently studied [65] using the Fermi-Pasta-Ulam- $\beta$  model in systems of up to 100nm in size, and it showed divergence of the thermal conductivity with lattice size up to 128 x 128 x 256 lattice sites. These simulations focused on materials with defined lattice structures and therefore reliable results for lattice thermal conductivity were attainable with a few thousand atoms. On an amorphous polymer like PMMA, the physical principle behind thermal transport, i.e. molecular vibrations, is the same but with the additional complexities of an irregular structure, thus requiring the use of larger model size.

Besides lattice structure systems, MD simulation has been successfully used, for example, to study thermal transport on a Lennard-Jones fluid [66], interface thermal resistance and heat conduction between parallel plates separated by a thin layer of liquid Argon [67] and the thermal conductivity of a single polyethylene chain [68]; among many other investigations.

The methodology to calculate thermal transport using MD can be divided in two major groups: The *Green-Kubo* auto correlation function and *non-equilibrium molecular dynamics (NEMD)*.

#### 4.3.1 The Green-Kubo Formulation

This formulation, derived from the linear response theory, relates the dissipation of thermal fluctuations *in an equilibrium system* with its thermal conductivity [63, 64, 69] though the use of the heat flux operator. In MD simulations, the heat current is given by

$$\vec{R} = \sum_i \vec{r}_i h_i \quad (46)$$

$$\vec{J}_q = \frac{d}{dt} \vec{R} \quad (47)$$

where  $h_i$  is the total energy of particle  $i$ , which includes kinetic and potential energies.

For pairwise interactions, it is

$$h_i = \frac{p_i^2}{2m_i} + \frac{1}{2} \sum_j V_{ij} \quad (48)$$

Following the fluctuation–dissipation theorem, the thermal conductivity tensor can be expressed in terms of heat current auto correlation function (HCAFC),

$$\Lambda = \frac{1}{K_B T^2 V} \int_0^\infty dt C_{jj}^q(t) \quad (49)$$

where

$$C_{jj}^q(t) = \langle \vec{J}_q(t); \vec{J}_q(0) \rangle \quad (50)$$

is called the quantum canonical correlation function and  $\langle a; b \rangle$  is defined as

$$\langle a; b \rangle = \frac{1}{\beta} \int_0^\beta d\xi \text{Tr}[\rho \exp(\xi H) a \exp(-\xi H) b] \quad (51)$$

with  $\rho$  defined as the density matrix of the system at equilibrium and  $a, b$  being dynamic operators.

Quantum canonical correlation functions are difficult to evaluate directly and approximations have to be implemented. In the classical limit, the Plank constant  $\hbar$

approaches zero and the canonical correlation reduces to the usual classical correlation function. The classical counterparts of (49) and (50) are

$$\Lambda = \frac{1}{K_B T^2 V} \int_0^\infty dt C_{jj}^c(t) \quad (52)$$

$$C_{jj}^c(t) = \langle \vec{J}_q(t) \vec{J}_q(0) \rangle \quad (53)$$

where  $C_{jj}^c(t)$  is obtained by phase space averaging

$$\langle ab \rangle = \frac{\int d\Gamma \exp(-\beta H) ab}{\int d\Gamma \exp(-\beta H)} \quad (54)$$

The implementation of the Green-Kubo formulation for thermal conductivity calculation on classical MD is not a trivial exercise and in this investigation there is the additional limitation of size of the samples: In order to calculate the thermal conductivity the position, velocity and force of every bead in a given model has to be known at every time-step, thus requiring very large storage capacity, in the order of 100 Gigabytes. Another limitation of the Green-Kubo formulation is that for single chains [68], the analysis of one polymer chain cannot be used to predict the thermal conductivity of other chains with different lengths.



#### 4.3.2 Non-equilibrium MD Simulations

The Green-Kubo formulation required the system to be in equilibrium. When a temperature gradient is applied to a MD simulation, a non-equilibrium condition is created and a heat flux is generated as a response; therefore the Fourier Law can be used to determine thermal conductivity. It is important, however, to first demonstrate the applicability of the Fourier Law as it has been proven to fail near the Casimir limit (for example, in simulation of systems with nano-confined geometries); and second, the steady state or local thermal equilibrium of the system has to be attained [67]. These simulations are similar to real experiments.

A similar approach often referred to as reverse NEMD consists in imposing the heat flux by exchanging kinetic energy between two particles in different regions of the simulation box, thus generating a temperature gradient in the system. This algorithm [70] divides the system in parallel slabs and exchange energy between one of the boundaries and the center slabs, thus creating a periodic heat flux. The main advantage of this approach is evident in cases where the heat flux is difficult to define microscopically as it is the case in anisotropic materials where the directions of both  $\Lambda$  and  $T$  in eq. (27) are not collinear and the thermal conductivity becomes a tensor. For large systems the heat flux calculation required large data storage and computer time. Additional advantages of the reverse-NEMD are [70]:

- Reverse NEMD generally conserves total energy and linear momentum; therefore there is no need for external thermostating.
- No artificial walls are required as hot-cold reservoirs or zero-velocity boundaries.

- The algorithm is easy to implement, the output is a well-defined temperature profile rather than a heat flux, and the method shows rapid convergence.
- Can be applied to calculate shear viscosity if a momentum exchange is imposed rather than an energy exchange.

The application of reverse NEMD has been commonly used in Lennard-Jones fluids whose properties are well known and relaxation times are short. The application on polymeric systems faces the limitations imposed by the large timescales in polymers. Additionally, there is the limitation of a non-periodic boundary in the through-thickness axis of a polymer film. An additional consideration is that this method assumes that the *unphysical* transfer imposed by the exchange is balanced by the *physical* flow. In simulations where the energy swap is too aggressive, the resultant temperature gradient might not be linear, hindering the application of Fourier Law.

#### **4.4 Proposed Approach**

In this investigation, reverse NEMD is the method selected to perform the simulation for the thermal conductivity of the films. The details of the implementation follow.

##### *4.4.1 Energy Gradient*

This work focuses on the MD simulation of PMMA films over a Silicon oxide substrate and with a free surface (air) on top. The thickness of the films varies between 5 and 50 nm and is assumed to be non-periodic in the z-axis direction, with periodic boundary conditions imposed on x and y-axis. The structure of the PMMA is amorphous, with the

degree of polymerization varying from 25 to 300 monomers per chain. The number of particles on the fully atomistic description varies between 18016 atoms to 180080 atoms for the 5 and 50 nm films respectively, and they required relaxation times on the order of 100 nanoseconds. It is readily seen that the calculation of the heat flux current by either the Green-Kubo formulation or equilibrium MD is a paramount task requiring large amounts of storage and computational time.

The approach used here is to impose an energy gradient similar to the reverse NEMD, where an energy flux is the boundary condition and the temperature is the system's response. However, there are key differences with previous works:

- Due to the non-periodic condition through the thickness of the film, exchanging energy between the substrate and center *slabs* will not result in a steady heat flux along the thickness of the film and therefore the exchange has to be between the substrate and the free surface.
- It is difficult to impose an energy sink condition on the free surface, as sink-particles would need to be added consequently affecting the topology of polymer chains near the surface. Additionally, the surface position (film thickness) shows small statistical variations requiring a *moving* energy sink boundary.

To overcome these difficulties the energy gradient is imposed by adding kinetic energy at the substrate through *hot* LJ particles located at the position of the silicon substrate while kinetic energy is removed from *all* polymer particles. When the kinetic energies added and extracted are the same, the energy balance is enforced and the

scheme is equivalent to one-dimensional heat conduction with uniform volumetric heat generation, where the heat flux at the wall (substrate) is equivalent to the heat generated through the solid (polymer film). The approach used in this work would be a *reverse* case in which there is uniform volumetric cooling (or negative heat generation) in the polymer film. The advantage of this method is that the governing equations for the one dimensional heat transfer with heat generation are well studied and therefore, if a steady state temperature profile is obtained, the determination of the thermal conductivity is straightforward. Additionally, only the LJ hot particles needs to be added to the film substrate sample thus minimizing the number of total particles of the system and reducing artifacts that can potentially affect the behavior of the polymer.

#### *4.4.2 One Dimensional Analysis of Heat Flux Through a Wall with Heat Generation*

The general solution of eq. (35) is

$$T = \frac{-q'''}{2k}x^2 + C_1x + C_2 \quad (55)$$

where the integration constants  $C_1$  and  $C_2$  will depend on the boundary conditions. In a plane wall with heat generation and where both surfaces temperatures  $T_{s1}$  and  $T_{s2}$  are equal, the temperature profile shows a symmetrical, quadratic dependence with the thickness of the wall, as shown in Figure 19.

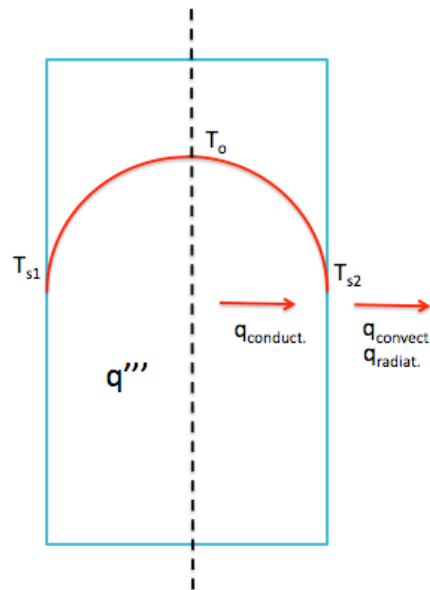


Figure 19: Temperature distribution on a wall with uniform heat generation  $q'''$ .

The temperature at the center,  $T_o$ , is the maximum temperature at the slab, and no heat occurs across the center line (dashed) as the heat generated in a volume element located the center line will diffuse by conduction toward the walls ( $q_{\text{conduct.}}$ ) at lower temperature, and then outside the walls either by convection or radiation. In analyzing the solution of eq. (55), an insulated boundary can be assumed at the centerline. The boundary condition at the wall can be defined as either the temperature  $T_{s2}$  or the surface heat transfer if the heat flux, or the adequate heat transfer mechanism is known.

When applying eq. (55) to our polymer films model, it is clear that if energy is supplied to the substrate and removed in the *exact same amount of energy* throughout the polymer film, then the neat heat flux at the free surface would be zero and therefore an insulated boundary condition can be applied at  $z=L$ , where  $L$  is the film thickness. Is

important to clarify that simulations in this work use a reverse approach where heat is added to the substrate and removed in the polymer volume, instead of generating heat in the volume and removing it from the substrate. At the substrate ( $z=0$ ), the heat flux is known as it the result of the volumetric heat generation, but the heat flux boundary condition was used at the free surface, at the substrate the condition of a known temperature obtained through the MD simulation of the different films is applied. Using boundary conditions for the slab in Figure 19.

$$\left. \frac{\partial T}{\partial x} \right|_{x=L} = 0 \quad \text{and} \quad T|_{x=0} = T_s$$

the solution of eq. (55) becomes

$$T(x) = \frac{-q'''}{2k} x^2 + \frac{q'''L}{k} x + T_s \quad (56)$$

Equation (56) will be used to solve for the thermal conductivity of the PMMA films by setting the thickness in the z-axis (replacing x) and using the known heat removal from the polymer volume as  $q'''$  while  $T_s$  will be the temperature at the substrate. Some implications derived from eq. (56) are:

- The temperature profile from the simulations is expected to show a quadratic dependence with the z-position.

- The thermal conductivity and (negative) heat generation affects the shape of the steady state temperature profile, while the intercept is solely defined by the substrate temperature.
- The gradient of the temperature with respect to  $z$  should approximate 0 at the film surface (insulated boundary condition).
- If a second order polynomial curve fit is applied to the temperature profile, the ratio between the  $z$  and  $z^2$  constant should be equal to  $-2L$ .

#### 4.4.3 Entropy and the Interpretation of Results

A word of caution needs to be added regarding the results from the MD simulation of coarse-grained systems. From the first and second law of thermodynamics, it can be shown that energy of the system follow the relationship

$$dE = TdS - \sum_i X_i dx_i + \sum_j \mu_j dN_j \quad (57)$$

where  $E$  is the energy,  $S$  the entropy,  $X_i$  are the generalized forces corresponding to the external variables  $x_i$ , and  $\mu_j$  are the chemical potentials corresponding to the number of particles  $N$  of type  $j$ . For a system with constant number of particles and boundary work, eq. (57) reduces to

$$dE = TdS - pdV \quad (58)$$

In the CG systems the number of degrees of freedom have been reduced and therefore, the entropy of the system is fundamentally different from the fully atomistic representation. As seen on eq. (58), if we run the MD simulation for atomistic and CG systems where the temperature, volume and pressures are similar and then compare both the results, the calculated values of the energy  $E$  will be different as the entropy of both systems is different and therefore calculated values as the specific heat, thermal expansion coefficients and thermal conductivity may differ from fully atomistic MD simulations. With this in mind, is important to clarify that results from the CG models are expected to be of the same order of magnitude as the atomistic simulations, but a direct comparison is not recommended as the energy maps of the models are different. Nevertheless, comparing results among several CG representations with the same degrees of freedom (i.e. entropy) enable us to capture whether or not there is an effect of the film thickness on the thermal conductivity.



## 5. SAMPLE GENERATION, CONDITIONING AND NUMERICAL PROCEDURE

### 5.1 Introduction

In this section the detailed procedure for film models generation, conditioning and testing is presented. The process begins with the use of the Materials Studio/Cerius2 *Amorphous Builder* module to generate the fully atomistic film samples, followed by the use of custom developed tools to generate the coarse grained models and transfer the data files from Cerius2 to LAMMPS format. Then the description of the parameters used during the MD simulation for conditioning of the samples is presented, as well as the details of the *production MD runs* where the energy gradient is imposed and the temperature profile obtained as a response. The procedure for the calculation of the thermal conductivity as a function of film thickness, as well as some additional considerations, closes this section.

### 5.2 Sample Generation: The Amorphous Builder

The Amorphous Builder (AB) is part of the package of the Materials Studio/Cerius2 modeling software by *Molecular Simulations Inc.* © 1999. A new version of the software called Materials Studio that runs in Windows platform is also available, but for this investigation we used the former Unix platform version.

The AB module allows the building of structures non-periodically as an isolated single or multiple chains, as a 3D-periodic system to represent bulk state, or as a film by

imposing a 2D-periodic condition. The structures are generated by varying the rotatable torsions using either a random method or a rotational isomeric state (RIS) method and finally a *bump check* algorithm is used to control how close together non-bonded interactions are allowed to come when the amorphous structure is being built.

The builder uses as input a base structure/chain usually generated by the *Polymer Builder* module. In this work, the base structure is always a PMMA chain in atactic configuration and with a degree of polymerization (N) ranging from 25 to 300 monomers. The atactic model was selected as it better represents the amorphous nature of the PMMA. Film samples with thickness under 15 nm were generated with a number of chains with N=150, while films with thickness over 15 nm were generated with chains of N=300. The transition thickness at L=15nm was set in order to maintain a similar number of chains across all the samples and also to ease the generation of the amorphous structures with the AB algorithm. At thickness equal 15nm, film samples with chains of N=25, 50, 150 and 300 were generated in order to study the effect, if any, of the degree of polymerization on the heat transfer.

On the AB algorithm, the torsions are calculated by either a Monte Carlo method to assign random values to all torsions, or by one of two RIS methods:

- The RIS ratio where the distribution of torsion angles, angle tolerances and relative frequencies are explicitly defined for each torsion type.
- The RIS energy method where the distribution of torsion angles is calculated using the Boltzmann partition function given the specified RIS temperature and relative energies from the various isomeric states.

A method is specified for each unique rotatable torsion and therefore a combination of the three previous methods can be used on a single chain. In this investigation we used Monte Carlo to randomly assign the angles. For a single chain the assignment of torsion angles is a relatively straightforward task, but for a packed, high density samples, there is a threshold in which most of the torsion angles available would result in the overlap of non-bonded atoms. In order to minimize this problem, two algorithms are implemented within the AB:

- A *bump checking* algorithm in which the minimum non-bond distance allowed is equal to the sum of both atoms van der Waals radii multiplied by a scale factor. This scale factor represent a trade off, as a large relative large number will prevent overlap but make difficult for the AB to find acceptable values for all torsions, potentially inducing the failure of the algorithm. A small value would have the opposite effect, resulting in high frequency of atom overlap and therefore an unstable system.
- A *retry attempts* algorithm in which the number of attempts to find an acceptable angle for each torsion is defined. If a value is not found after the number of attempts, the AB backs up to the previous torsion, sets a new value for the angle, and then tries the *problem* bond again. In high-density samples, when most of the torsions are already set, finding the last torsion might require the AB algorithm to back up several bonds before acceptable values are found. The AB can back up all the way to the beginning of the chain and starts building again, or abort after a specified number of attempts have been made.

Samples of PMMA films were created with an initial density of  $0.5 \text{ g/cm}^3$  (~42% of the bulk density of PMMA,  $1.18 \text{ g/cm}^3$ ) with the objective of facilitating the building of an amorphous structure through the AB. The dimensions in both  $x$  and  $y$ -axis were set at 7.3 nm, with the  $z$ -axis or thickness varying from 7.3 to 73 nm. After conditioning, these samples resulted in film of proper density and 5.5 and 50 nm in thickness respectively. It is important to note that attempts were made to build samples with initial thickness over 73 nm, but AB aborted without reaching a workable amorphous structure after 240 hrs of continuous process on a single CPU processor of the *Cosmos* supercomputer at Texas A&M. Several trials with variable base-to-film-thickness ratio and density as low as  $0.3 \text{ g/cm}^3$  were unsuccessful in producing a sample of initial thickness over 73 nm. Table 9 presents a summary of the film samples generated, all with density of  $0.5 \text{ g/cm}^3$  and a base ( $x/y$  footprint) of  $7.3 \times 7.3$  nm.

Table 9: Summary of film samples generated with the Amorphous Builder.

Sample	# of chains	N	# of atoms	z (nm)
f5	8	150	18016	7.36
f10	16	150	36032	14.72
f15_25	144	25	54288	22.08
f15_50	72	50	54144	22.08
f15_150	24	150	54048	22.08
f15_300	12	300	54024	22.08
f20	16	300	72032	29.44
f25	20	300	90040	36.80
f37	30	300	135060	55.20
f50	40	300	180080	73.60

### 5.3 Sample Conditioning

In order to bring the already generated amorphous film samples to the proper density and configuration, a multi-step procedure was followed using both *Cerius2* and LAMMPS from Sandia National Laboratories. The process began by assigning atomic charges to the samples using a Gasteiger equilibration algorithm; then performing an energy minimization of the samples in their fully atomistic descriptions. The following step was to map the models to the coarse grained representation.

#### 5.3.1 Coarse Grained Models

In Section 3.3 the details of the parameterization of the CG models was given, and results on a bulk samples up to 18000 atoms showed that both the 6 bead and 4 bead *b* model (from now on designated as *4 bead only*) can describe the behavior of the PMMA structure. The CG models also allow for an improvement on the speed of the simulation equal to 6 and 21.5 times that of the atomistic description. Given the large size of the film samples, the 4 bead model, showed in picture 20 was used to run the MD of the conditioning and testing of the samples.

The mapping of the fully atomistic to bead was performed following the procedure described in Section 3, with a C++ algorithm developed for this specific task. The algorithm produced an output file compatible with LAMMPS, which we used to perform the sample conditioning MD and required to increase the density of the films to the bulk value and impose the proper boundary conditions.

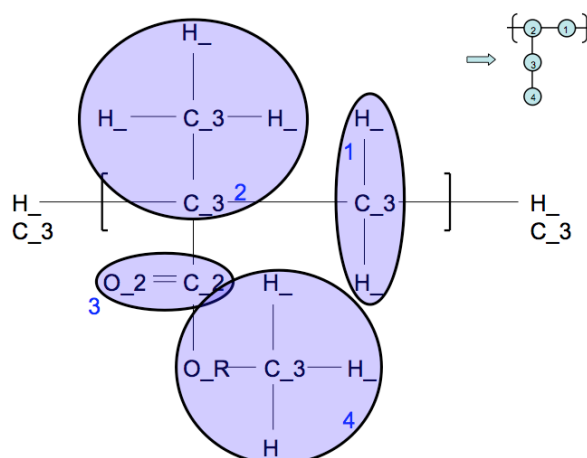


Figure 20: The 4-bead CG model of PMMA.

### 5.3.2 Substrate and Free Surface

The original film samples were created with a uniform, low density of  $0.5 \text{ g/cm}^3$  in order to obtain a suitable random amorphous structure. On a PMMA film, the bulk density is approximately  $1.18 \text{ g/cm}^3$  with the density near the surfaces expected to be affected by both the silicon substrate and the free surface: On the silicon substrate, the van der Waals, long range attractive forces are expected to bring the beads close to the wall thus increasing the packing density. At the free surface effect is the opposite, as a bead on this surface will only *feel* half of the neighbor beads interactions when compared to a bead in the center of the film.

For the modeling of the substrate we took advantage of one of LAMMPS's tools for boundary conditions: the Lennard-Jones 12-6 wall potential. The reasoning was that if silicon and oxygen atoms are physically put at the bottom of the simulation box, the quantity of wall-atoms should be enough to exert the appropriate non-bonded interaction

over the polymer beads. This meant that a large amount of non-polymeric beads needed to be added to the models, thus increasing the already large size of the samples. By running a small simulation in which every bead type was rotated in every possible angle at different distances from a  $\text{SiO}_2$  wall, a non-bonded interaction between the wall and the beads was calculated, and a Lennard-Jones wall potential was curve-fitted to model said interaction. Figure 21 depicts the procedure for a  $\text{CH}_3$  bead (from 6 bead model).

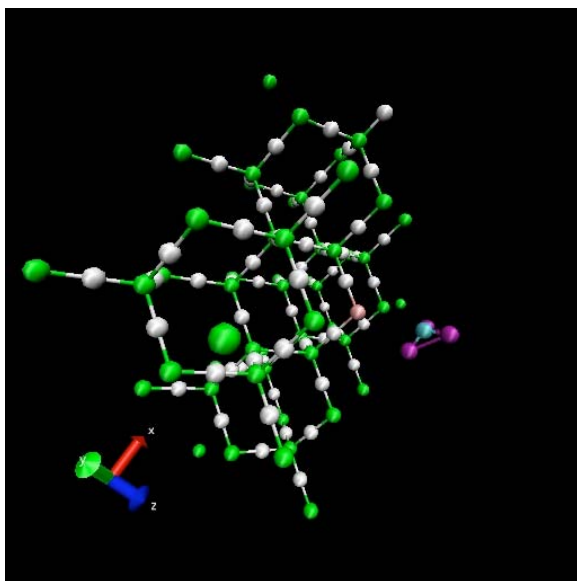


Figure 21: Simulation to estimate the bead- $\text{SiO}_2$  substrate interaction.

It can be argued that the presence of the wall atoms will induce a *cage effect* in some of the polymer atoms, affecting the mobility and dynamics near the wall. It is true that such effect is lost when a simple wall potential replaces the wall atoms, but on a CG representation any cage effect is unrealistic as the description of the polymer is greatly simplified. We consider this limitation a reasonable trade-off given the advantages of the

CG representations. Consequently, the simulations in this work would be representative of films supported by a *smooth, cleaned silicon wall* where the only interaction between wall and substrate is through van de Waals forces. No other interactions, like the strong polarity and acid-base effects of silicon native oxide on PMMA, are included in the model. The LJ wall potential at the substrate was given a cut-off ratio of 12 Å in order to guarantee the wall effect in the density and polymer chain arrangement near the wall.

At the free surface, the boundary condition was in principle easier to impose: A free film surface in contact with air has no wall potential. The density of the air is much lower than the polymer and therefore only few particles, if any, would be necessary to represent the interaction. The air-polymer interaction was considered negligible and no wall potential was assigned to the surface. However, since the initial samples required a process to increase their density to a bulk-like value, a wall potential has to be imposed so that the *compression* process can be contained and no uncontrolled expansion in the thickness direction results at the high pressures of the compression dynamics. Since at the free surface the attractive, long-range interaction of the van der Waal forces is limited in both magnitude and distance (perpendicular to the wall), a soft Lennard-Jones 9-3 potential was imposed for the *sample compression process* only. Figure 22 shows the results of the LJ interactions between the beads of the 4 bead model and the SiO<sub>2</sub> wall, and both the substrate and free-surface wall potentials.



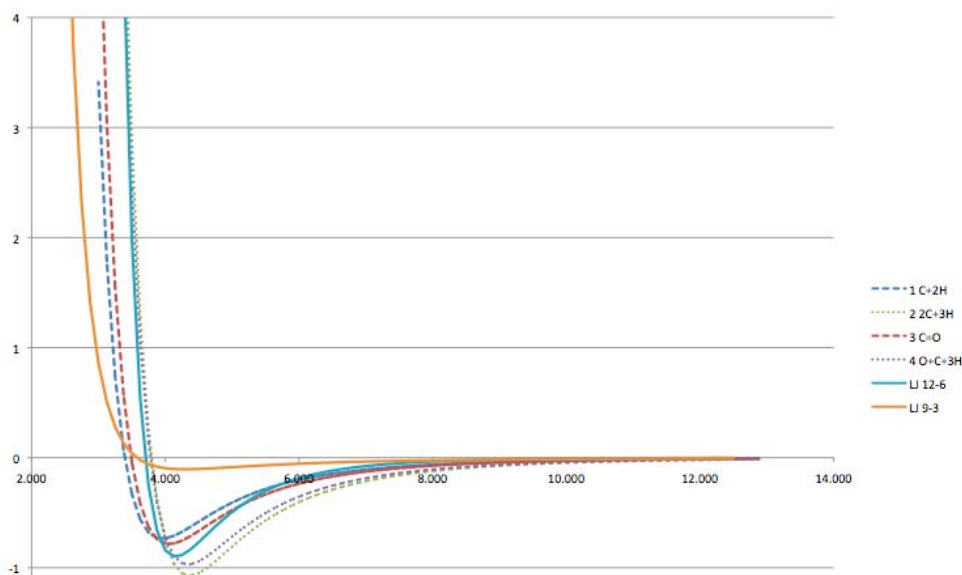


Figure 22: The Lennard-Jones wall potentials at the substrate (light blue) and free surface (orange).

One important note is that the free-surface wall potential limited the maximum time step of the MD simulation, as a long time step would allow a bead to jump into the highly repulsive part of the potential around  $3.5 \text{ \AA}$  making the system unstable. This restriction disappeared when the LJ 9-3 potential was removed.

### 5.3.3 Conditioning Procedure

The first part of the conditioning consisted on *compression* dynamics through NPT simulations at a pressure of 1000 atm and temperature of 300 K. The substrate and free-surface wall potential were imposed as boundary conditions in both  $z$ -axis limits, with a pressure-controlled periodic boundary condition in the  $x$  and  $y$ -axis. A wall velocity ranging from 1 to 10 nm per ns of simulation (depending on the thickness of the samples) was imposed to the bottom wall while a negative velocity of the same

magnitude was imposed to the free surface. This allowed for the reduction of the thickness of the low-density sample to a desired thickness in few nanoseconds of MD. The pressure condition of 1000 atm imposed at the periodic boundaries in  $x$  and  $y$  resulted in the reduction of those dimensions as well, though the final value was not actively controlled as in the  $z$ -axis dimension but was defined by the random configuration of the polymer chains. The outcome of this procedure was a set of film samples with the desired thickness, high internal pressure and density about 10% higher than the bulk density of PMMA.

The second step in the simulation was to run *decompression* dynamics. The objective to remove the *non-physical* free-surface wall potential but that cannot be accomplished without reducing the high internal pressure of the samples or therefore an uncontrolled expansion of the films will occur. The dynamics consisted on NPT simulations with non-moving wall potentials in the  $z$ -axis and a pressure control periodic boundary in both  $x$  and  $y$ -axis limits. The pressure was gradually reduced to from the initial high pressure (usually  $\sim 2000$  atm) to 1 atm in 8 steps and at every pressure step, a temperature annealing from 300 K to 600 K and back was performed with 100 ps of dynamics every 50 K. In this stage, a total of 8.8 ns of dynamics were performed in every sample, with the resulting films having the desired thickness, density, and at atmospheric pressure. Under these conditions, the Lennard-Jones 9-3 potential at the free surface was removed without affecting the samples negatively. Table 10 shows the characteristics of the samples after the decompression processes.

Table 10: Summary of film samples after decompression.

Sample	# of beads	density (g/cm <sup>3</sup> )	x (nm)	y (nm)	z (nm)
f5	4800	1.065	5.69	5.65	5.82
f10	9600	1.081	6.18	5.29	11.26
f15_25	14400	1.145	5.77	5.74	15.78
f15_50	14400	1.146	5.61	5.86	15.85
f15_150	14400	1.145	5.93	5.58	15.79
f15_300	14400	1.092	5.97	5.78	15.84
f20	19200	1.126	6.05	5.80	20.19
f25	24000	1.126	5.65	5.56	28.15
f37	36000	1.098	6.09	5.98	37.39
f50	48000	1.106	5.88	6.13	50.01

The next step in the conditioning process was to add the *hot particles* at the base of the sample (substrate) as a means to provide the energy input to the system. These particles were single LJ beads with no bonds, interacting with the polymer through a Van der Waals potential that was calculated so that in average has half the magnitude and radii of the Van der Waals potential between polymer beads. The objective was to induce the *hot particles* to be in equilibrium near the natural center point between non-bonded polymer beads and therefore minimize the effect of these particles on the configuration of the polymer chains.

A *grid* of 12x12 hot particles was added at the base of all samples, as shown in Figure 23. The particles had a molecular weight of 12.5 g/mol, roughly equivalent to half the average of the MW of the polymer beads. The MW was selected after short runs of dynamics where the positions and velocity of the hot particles were tracked. It is important to notice there is a trade-off in selecting the MW: (relatively) heavy particles

move slowly, improving the time step but creating a significant effect on the position/velocity of the surrounding polymer beads; while light particles have the opposite effect on the polymer but tend to *jump* thus creating potential overlapping and instability. Given the parameters of the 4 bead model FF, a MW of 12.5 g/mol for the hot particles seems to be good compromise.

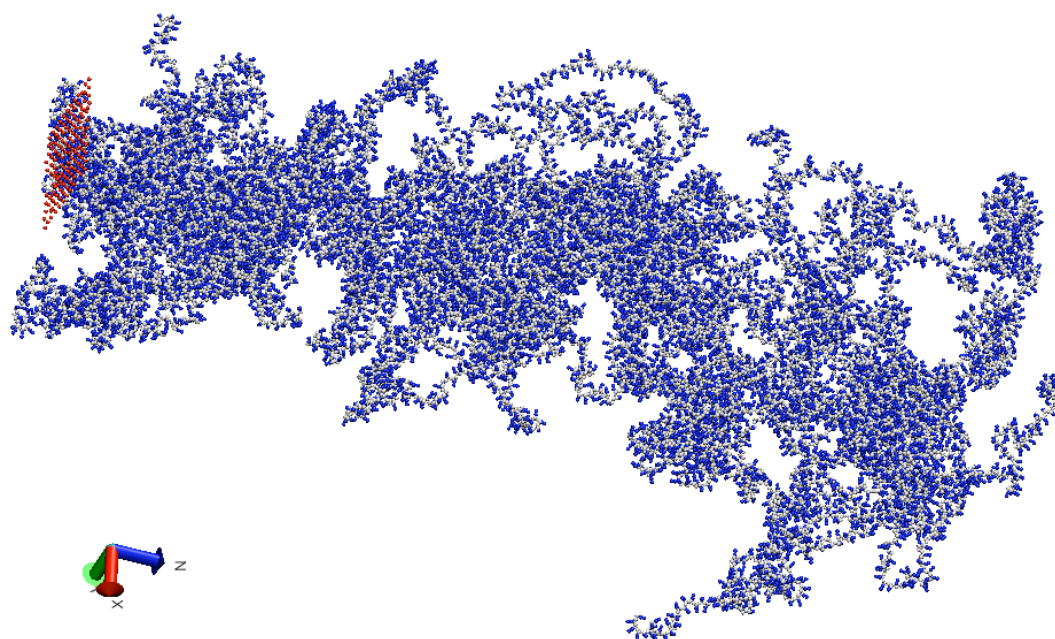


Figure 23: f50 sample (50nm) in a non-periodic unwrapped representation, showing the hot particles added to the substrate (red).

In order to prevent the hot particles to drift inside the polymer, a *drag* force was set on the particles as a function of their distance to the bottom wall. This force acted in the z-axis only and guaranteed the hot particles stayed within 3 Å of the wall position while at the same time allowed them to move freely on the x-y plane.

In regard to the heating source, it can be argued that by adding heat to the polymer beads near the wall the same heating effect can be obtained without the need for additional *non-physical* particles. Though this might be truth on a LJ liquid, in a polymer system as the one showed in Figure 23, it is clear that heat will travel faster through the bonded atoms (backbone) than by the weaker non-bond interactions. In such case, the polymer beads selected to be the heat source would have a great impact in the thermal transport. For example, if 10 beads are selected and 7 of them are in the same polymer chain, that particular chain physical configuration will dominate the heat transfer. By adding heat to non-polymeric particles that can freely move in an  $x$ - $y$  plane and interact with *all* polymer beads though a uniform van der Waals potential, uniform heating is granted.

One final note is that we attempted to implement the same boundary condition at the free surface to provide heat sink with *cold particles*, but the interaction between the polymer beads and the cold particles was too weak and we usually ended with the cold particles reaching zero energy, thus aborting the simulation. Moreover, due to the nature of the film, slight variations in thickness were observed and in some cases a gap generated between the cold particles and the free surface. The problem was avoided by using the all the polymer beads as a heat source in a manner similar to the *uniform volumetric heat generation* explained in Section 4.

The last part of the conditioning, after the hot particles were added, consisted of 50 ns of NpT dynamics at 300 K and atmospheric pressure. Results from Section 3 indicate the  $g(r)$  curves show minimal variation from 0 to 100 ns of dynamics and

collapse into a single curve after 100 ns; therefore 50 ns of NpT dynamics is considered a good compromise between improvement in the samples' condition and the computer resources available. For the NpT simulations the substrate potential was imposed, but the *non-physical* free-surface potential was removed in order to allow the surface to relax. The simulation was run at the larger time step allowed by the 4 bead model and consequently reducing the CPU time. These dynamics are considered long enough as to render the samples fully relaxed.

All the sample conditioning dynamics were run at the *Hydra* supercomputer at Texas A&M. The number of processors used in the parallel simulations of the film samples was scaled with the number of particles in the system by keeping the ratio of 500 particles/processor. The number of processors and physical memory per node, plus on-the-run performance, dictated whether or not the number of processors needed to be changed for a given simulation. Table 11 shows a summary of the simulation performance in ns of simulation per physical hour (running in all CPUs), and the total CPU-hrs used during the conditioning.

#### **5.4 Sample Dynamics**

As explained in section 2, there are *ensembles* that can be used in classical MD to calculate system properties. For example, in the microcanonical ensemble (NVE) the volume, energy and number of molecules of the systems are conserved, while in the canonical ensemble (NVT) the energy, instead of the temperature, is maintained constant.

Table 11: Coarse grained MD simulation performance on *Hydra* supercomputer.

Sample	# of processes	Performance (ns/hr)	Total CPU-hrs
f5	8	2.723	175.6
f10	16	1.581	605.2
f15_25	32	1.754	1091.0
f15_50	32	1.752	1092.2
f15_150	32	1.742	1098.7
f15_300	32	1.744	1097.1
f20	32	1.324	1444.9
f25	32	1.044	1833.4
f37	48	0.794	3615.7
f50	64	0.517	7402.9

In order to obtain the system's temperature response to a heat flux imposed as a boundary condition, a MD simulation with no active control over the temperature is needed. Moreover, the volume of the simulation box should be able to change because there are statistical changes in film thickness as temperature changes. Based on these requirements, any isothermal or isometric ensemble had to be discarded (microcanonical, canonical, grandcanonical, etc.) and therefore the isenthalpic-isobaric ensemble (NpH) was selected, as the pressure and the number of molecules can be assumed constant throughout the simulation.

In LAMMPS, the NpH ensemble performs constant time integration to update positions and velocities using a Nose/Hoover pressure barostat thus creating a trajectory consistent with the isobaric ensemble. This ensemble does not directly control the energy of the system and therefore we enforced an energy balance by adding/removing heat.

The first step of the dynamics was to run 1ns of NpH dynamics at 1 atm pressure and observe the response of the system temperature and energy, as shown in Figure 24.

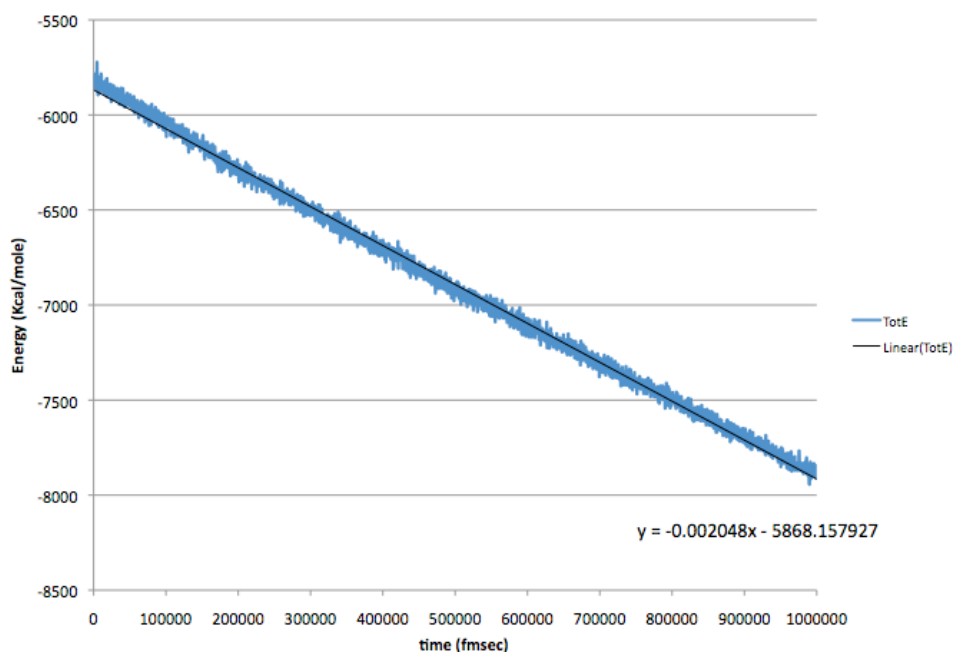


Figure 24: Variation of energy with respect to time on a NpH simulation.

All the films samples showed a behavior similar to the f5 sample showed in Figure 25, that is, the total energy of the system decreased linearly with time. The slope of the curve is expected to level at temperatures near the absolute zero, or otherwise the simulation will reach zero energy and likely abort. The temperature of the system also reduced linearly, as there is a direct link between energy and temperature. We recorded the change of energy per unit time and per degree temperature, and calculated the averages over 1 ns in the Table 12.



Table 12: Change in energy with time and temperature for the NPH simulations.

Sample	Energy/time (Kcal/mol fmsec)	Energy/K (Kcal/mol K)
f5	-0.002048	31.29
f10	-0.001716	63.45
f15_25	-0.001367	94.57
f15_50	-0.002149	92.70
f15_150	-0.002180	89.76
f15_300	-0.002085	95.42
f20	-0.002201	120.85
f25	-0.002175	150.68
f37	-0.002051	231.73
f50	-0.001880	299.41

The second column in Table 12 shows that the energy reduction per unit time was relatively constant and independent of the size of the system. However, there seems to be an effect of the degree of polymerization on the f15\_25 sample where the polymer chains are only 25 monomers in length. One possible explanation for this energy reduction is the effect of the *non-physical hot particles*. Hot particles are attached to a plane at the substrate in order to prevent them from drifting into the sample. When a polymer bead interacts with a hot particle, it transfers some of the energy and makes the hot particle change its direction. If the new direction is away from the z-plane, an external drag force keeps the particle from leaving the plane and therefore part of the particle energy is dampened, or lost. The plane where the hot particles are located may have a dampening effect if the temperature or energy are not controlled. In order to prevent this effect, we enforced an *energy balance* by adding energy to the polymer at

the same rate the energy was lost, thus maintaining constant energy throughout the simulation time. The last column on Table 12 is the slope of the sample total energy vs. temperature and it scales with the size of the systems, as expected. Once normalized by the number of moles in each film sample, the value came to be a constant  $1.070 \text{ J/g}_K$  for all samples, which is similar *in spirit* and magnitude to the *constant pressure specific heat*, though is about two-thirds of the  $C_p$  values previously obtained in CG the modeling of bulk PMMA.

#### 5.4.1 Energy Gradient

Adding kinetic energy to the hot particles and uniformly removing energy from the polymer imposed the heat flux during NPH simulation, but due to the change of total energy observed during the NPH simulation, additional energy was added to the system in order to maintain the energy balance. Figure 25 shows a schematic of the fluxes and balance.

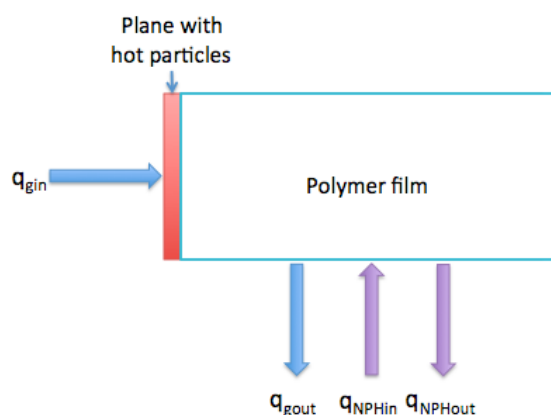


Figure 25: Heat balance on the polymer film during NpH simulation.

The heat balance during the simulation can be expressed as

$$q_{gin} + q_{gout} + q_{NPHin} + q_{NPHout} = 0 \quad (59)$$

where  $q_{gin}$  and  $q_{gout}$  are the energy fluxes imposed to establish the temperature gradient,  $q_{NPHout}$  is the energy loss during the NPH simulation and  $q_{HPNin}$  is the heat added to counteract the effect of  $q_{NPHout}$ . All the heat fluxed except  $q_{NPHout}$  are controlled variables of the simulation. If we seat  $q_g$  equal in magnitude to  $q_{NPH}$ , two of the heat fluxes vanish and the equation simply becomes

$$q_{gin} = q_{NPHout} \quad (60)$$

The samples were subject to 15 ns of NPH dynamics at a constant pressure of 1 atm and with a continuous energy flux to the hot particles equal in value to the middle column of Table 12. After the initial run, another 15 ns of NPH dynamics were performed but adding only *half* of Table 12 values, with the other *half* required to maintain the energy balance added directly to the polymer. This procedure is equivalent of testing the film at two different heat fluxes, and while the temperature values were expected differ, the resultant thermal conductivity should remain constant. For reference purposes, the surface heat flux generated by adding the Table 12 values to the hot particles was roughly equivalent to a heat flux of 70 kW/mm<sup>2</sup> coming from the substrate into the polymer.

Several regions or *slabs* parallel to the substrate were defined for the NpH simulation. Each region was 5 nm in thickness, with the first one beginning at the position of the substrate wall potential and the last region including the free surface. The slabs temperature was calculated by averaging the temperature of all beads inside the region at a given time step, and a data file with the average of the temperature every 50 time steps was generated. If a bead moved out of the slab boundary, said bead was considered part of the neighbor slab and therefore heat advection by the particle translation was accounted for, even though we expect this part of the heat flux to be zero in the solid phase of PMMA.

During the NpH simulations the films thickness fluctuated within 2% of its initial value and therefore, for the larger films, we reached a point in which particles slipped out of the very top slab, affecting the slab temperature. When only few particles were inside the top slab the temperature showed large fluctuations and an average value approximately 10 K higher than the surrounding slabs. Even though we have no specific description of phonons in our model, we regard this temperature effect as a consequence of the *phonon scattering* at the surface, where the end particles had less means of dissipating/transmitting the energy and the vibrations reflected back in a manner similar to the *tip effect* in a whip. When no particles were present in the slab, the temperature dropped to zero and the value was discarded.

#### 5.4.2 Data Generated

Throughout the NpH simulations, the following data was generated for each sample:

- Average slab temperature, averaged over 50 time steps.
- Average slab kinetic energy, total potential energy and pair potential energy.

These values were calculated in a similar way to the temperature, averaging the values of the beads contained inside each slab every 50 time steps.

- Volume, x-y-z dimensions, overall sample temperature, pressure, and energies (pair, VdW, bond, angle, etc.) every 50 time steps.
- Trajectory with the position and velocity of each bead, every 200 time steps.
- Restart files every nano second (~200 000 time steps).

The data files generated by the 30 ns of NpH dynamics across all the film samples required approximately 400 GB of storage, with most of the data being the trajectory files (8.1 GB/ns of dynamics on the f50 sample). In order to analyze such large collection of data, we wrote a code to produce averages and standard deviation values over nanosecond intervals. For the temperature profiles a least-squares approximation was used to generate curve-fitting parameters because a quadratic dependence of temperature with thickness was expected.

## 6. RESULTS AND ANALYSIS

### 6.1 Introduction

In this section the results from the MD simulations of the PMMA films are presented.

The first part consists of the analysis of temperature profiles through the thickness of the films and the determination of each film's thermal conductivity. Then the dependence of thermal conductivity with respect to film thickness and the degree of polymerization (for the 15 nm films) are presented and compared to the experimental results for similar PMMA films. In the last sub section, the kinetic and potential energy profiles are presented with a discussion of the effect of the substrate and the free surface on the thermal transport of the films.

### 6.2 Temperature Profiles

Figure 26 shows the temperature response of the f50 sample (50 nm thickness) to the heat flux imposed as a boundary condition. The values are the averages over nanosecond periods obtained directly from the simulation results (no-post processing). The silicon substrate is on the left ( $Z=0$  Å) while the free surface is on the right.

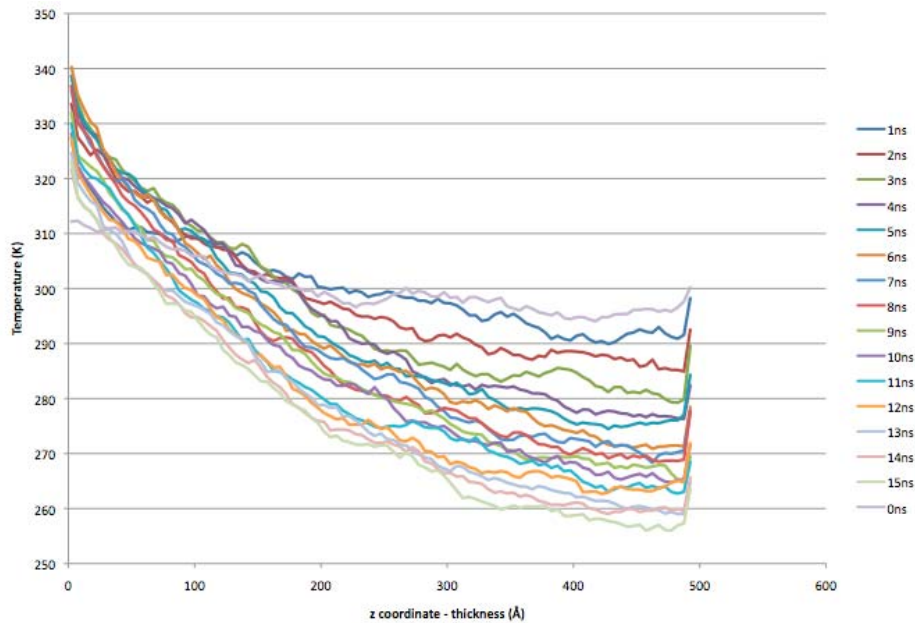


Figure 26: Temperature profiles for the f50 sample.

The initial temperature profile (0 ns) averaged 300 K, but its local value seem to increase few degrees towards the substrate while it tends to be around 295 K near the free surface. When the heat flux is imposed the substrate temperature increased while the free surface reduced, as expected. However, after reaching steady state, the overall temperature kept reducing approximately 1 degree K per nanosecond, suggesting that the system was losing more energy than the amount added to compensate for the NpH simulation ( $q_{NPH}$ ). According to eq. (55), the temperature profile through the film thickness depends only on the thermal conductivity and the heat added in ( $q_{in}$ ), with the temperature at the substrate ( $T_s$ ) being defined as a boundary condition. If, only for visualization purposes, all the temperatures in Figure 26 are shifted to the same free surface temperature as shown in Figure 27, we observe that at time equal 1, 2 and 3 ns the temperature profile varied indicating the heat flux is not steady, but after 3 ns all the

temperature profiles collapsed into a band with a similar trend. This behavior was the same across all the samples, with the smaller samples reaching a steady temperature profile in less than 1 ns. All temperature profiles after 5 ns of constant heat flux were considered *steady state* and used to calculate the thermal conductivity.

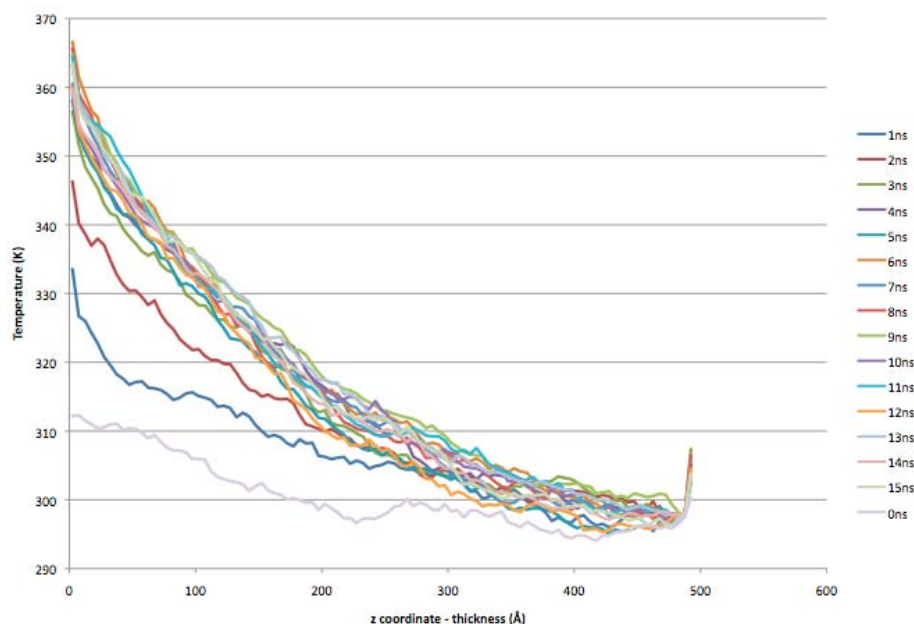


Figure 27: Shifted temperature profiles for the f50 sample.

It can be seen in both Figures 26 and 27 there is temperature increase in the slab at the free surface ( $Z=500 \text{ \AA}$ ). This jump of few degrees is the only manifestation (by an abnormal increase on the kinetic energy of the beads) of phonon scattering on the samples and it is only evident on the last or last two angstroms of the slab, hence confirming Klemens' calculation of the Casimir limit being in the order of an atomic bond length for an amorphous system at room temperature. Since all the hot particles



resided in the first slab near the substrate, the temperature of both the first and last slabs were considered abnormal and not included in the thermal conductivity calculations.

The temperature profiles of all the samples showed a quadratic dependence with respect to the z-coordinate or thickness. Figure 28 shows the least squares curve fit for the temperature profiles of the f37 sample from 16 to 28 ns, with a very good agreement between the MD data and the curve fit. It is worth noting the heat flux input of all samples was halved at  $t=15$  ns and therefore the curves at 16 and 18 ns are considered transients, even though the system seems to have reached steady state at 18 ns. Another finding is that curve slopes tend to reach zero at the free surface, which is expected given the free surface boundary condition akin to a thermally isolated wall. Figure 29 shows the same plot as Figure 28 but for the f5 sample between 0 to 15 ns. In the smaller film samples the temperature gradient was less pronounced and the statistical variation of the temperature (with a standard deviation of 6 degrees K) masked the profiles. The values at 3 and 9 ns, for example, seemed to be in disagreement with the other 5 temperature profiles showed in the Figure 29. Nevertheless, the quadratic fit still showed a good match for the temperature profiles.

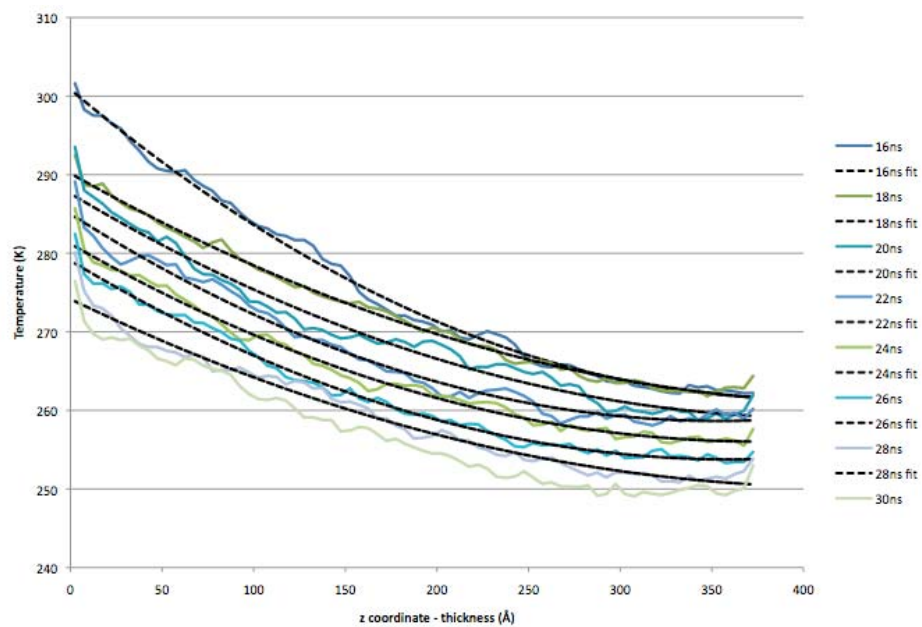


Figure 28: Temperature profiles and curve fit for the f37 sample.

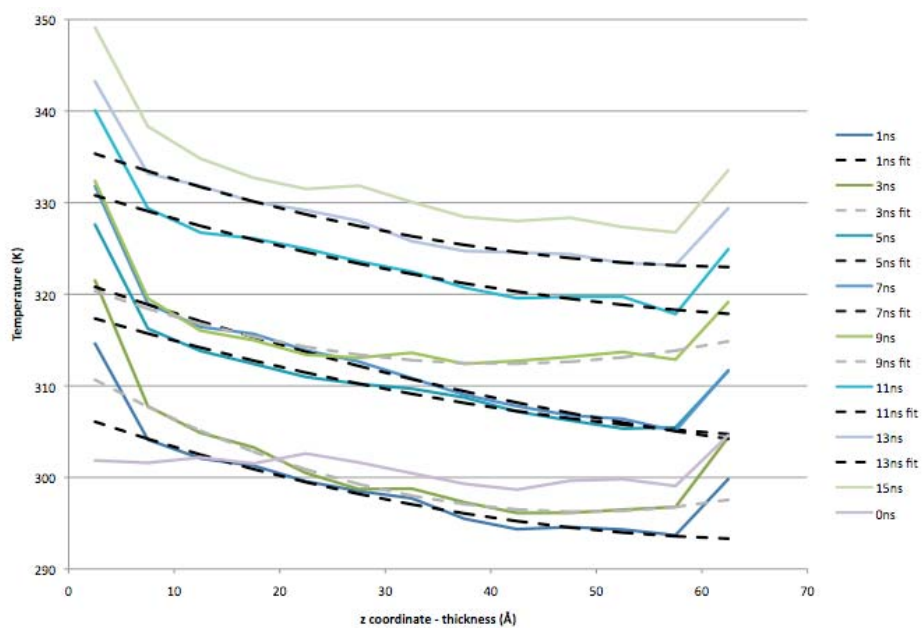


Figure 29: Temperature profiles and curve fit for the f5 sample.

According to the eq. (55) showed below, the proportionality constants obtained from the curve fitting,  $C_1$  and  $C_2$ , which multiply the  $x$  and  $x^2$  terms respectively (akin to  $z$  and  $z^2$  terms in the film samples) can be used to calculate the thermal conductivity as the value of  $q'''$  is known ( $q_{in}$ ). If eq. (55) is to represent good fit to the data from the MD simulations, the thermal conductivity values obtained from  $C_1$  and  $C_2$  should be similar, and the ratio  $C_2/C_1$  equal to  $-2L$ , with  $L$  being the thickness of sample.

$$T(x) = \frac{-q'''}{2k} x^2 + \frac{q'''L}{k} x + T_s \quad (55)$$

The procedure followed to calculate the thermal conductivity was:

- The temperature profiles were averaged over 1 ns time intervals.
- The data from 0 to 5 ns and from 15 to 20 ns was discarded. This was because the energy input was changed at time equal 0 and again at 15 ns, and the first 5 ns after a heat flux change are considered *transient regime*.
- A least-square quadratic curve fit was applied to the temperature profiles, and the ratio  $C_2/C_1$  was used to calculate the variable  $L$ , or *pseudo-thickness*. If the calculated pseudo-thickness was within 30% of the actual film thickness of the samples, the curve fit was considered good and the thermal conductivity from  $C_1$  and  $C_2$  was calculated and averaged.
- All thermal conductivities for a sample were averaged and the standard deviation calculated as a measure of dispersion.

In general, we found that only 3-4 profiles out of the 20 *steady state* temperature profiles has to be discarded due to disagreement between the pseudo-thickness and actual thickness of the samples. The exception was sample f5 in which 6 values were discarded, but this was expected given dispersion in temperature gradients showed in Figure 29. In the film samples over 25 nm thickness, only 1 or 2 values were discarded thus indicating a good agreement of eq. (55). There was no significant difference between thermal conductivity values calculated at different heat fluxes in a given sample, thus validated the theoretical model.

### 6.3 Thermal Conductivity

Figure 30 shows the averaged thermal conductivity of the films as a function of the film thickness. The error bars indicate one standard deviation above and below the average values, which are presented in Table 13. The first observation is that for film thicknesses between 15 nm and 50 nm, the thermal conductivity calculated by MD is on average 0.135 W/m\_K. This value is 35% lower than the experimental thermal conductivity for bulk PMMA (0.212 W/m\_K), but it is considered a very good approximation. In the discussion following Table 12 in section 5, we showed the films' average energy variation with temperature during the NpH dynamics was 0.501 J/g\_K, which is lower than the specific heat of bulk PMMA (1.466 J/g\_K) and therefore, a lower value of thermal conductivity from the models is reasonable. For film thickness below 15 nm, there seems to be a decrease in the thermal conductivity in line with experimental findings in published literature but that does not follow the experimental

results obtained by Kim [71] on PMMA films of similar thickness. At thickness equal 15 nm there are 4 data points representing the film samples with different degrees of polymerization (N). The data point in red is the value calculated from the sample with N=25 and it is considered an abnormal value. Figure 31 shows that N of 50 or above is necessary to obtain a thermal conductivity independent of the degree of polymerization. It is worth noting that in Section 2 we defined the entanglement length of PMMA to be approximately 100 monomers, and it is argued that with N below 50 the polymer has limited entanglement and behave more as a polymer melt. All film samples, with the exception of f15\_25 and f15\_50, had N=150 or 300 and therefore the thermal conductivity obtained from these samples is considered independent of the polymer chain length.

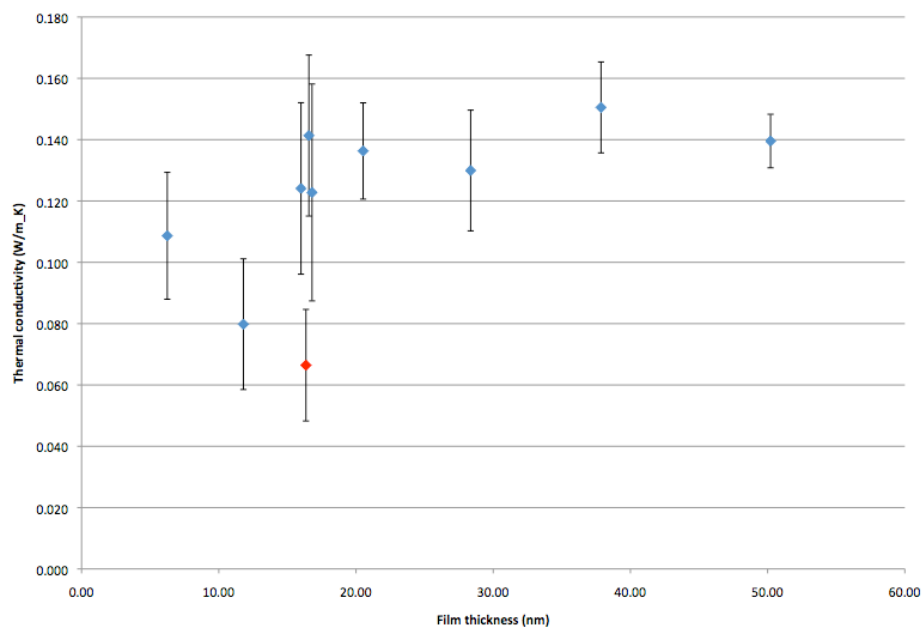


Figure 30: Thermal conductivity as a function of film thickness. Data point in red indicated film with degree of polymerization below entanglement length of PMMA.

Table 13: Calculated thermal conductivities for the PMMA films.

Sample	Thermal conduct. (W/m_K)	Standard deviation
f5	0.109	0.021
f10	0.080	0.021
f15_25	0.066	0.018
f15_50	0.141	0.026
f15_150	0.124	0.028
f15_300	0.123	0.035
f20	0.136	0.016
f25	0.130	0.020
f37	0.151	0.015
f50	0.140	0.009

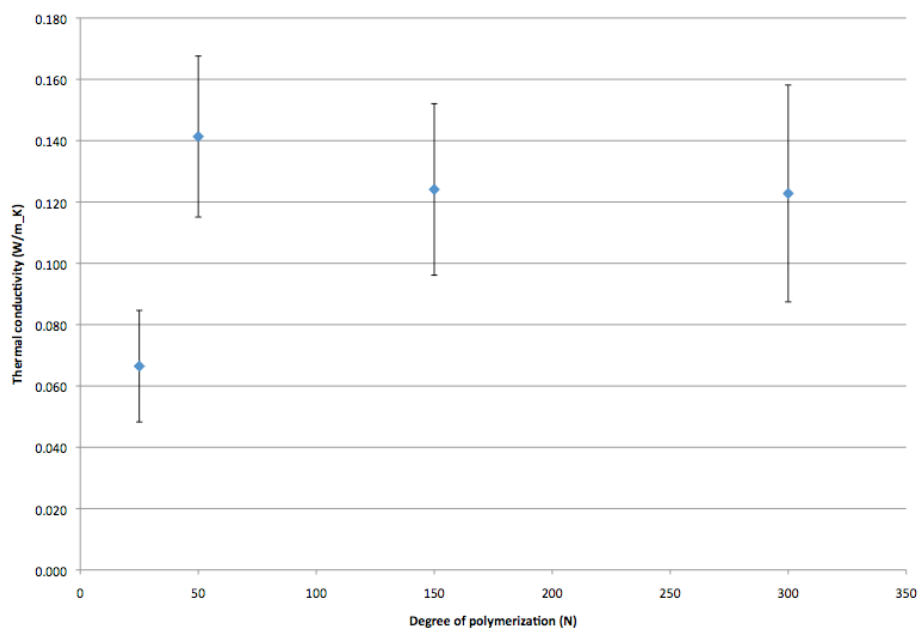


Figure 31: Thermal conductivity of the f15 sample as a function of the degree of polymerization.

The experimental results from Kim on PMMA films spin-coated over a silicon wafer substrate are showed in Figure 32 and are included here because it is roughly the same system we set out to model numerically. Kim used the Transient-Thermo Reflectance method (TTR) to obtain the thermal conductivity, detecting a 13% increase in its value for films with thickness equal to 188 nm and a 238% increase at thickness equal to 40 nm. Kim theorizes that the attractive interaction between the PMMA film and the native oxide on the (100)-silicon wafer caused an increase on the mass density and acoustic speed of the films near the surface, consequently increasing the thermal conductivity as film thickness reduced. This findings agree with published literature on behavior of  $T_g$  for supported PMMA films over silicon with native oxide.

Thermal Conductivity and Mean Free Path of Phonon vs. PMMA Film Thickness

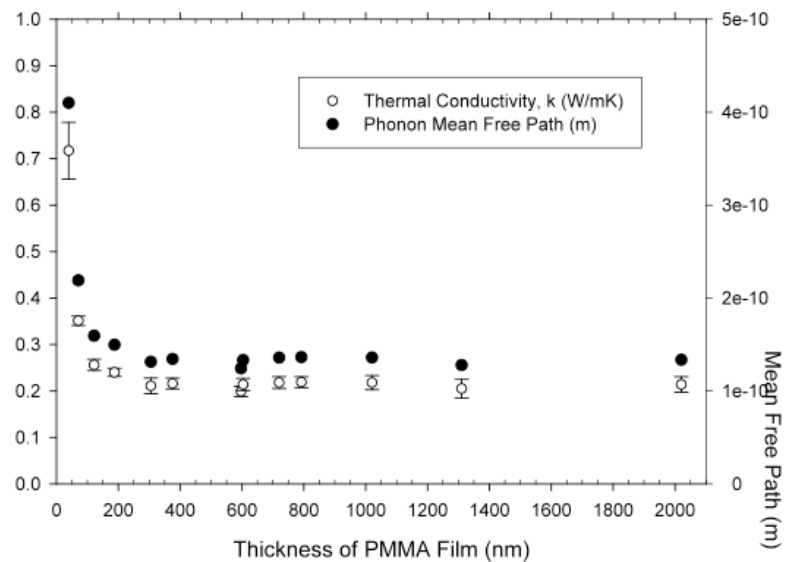


Figure 32: Experimental thermal conductivity of PMMA film samples by Kim [71].

In the present work we found no evidence of an increase of sample density with reduced thickness. If there is an effect, it is actually a *reduction* in density for films under 10 nm, most likely caused by the effect of the free surface. Figure 33 shows the film density of all the samples (from Table 10) as a function of thickness. It is important to point that as described in Section 5.3.2, the substrate potential used in this investigation is equivalent to perfectly smooth, clean silicon with no native oxide. Experimental investigations had shown that in such substrates the density of PMMA films reduced (up to 5%) with reduced thickness and therefore the model used in this work is a good representation of the experiments, though it might not described the experiments of Kim. Further details on experimental work can be fun in the appendix.

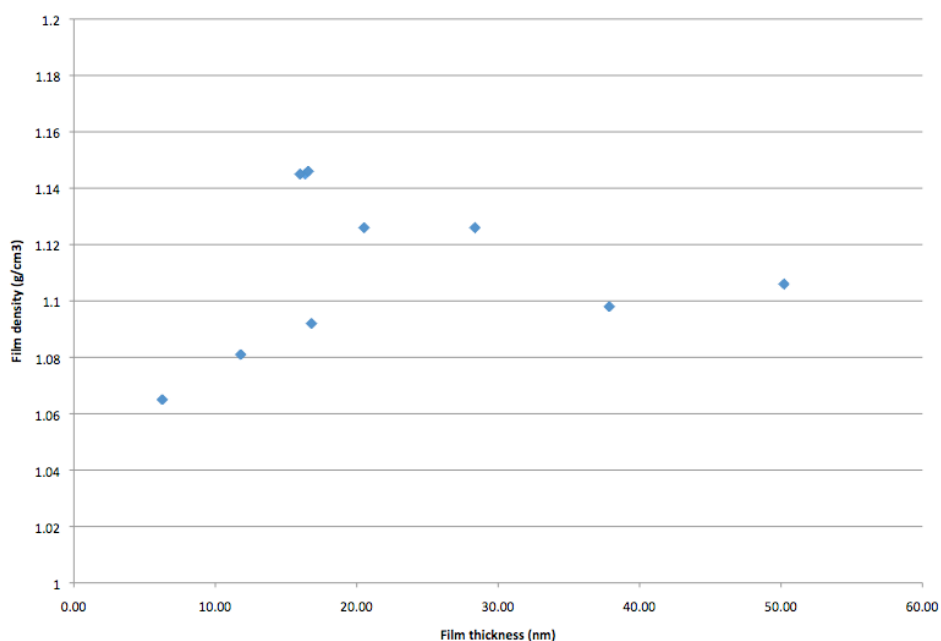


Figure 33: Density of film samples as a function of thickness.



## 6.4 Energy

Figures 34 and 35 show the kinetic and total potential energy of the f50 sample as a function of the sample thickness. There is a *zigzag* like fluctuation in the energy between neighboring slabs, which is probably due to the variation of the number of beads per slab. On average, every slab should have 480 beads, but if a slab has more than the average, the neighbor slabs will have fewer beads as the samples were conditioned as fully amorphous and under uniform pressure. The zigzag fluctuation persevered throughout the MD simulation time indicating the beads were not likely to move between slabs, which is expected in a solid phase. Changes in the relative position of the *peaks* in the energy curves were mostly due to the samples' thickness variation during the simulation time. In any case, the variations were within 10% of the average.

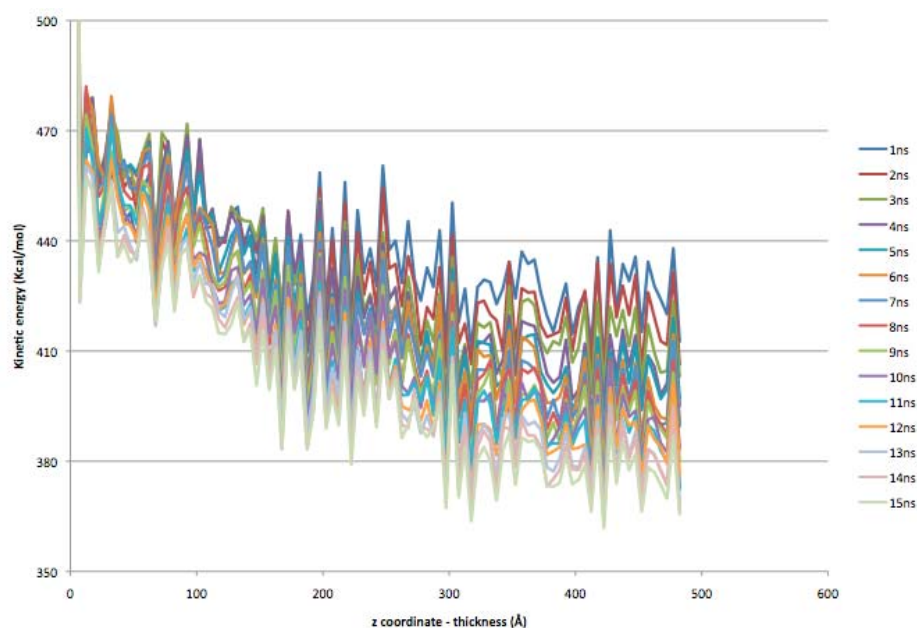


Figure 34: Kinetic energy as a function of thickness for the f50 sample, 15 ns.

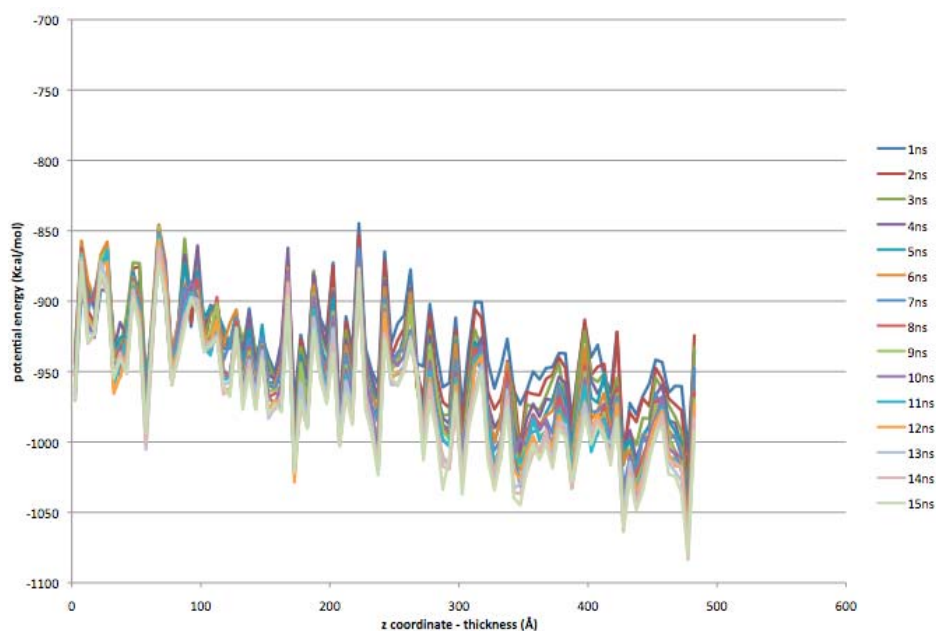


Figure 35: Potential energy as a function of thickness for the f50 sample, 15 ns.

Figure 34 shows that the kinetic energy follows the quadratic dependence with thickness as the temperature profile in Figure 26. As expected, the exchange of kinetic energy the main carrier of heat through the sample. Figure 35 shows that total potential energy (bond + angle + Van der Waals) is higher closer to the substrate where the attractive wall potential increase the energy, while it is lower near the top surface where the non-bon pair energy reduces as the number of neighbors diminish near the free wall.

Based on these figures, one can argue tha the total potential energy in the center of the f50 sample, between 120 and 300 Å, is constant at -940 Kcal/mol thus indicating this area has neither influence from the free surface nor the substrate. As the thickness of the film sample is reduced, the *competing effects* of both surfaces on the thermal conductivity of the film cancel each other. When the thickness is reduced to around 100 Å, the surface effect prevails and the thermal conductivity of the sample reduces with

thickness. The statistical variation of the data does not allow for a qualitative proof of this hypothesis, but we found the same behavior across all the film samples.

Figure 36 present the same plots for the f10 sample, showing they follow the same trend.

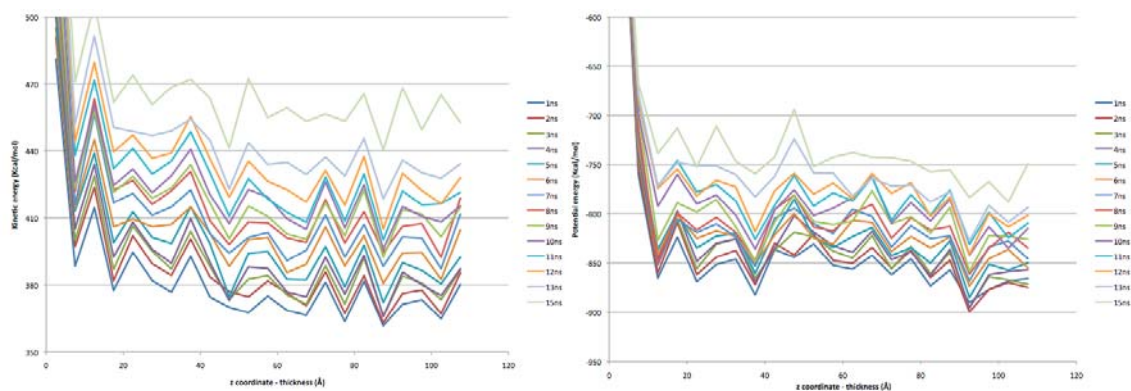


Figure 36: Kinetic (left) and potential (right) energies as a function of thickness for the f10 sample, 15 ns.

## 7. CONCLUSIONS

### 7.1 Summary

The reverse non-equilibrium molecular dynamics simulation technique was used along with coarse-grained modeling to simulate ultra-thin films of PMMA with film thicknesses ranging from 5 nm to 50 nm and layered over a treated silicon oxide substrate. In order to run the simulations with reasonable computer resources, six coarse grained models of PMMA were developed and tested, with 2 of them selected due to their good agreement with experimental and numerical data from previous studies of PMMA and their improved performance, resulting in processing times up to 21.5 times faster than similar size atomistic representations. A heat flux boundary condition was imposed to the films and the temperature profiles across the thickness were obtained as a response, enabling the estimation of the thermal conductivity. The results show temperature profiles that obey the Fourier equation heat transfer. The average thermal conductivity was 0.135 W/m\_K for film thickness from 50 to 15 nm, with no evident variation of the conductivity with respect to film thickness. Films of 5 and 10 nm thickness showed thermal conductivities ~30% lower but with higher degree of uncertainty due to the statistical dispersion of the results. The calculated thermal conductivity is on the same order of magnitude as the experimental thermal conductivity for bulk PMMA (0.212 W/m\_K), which, giving the limitations and approximations of the methodology used, is considered a satisfactory result.

## 7.2 Conclusions

The concluding remarks of this work can be summarized as,

- There is no dependence of the thermal conductivity of PMMA films over treated silicon oxide substrates, with respect to the thickness of the films, when thicknesses vary from 50 nm to 15 nm.
- There is an *apparent reduction* of the thermal conductivity of the PMMA films under 15 nm thickness. The reduction is 30% in average, but might be caused by statistical variation of the data generated by MD. In any case, an *increase* in thermal conductivity, as suggested by experimental results in similar systems, was not observed.
- The exchange of kinetic energy (momentum) of is the main carrier of heat in the samples tested. Potential energy curves show the influence of the substrate and free surface, and these effects seem to *cancel* each other as the film thickness is reduced.
- There is an effect of the degree of polymerization in the thermal conductivity. Thermal conductivity dropped 50% when the chain length was 25% of the entanglement length for PMMA.
- The Fourier equation of heat transfer is perfectly suitable to describe the temperature profile of the PMMA samples tested.
- Coarse-grained models are useful to simulate larger systems and obtain average properties that compare well with atomistic simulations. In this investigation, an

improvement of 21.5 times in computer performance was possible with the use of coarse representation.

**REFERENCES**

- [1] Intel Corporation, 2008, "Technology with the Environment in Mind," Intel Technology Journal, accessed in May 2009.  
<http://www.intel.com/technology/itj/2008/v12i1/7-evaluation/2-intro.htm>
- [2] Bashnagel, J., Binder, K., Doruker, P., Gusev, A., Hahn, O., Kremer, K., Mattice, W., Muller-Plathe, F., Murat, M., Paul, W., Santos, S., Suter, U., and Tries, V., 1998, "Bridging the Gap Between Atomistic and Coarse-Grained Models of Polymers: Status and Perspectives," *Advances in Polymer Science*, **152**, pp. 41-156.
- [3] van Heijnsbergen, D., von Helden, G., Duncan M., van Roij, A., and Meijer, G., 1999, "Vibrational Spectroscopy of Gas-Phase Metal-Carbide Clusters and Nanocrystals," *Phys. Rev. Lett.* **83**(24), pp. 4983-4986.
- [4] Durig, U., Cross, G., Despont, M., Drechsler, U., Haberle, W., Lutwyche, M.I., Rothuizen, H., Stutz, R., Widmer, R., Vettiger, P., Binning, G.K., King, W.P., and Goodson, K.E., 2000, "Millipede - an AFM Data Storage System at the Frontier of Nanotribology," *Tribology Letters*, **9**(1-2), pp. 25-32.
- [5] Venkatasubramanian, R., Silvola, E., Colpitts, T., and O'Quinn, B., 2001, "Thin-film Thermoelectric Devices with High Room-temperature Figures of Merit," *Nature*, **413**, pp. 597-602.
- [6] Soldera, A., and Grohens, Y., 2002, "Molecular Modeling of the Glass Transition of Stereoregular PMMAs," *Polym.-Plast. Technol. Eng.*, **41**(3), pp. 561-571.

- [7] Soldera, A., and Metatla, N., 2000, "Glass Transition Phenomena Observed in Stereoregular PMMAs Using Molecular Modeling," *Composites: Part A*, **36**, 521-530.
- [8] Sane, S., Cagin, T., Knauss, W., and Goddard, W., 2001, "Molecular Dynamics Simulations to Compute the Bulk Response of Amorphous PMMA," *Journal of Computer-Aided Materials Design*, **8**, pp. 87-106.
- [9] Subramanian, V., Asirvathan, P. Balakrishnan, R., and Ramasami, T., 2001, "Molecular Mechanics Studies on Polypropylene and Polymethylmethacrylate Polymers," *Chemical Physics Letters*, **342**, pp. 603-609.
- [10] Soldera, A., and Grohens, Y., 2002, "Local Dynamics of Stereoregular PMMAs Using Molecular Simulation," *Macromolecules*, **35**, pp.722-726.
- [11] Soldera, A., and Grohens, Y., 2004, "Cooperativity in Stereoregular PMMAs Observed by Molecular Simulation," *Polymer*, **45**(4), pp. 1307-1311.
- [12] Soldera, A., 2002, "Energetic Analysis of the Two PMMA Chain Tacticities and PMA Through Molecular Dynamics Simulations," *Polymer* **43**(15), pp. 4269-4275.
- [13] Kalogeras, I., 2004, "Thermally Stimulated Currents of Poly(methyl methacrylate): Comments on the Molecular Origin of a Debye-type Signal Between the  $\alpha$  and  $\beta$ -Relaxation Modes," *Journal of Polymer Science: Part B*, **42**, pp. 702-713.
- [14] Pfister, L.A., and Stchurski, Z.H., 2002, "Micromechanics of Stress Relaxation in Amorphous Glassy PMMA Part II: Application of the RT Model," *Polymer*, **43**(26), pp. 7409-7417.



- [15] Stoliarov, S., Westmoreland, P., Nyden, M., and Forney, G., 2003, "A Reactive Molecular Dynamics Model of Thermal Decomposition in Polymers: I. Poly(methyl methacrylate)," *Polymer*, **44**(3), pp. 883-894.
- [16] Apel, U.M., Hentschke, R., and Helfrich, J., 1995, "Molecular Dynamics Simulation of Syndio- and Isotactic Poly(methyl methacrylate) in Benzene," *Macromolecules*, **28**, pp. 1778-1785.
- [17] Okada, O., Oka, K., Kuwajima, S., Toyoda, S., and Tanabe, K., 2000, "Molecular Simulation of an Amorphous Poly(methyl methacrylate)–Poly(tetrafluoroethylene) Interface," *Computational and Theoretical Polymer Science*, **10**, pp. 371-381.
- [18] Jawalkar, S., Susheelkumar, G., Malladi, S., Mallikarjuna, N., and Tejraj, M., 2005, "Molecular Modeling on the Binary Blend Compatibility of Poly(vinyl alcohol) and Poly(methyl methacrylate). An Atomistic Simulation and Thermodynamic Approach," *Journal of Physical Chemistry B*, **109**(32), pp. 15611-15620.
- [19] Genix, A., Arbe, A., Alvarez, F., Colmenero, J., Willner, L., and Richter, D., 2005, "Dynamics of Poly(ethylene oxide) in a Blend with Poly(methyl methacrylate). A Quasielastic Neutron Scattering and Molecular Dynamics Simulations Study," *Physical Review E* **72**, 031808, pp.1-8.
- [20] Fukao, K., Uno, S., Miyamoto, Y., Hoshino, A., and Miyaji, H., 2001, "Dynamics of  $\alpha$  and  $\beta$ - Processes in Thin Polymer Films: Poly(vinyl acetate) and Poly(methyl methacrylate)," *Physical Review E*, **64**, 051807, pp.1-11.

- [21] Hartmann, L., Gorbatschow, J., Hauwede, J., and Fremer, F., 2002, "Molecular Dynamics in Thin Films of Isotactic Poly(methyl methacrylate)," *European Physical Journal E*, **8**, pp. 145-154.
- [22] Roth, C., and Dutcher, J., 2003, "Glass Transition Temperature of Freely-Standing Films of Atactic Poly(methyl methacrylate)," *European Physical Journal E*, **12**, pp. 103-107.
- [23] Hou, Y., and Higgins, A., 2002, "Single Molecule Studies of Dynamics in Polymer Thin Films and at Surfaces Effect of Ambient Relative Humidity," *Journal of Physical Chemistry B*, **106**(40), pp. 10306-10315.
- [24] Minelli, C., Frommen, C., Hinderling, C., Pugin, R., Heinzelmann, H. and Liley, M., 2006, "The Influence of Nanoparticle Fillers on the Morphology of a Spin-cast Thin Film Polymer Blend," *Colloid Polymer Science*, **284**, pp. 482-488.
- [25] Zhou, J., Krueger, S., and Gregurik, K., 2005, "A Coarse Graining Approach to Determine Nucleic Acid Structures from Small Angle Neutron Scattering Profiles in Solution," *Nucleic Acid Research*, **33**(19), pp. 6361-6371.
- [26] Molinero, V., and Goddard, W., 2004, "M3B: A Coarse Grain Force Field for Molecular Simulations of Malto-Oligosaccharides and Their Water Mixtures," *Journal of Physical Chemistry B*, **108**(4), pp. 1414-1427.
- [27] Buehler, M., and Huajian, G., 2005, "Ultra-Large Scale Simulations of Dynamic Material Failure," *Handbook of Theoretical and Computational Nanotechnology*, vol. **X**, Chapter 14, American Scientific Publishers, Valencia, CA., edited by Michael Rieth and Wolfram Schommers, pp. 1-41.

- [28] Iotov, M., and Goddard, W., 1998, "Diffusion in Amorphous Media," Ph.D. dissertation, California Institute of Technology, Pasadena, CA.
- [29] Wikipedia.org, "Molecular Dynamics," accessed in November 2009.  
[http://en.wikipedia.org/wiki/Molecular\\_dynamics](http://en.wikipedia.org/wiki/Molecular_dynamics)
- [30] Meng, B., and Weinberg, W.H., 1994, "Monte Carlo Simulations of Temperature Programmed Desorption Spectra," *Journal of Chemical Physics*, **100**, pp. 5280-5286.
- [31] Haile, J.M., and Graben, H.W., 1980, "Molecular Dynamics Simulation Extended to Various Ensembles: I. Equilibrium Properties in the Isoenthalpic-Isobaric Ensemble," *J. Chem. Physics* **73**(5), pp. 2412-2419.
- [32] Sun, H., 1998, "COMPASS: An Ab Initio Force-Field Optimized for Condensed-Phase Applications-Overview with Details on Alkane and Benzene Compounds," *Journal of Physical Chemistry B* **102**(38), pp. 7338-7364.
- [33] Wikipedia.org, "Force Field (Chemistry)," accessed in November 2009.  
[http://en.wikipedia.org/wiki/Force\\_field\\_\(chemistry\)](http://en.wikipedia.org/wiki/Force_field_(chemistry))
- [34] Wikipedia.org, "List of software for Molecular Dynamics Modeling," accessed in November 2009.  
[http://en.wikipedia.org/wiki/List\\_of\\_software\\_for\\_molecular\\_mechanics\\_modeling](http://en.wikipedia.org/wiki/List_of_software_for_molecular_mechanics_modeling)
- [35] Accelrys Inc., "Materials Studio Overview," accessed in November 2009.  
<http://accelrys.com/products/materials-studio/>
- [36] Plimpton, S.J., 1995, "Fast Parallel Algorithms for Short-Range Molecular Dynamics," *Journal of Computational Physics*, **117**, pp. 1-19.

- [37] Baschnagel, J., and Varnik, F., 2005, "Computer Simulations of Supercooled Polymer Melts in the Bulk and in Confined Geometry," *Journal of Physics: Condensed Matter*, **17**, pp. R851-R953.
- [38] Kremer, K., and Grest, G.S., 1990, "Dynamics of Entangled Polymer Melts: A Molecular-Dynamics Simulation," *Journal of Chemical Physics*, **92**, pp. 5057-5086.
- [39] Bennemann, C., Paul, W., Binder, K., and Dünweg, B., 1998, "Molecular-Dynamics Simulations of the Thermal Glass Transition in Polymer Melts: Alpha-Relaxation Behavior," *Physical Review E*, **57**, pp. 843-851.
- [40] Varnik, F., Baschnagel, J., and Binder, K., 2002, "Reduction of the Glass transition Temperature in Polymer Films: A molecular-Dynamics Study," *Physical Review E*, **65**, 021507, pp. 1-14.
- [41] Baschnagel, J., Maeyer, H., Varnik, F., Metzger, S., Aichele, M., Muller, M., and Binder, K., 2003, "Computer Simulations of Polymers Close to Solid Interfaces: Selected Topics," *European Physical Journal E*, **12**, pp. 167-171.
- [42] Varnik, F., Baschnagel, J., Binder, K., and Mareschal, M., 2003, "Confinement Effects of the Slow Dynamics of a Supercooled Polymer Melt: Rouse Modes and the Incoherent Scattering Function," *Interface Science*, **11**, pp. 159-173.
- [43] Varnik, F., Baschnagel, J., and Binder, K., 2002, "Static and Dynamic Properties of Supercooled Thin Polymer Films," *European Physical Journal E*, **8**, pp. 175-192.
- [44] Aichele, M., and Baschnagel, J., 2001, "Glassy Dynamics of Simulated Polymer Melts: Coherent Scattering and Van hove Correlation Functions. Part I:

- Dynamics in the Beta-relaxation Regime,” *European Physical Journal E*, **5**, pp. 229-242.
- [45] Tschöp, W., Kremer, K., Batoulis, J., Bürger, T., and Hahn, O., 1998, “Simulation of Polymer Melts: I. Coarse-graining Procedure for Polycarbonates,” *Acta Polymerica*, **49**, pp. 61-74.
- [46] Tschöp, W., Kremer, K., Hahn, O., and Batoulis, J., 1998, “Simulation of Polymer Melts: II. From Coarse-grained Models Back to Atomistic Description,” *Acta Polymerica*, **49**, pp. 75-79.
- [47] Marrink, S.J., Risselada, H.J., Yefimov, S., Tielman, D.P., and de Vries, A.H., 2007, “The MARTINI Force Field: Coarse Grained Model for Biomolecular Simulations,” *Journal of Physical Chemistry B*, **111**(27), pp. 7812-7824.
- [48] Monticelli, L., Kandasamy, S.K., Periole, X., Larson, R.G., Tieleman, D.P., and Marrink, S.J., 2008, “The MARTINI Coarse-grained Force Field: Extension to Proteins,” *Journal of Chemical Theory and Computation*, **4**, pp. 819-834.
- [49] Mayo, S.L., Olafson, B.D., and Goddard, W.A., 1990, “Dreiding: A Generic Force-Field for Molecular Simulations,” *Journal of Physical Chemistry* **94**(26), 8897-8909.
- [50] Chakrabarty, A., and Çagin, T., 2008, “Coarse Grain Modeling of Piezoelectric Polyimide Copolymers,” *Proceedings of the Multiscale Materials Modeling Conference 2008*, October 27-31, Tallahassee, FL, pp. 645-650.
- [51] Sperling, L.H., 2001, *Introduction to Physical Polymer Science*, Third Edition, Wiley-Interscience, New York.

- [52] Winger, M., Trzesniak, D., Baron, R., and van Gunsteren, W., 2009, "On Using a Too Large Integration Time Step in Molecular Dynamics Simulations of Coarse-Grained Molecular Models," *Phys. Chem. Chem. Phys.*, **11**(12), pp 1934-1941.
- [53] Texas A&M Supercomputing Facility, "Basic System Information," accessed in December 2009.  
<http://sc.tamu.edu/help/hydra/sysinfo.php>
- [54] Bobisud, L., 1967, "Speed on Energy Propagation for Parabolic Equations," *Illinois J. Math.*, **11**(1), pp. 111-113.
- [55] Polsky, Y., 1994, "Heat Conduction for Dielectric Thin Films from the Casimir to the Diffusion Limit," M.S. thesis, Rice University, Houston , TX.
- [56] Cattaneo, C.R., 1958, "Sur Une de l'équation de la Chaleur Éliminant le Paradoxe d'une Propagation Instantanéé," *Compte. Rend.*, **247**(4), pp. 431-433
- [57] Tzou, D.Y., 1989, "Shock Wave Formation Around A Moving Heat Source in A Solid with Finite Speed of Heat Propagation," *International Journal of Heat and Mass Transfer*, **32**(10), pp. 1979-1987.
- [58] Klemens, P.G., 1951, "The Thermal Conductivity of Dielectric Solids at Low Temperatures (Theoretical)," *Proceedings of the Royal Society of London, Series A, Mathematical and Physical Sciences*, **208**(1092), pp. 108-133.
- [59] Flik, M.I., and Tien, C.L., 1990, "Size Effect on the Thermal Conductivity of High-Tc Thin-Films Superconductors," *Journal of Heat Transfer*, **112**, pp. 872-881.

- [60] Majumdar, A., 1993, "Microscale Heat Conduction in Dielectric Thin-Films," *Journal of Heat Transfer*, **115**(1), pp. 7-16.
- [61] Heino, P., 2009, "Simulations of Nanoscale Thermal Conduction," *Microsyst. Technol.*, **15**, pp. 75-81.
- [62] Xue, H., and Shu, C., 1999, "Equilibration of Heat Conduction Simulation in a Very Thin Film Using Molecular Dynamics," *International Journal of Numerical Methods for Heat and Fluid Flow*, **9**(1), pp. 60-71.
- [63] Che, J., Cagin, T., Deng, W., and Goddard, W., 2000, "Thermal Conductivity of Diamond and Related Materials from Molecular Dynamics Simulations," *Journal Of Chemical Physics*, **113**(16), pp. 6888-6900.
- [64] Che, J., Cagin, T., and Goddard, W., 2000, "Thermal Conductivity of Carbon Nanotubes," *Nanotechnology* **11**, pp. 65-69.
- [65] Shiba, H., and Ito, N., 2008, "Anomalous Heat Conduction in Three-Dimensional Nonlinear Lattices," *Journal of the Physics Society of Japan*, **77**(5), 054006, pp. 1-8.
- [66] Bugel, M., and Galliero, G., 2008, "Thermal Conductivity of the Lennard-Jones Fluid: An Empirical Correlation," *Chemical Physics*, **352**, pp. 249-257.
- [67] Kim, B.H., Beskok, A., and Cagin, T., 2009, "Molecular Dynamics Simulation of the Thermal Resistance at the Liquid-solid Interface," *Journal of Chemical Physics*, **129**, 174701, pp. 1-9.
- [68] Henry, A., and Chen, G., 2009, "Anomalous Heat Conduction in Polyethylene Chains: Theory and Molecular Dynamics Simulations," *Physical Review B*, **79**, 144305, pp. 1-10.

- [69] McGaughey, A.J., and Kaviany, M., 2004, “Thermal Conductivity Decomposition and Analysis Using Molecular Dynamics Simulations: Part II. Complex Silica Structures,” *International Journal of Heat and Mass Transfer*, **47**, pp. 1799–1816.
- [70] Müller-Plathe, F., and Reith, D., 1999, “Cause and Effect Reversed in Non-equilibrium Molecular Dynamics: An Easy Route to Transport Coefficients,” *Computational and Theoretical Polymer Science*, **9**, pp. 203-209.
- [71] Kim, I., 2007, “Experimental Investigation of the Size Effect on Thermal Conductivity for Ultra-Thin Amorphous Poly(Methyl-methacrylate) (PMMA) Films,” M.S. thesis, Texas A&M University, College Station, TX.



## APPENDIX

### Introduction

This appendix consists of a literature survey on recent experimental investigations that were not cited on the main body of the dissertation. Few early experimental works, numerical simulations and three topical reviews were also included in this survey. The appendix begins with a summary of findings followed by a set of tables pointing to relevant results from the individual investigations; specifically, results on the glass transition temperature, density, thermal properties and some other topics of interest in the field of research of polymeric thin-films. Representative plots from selected investigations are included for quick reference. The list of references cited is presented at the end of the appendix.

### Summary

In the mid 1990's few investigators found that the glass transition temperature ( $T_g$ ) of thin polymers films changed as the thickness of the film reduced to the sub-micron scale. Further experiments from several sources confirmed that, in general, when the thickness of a supported polymer film reduces below a critical value the  $T_g$  of the film increases whenever the film and substrate have a strong interaction, and reduces when the film has a weak interaction with the substrate or when the film is freely-standing.

In the particular case of PMMA films spin coated over a silicon wafer, several investigations showed that  $T_g$  increases as film thickness reduces when the silicon has a

native oxide layer [7, 12, 13]. In the other hand when the silicon wafer is treated, for example with hexamethyldisilazane (HMDS) [12] or when the substrate is Al or Au [1, 3, 5, 10], a reduction in the  $T_g$  is observed. The same phenomenon is observed in freely standing films [11]. A number of theories have been proposed to explain this behavior (chain conformation near the substrate, cooperatively rearranging regions and percolation of domains with slow dynamics, among others) and a combination of effects may exist, but the most likely cause of the change of  $T_g$  with thickness are atomic interactions between the polymer and substrate. There is experimental evidence of hydrogen bonds between the carbonyl groups of the PMMA and silica substrates [20], the effect polarity of pendant groups [21] and acid-base interactions [16], which not only affect  $T_g$ , but also the density and even the elastic modulus [26] in the near-wall region. There are also numerical [30] and experimental [19] investigations on the effect of substrate surface roughness on the near wall dynamics of the polymer chains.

Regarding the density of supported polymer films, few investigations had shown that density in the near wall region, approximately 5 nm from the substrate, increases above the bulk value ( $\sim 30\%$ ) when the substrate has a native oxide [15, 16, 20, 21] or a hydrophilic surface [18], but remains constant or decrease slightly ( $\sim 5\%$ ) when the substrate is *cleaned* [17] or hydrophobic [18]. Numerical simulations showed that long chains of random tacticity had less tendency to be packed near the surface as the chain's conformation limits the filling space [24]. In general, the density follows the same trend as the glass transition temperature dependence with the film thickness and nature of the substrate.

A survey on experimental investigations in thermal properties of thin films rendered very few results. The only experimental work on PMMA at the scale of few tens of nanometers is that of Kim, which is referenced in the main body of this dissertation. Experiments on films over 500 nm in thickness [22, 24] had shown thermal conductivity similar to that of bulk PMMA but no change of conductivity with respect to film thickness. An interesting investigation is that of Lee et al. [23] that show a 3-fold increase in the acoustic speed for PMMA films layered over Al-coated silicon and with thickness under 40 nm. However, a similar investigation on PMMA films  $\text{Al}_2\text{O}_3$  substrate showed an increase in wave speed of only 10-20% for films under 60 nm. This is indicative that the acoustic speed, and therefore the thermal conductivity in the length scale of few tens of nanometers is also defined by the nature of the substrate-polymer interaction.

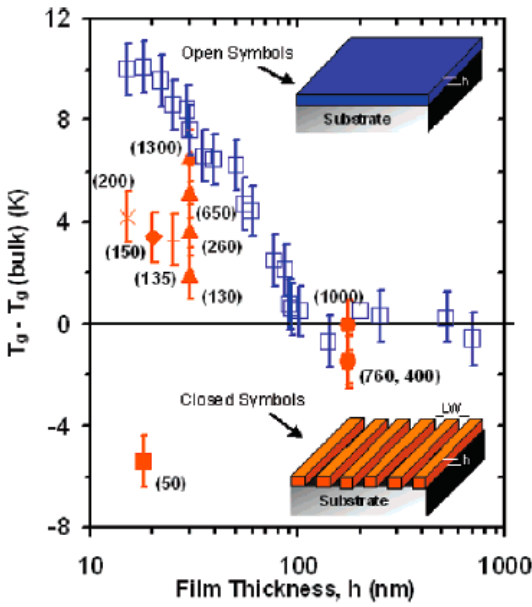
In the numerical model used in this dissertation a Lennard-Jones 12-6 potential, describing the non-bonded Van der Waals forces, represented the substrate-polymer interactions. Even though this potential was calculated using fully-atomistic descriptions, no other interactions (electrostatics, hydrogen bonds, etc.) were included and therefore the nature of the native oxide layer on the silicon wafer is not represented in this model. Moreover, the wall was modeled as a perfectly smooth wall because none of the silicon oxide atoms were included in the simulation domain.

It is expected that results from this dissertation will closely resemble those of experimental investigations on smooth and cleaned silicon surfaces, and not those of PMMA films coated over silicon with native oxide.

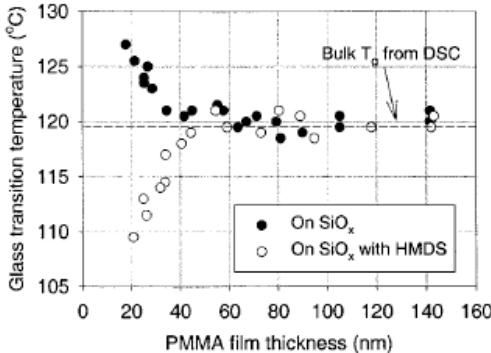
### Glass Transition Temperature

Main author [ref]	Year	Objective of study	Material
	Results relevant to this investigation		
Fukao K. [1]	2005	Aging dynamics in thin PMMA films	Atactic PMMA films spin coated over Al-vacuum deposited glass
	PMMA film with thickness equal to 26 nm showed Tg 7 K below bulk Tg; relaxation stress due to aging reduced with reduced film thickness.		
Tran T.A. [2]	2005	Cooperativity and confinement effects on Tg for nano comp.	PMMA/clay nano composites, ~2 to 140nm nm thick.
	Tg variation is the result of interplay between confinement and surface interactions. Strong interactions like s-PMMA in bentonite or thin films on Si wafers make Tg reduce with film thickness. Weak interaction, like s-PMMA on OMMT composites, make Tg increase		
Fukao K. [3]	2008	Tg and dynamics of thin films by dielectric relax. spectroscopy	PS and PMMA films, 4 to 200 nm thick, over Al substrate
	Tg of all films reduced with thickness. Reduction was ~20 K from bulk Tg and started at thickness 30-25 nm. Reduction was observed in both alpha and beta relaxation processes.		
Lavina S. [4]	2007	Synthesis and electrical properties of composite poly films	PMMA, PCV, m-SiO2 composites
	Tg of PMMA m-SiO2 composites reduced with increasing weight concentration of m-SiO2 from 0 to ~ 25%. Over 25% Tg showed an increasing trend.		
Fukao K. [5]	2003	Dynamics of thin films by dielectric spectroscopy	PMMA and PIP, ~5 to 200 nm thick and different tacticities, on Al substrate
	Reduction of Tg with reduced thickness in both alpha and beta relaxation processes. Alpha relaxation temperature showed dependence on tacticity of PMMA		
Kabomo M. [6]	2007	Effect of mol. mass and surface treatment by DFC and FTIR	Adsorbed PMMA on treated and untreated Cab-O-Sil silica
	Adsorbed PMMA on untreated silica showed higher Tg (by ~30 K). FTIR spectra showed H bonded to surface silanols and free carbonyls. On silica treated with HDMS, Tg's were similar to bulk Tg and independent of molecular mass.		

## Glass Transition Temperature

Main author [ref]	Year	Objective of study	Material
	Results relevant to this investigation		
Mundra M. [7]	2007	Effect of confinement on T <sub>g</sub> of patterned polymer structures	PMMA nanostructures spin coated over oxidized Si substrate
	<p>In PMMA films T<sub>g</sub> showed an increase of up to 10 K at 8 nm thicknesses, with bulk T<sub>g</sub> at 100 nm thickness. A similar trend was observed for nano lines, but it was much less pronounced (even decreased) due to the increase in free surface to substrate ratio. See Figure 3.</p>  <p><b>Figure 3.</b> <math>T_g - T_g(\text{bulk})</math> as a function of film thickness for TC1-labeled PMMA films (open squares) and nanolines with thickness of 175 nm (●), 30 nm (▲), 25 nm (+), 20 nm (◆), 18 nm (□), and 15 nm (×), respectively. The numbers in parentheses specify the line widths (LW). The error bars correspond to the error (<math>\pm 1</math> K) in estimating <math>T_g</math> values by the intersection of linear temperature dependences of integrated intensity in the rubbery and glassy states. The insets show schematics of sample geometries employed for <math>T_g</math> characterization.</p>		
Grohens Y. [8]	2003	Effect of chain conformation and stereo regularity on T <sub>g</sub>	PMMA films, 20 to 150 nm thick, spin coated on silicon substrate
	<p>s-PMMA films showed a reduction of 20 K in T<sub>g</sub> for thickness below 100 nm. i-PMMA showed the opposite trend. Difference in T<sub>g</sub> for s and i-PMMA vanished at 20 nm thickness. The solvent used during spin coating had an effect on the T<sub>g</sub> vs. thickness curves</p>		

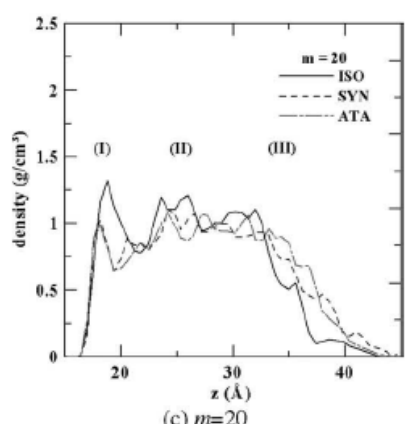
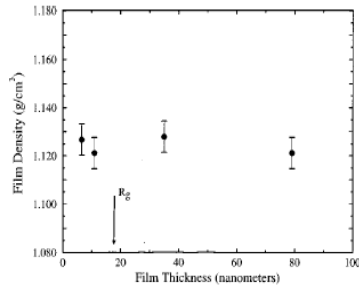
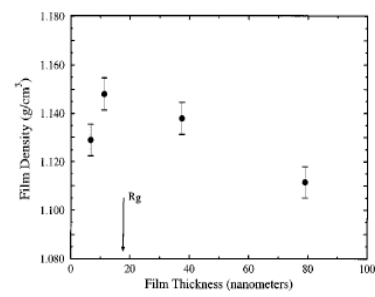
## Glass Transition Temperature

Main author [ref]	Year	Objective of study	Material
	Results relevant to this investigation		
Ash B. [9]	2003	Tg on PMMA/alumina nanocomposites by DSC	PMMA/alumina by free-radical polymerization of MMA in presence of nanoparticles
	Tg reduced 25 K when alumina nanoparticles (17 nm) were added at 0.5 wt % and above. The possible cause is the large mobility created through the addition of nanoparticles with large surface area and poorly bonded to the matrix.		
Shin H.S. [10]	2005	Tg of thin films by principal component analysis from FTIR	i-PMMA and s-PMMA films of 37 and 23 nm spin coated over cleaned Au substrates
	Tg for s and i-PMMA was found to be 60 °C and 110-120 °C respectively, in agreement with bulk values; even though the measurement was in films under 40 nm thickness.		
Roth C.B. [11]	2006	MW dependence of Tg on freely standing thin films	a-PMMA and s-PMMA, 30 to 200 nm thick, free standing
	Tg decreased linearly with film thickness below 100 nm. Tg reduction in high Mw PMMA films is 3 times less than that observed in PS films of similar Mw and thickness.		
Fryer D. S. [12]	2000	Tg as a function of film thickness by thermal probe measurement	PS and PMMA, 20 to 140 nm thick, spin coated over Si with and w/o native oxide
	<p>Strong dependence of Tg as a function of film thickness and presence of native oxide on the Si substrate. See Figure 8.</p>  <p>Figure 8. Plot of the results from local thermal analysis measurements of the <math>T_g</math> of poly(methyl methacrylate) films (<math>M_w = 100.3</math> kg/mol) on substrates of <math>\text{SiO}_x</math> and <math>\text{SiO}_x</math> with HMDS.</p>		

## Glass Transition Temperature

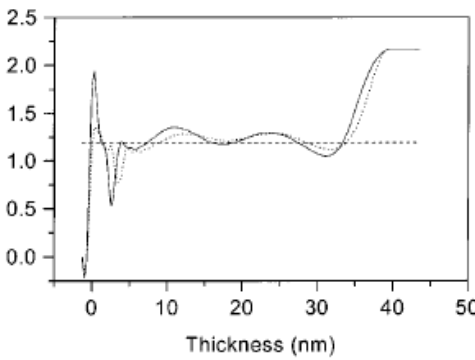
Main author [ref]	Year	Objective of study	Material
	Results relevant to this investigation		
Marceau S. [13]	2006	T <sub>g</sub> as a function of film thickness	a-PS and a-PMMA spin coated over Si with 1-2 nm native oxide
	Strong dependence of T <sub>g</sub> as a function of thickness. As thickness reduced, there was increase in T <sub>g</sub> for PMMA and reduction in T <sub>g</sub> for PS. See figures 3, 5 and 6.		

## Density

Main author [ref]	Year	Objective of study	Material
	Results relevant to this investigation		
Ju S-P. [14]	2009	Effect of chain length and tacticity on conformation	PMMA films with 5, 10, 20 monomers/chain over Au subst.
	<p>Films of PMMA with 20 monomers per chain did not show significant peak density (&lt;20%) near the substrate. Figure 2c shows results for a 4 nm film, substrate on the left.</p>  <p style="text-align: center;">(c) <math>m=20</math></p> <p style="text-align: center;">Fig. 2. Density distributions of the thin films with various chain-lengths.</p>		
Wallace W.E. [15]	1998	Density of PS thin films by twin neutron reflectivity	PS films of 6.5 to 79 nm thick spin coated on H-terminated Si
	<p>No variation of density with film thickness down to 6.5 nm, neither for the hydrogen-terminated silicon nor for the silicon with native oxide. Native oxide thicknesses were measured to be 2 to 3 nm, with roughness from 1 to 1.5 nm. See figures 7 and 8.</p>  <p style="text-align: center;">FIG. 7. Deuterated polystyrene thin film density for the samples on the hydrogen-terminated silicon surface. <math>R_g</math> is the bulk radius-of-gyration, 17.7 nm. The relative uncertainty derives mainly from the fitting procedure (see the text).</p>  <p style="text-align: center;">FIG. 8. Deuterated polystyrene thin film density for the samples on the silicon native-oxide surface. <math>R_g</math> is the bulk radius-of-gyration, 17.7 nm. The additional scatter in the results compared to Fig. 7 derives from the difficulties in fitting the native-oxide layer. The true relative uncertainty in the case is likely to be greater than that shown (see the text).</p>		



## Density

Main author [ref]	Year	Objective of study	Material
van der Lee A. [16]	2001	Density profiles in thin films by X-ray reflectometry	PMMA films, 20 to 70 nm thick, spin coated over Si (111) surfaces with native oxide
	<p>Density of film increased from 1.19 g/cm<sup>3</sup> (bulk PMMA) to 1.9 g/cm<sup>3</sup> (SiO<sub>x</sub>) beginning 5 to 10 nm from the wall, no matter the thickness of the film (smaller films were 20 nm). Acid-base interactions and monomer adhesion might be the causes. Average density might be overestimated. Figure 4 present results for a 35 nm film, substrate on the right.</p>  <p><b>Figure 4.</b> Mass density versus depth for a 35 nm i-PMMA film (full line) and s-PMMA film (dotted line). The dashed straight line represents the bulk density of conventional a-PMMA given as a reference.</p>		
Wu W-L. [17]	1994	Density profiles in thin films by neutron reflectivity	PMMA films, 17 to 62 nm thick, spin coated over Si (111) cleaned surfaces
	<p>A layer of ~5 nm and about half the density of bulk PMMA was observed at the polymer-free surface interface of films before annealing. Layer disappeared after annealing; Density of the films decreased with thickness (~5% in thinnest films). It is argued that films spun from low concentration sol. have 100-fold less entanglements and a restricted space-filling (only in film plane) caused the low density</p>		
Han X. [18]	2009	Effect of polymer-wall interaction in morphology and composition	SEBC/PMMA films spin coated on hydrophilic and hydrophobic substrates
	<p>PMMA segments on the hydrophobic substrate showed little variation across thickness. On hydrophilic surface, PMMA segment density increased near the surface</p>		

## Density

Main author [ref]	Year	Objective of study	Material
	Results relevant to this investigation		
Maire H. [19]	2009	Effect of substrate roughness in domain orientation	Ps-b-PMMA films, 20 to 200 nm thick, spin coated on several substrates
	Vertically oriented micro-domains of PMMA were not observed in the oxide coated Si substrates, probably because the high affinity of the PMMA segments to the surface, even though there were significant differences in the surface roughness of smoothed and roughened SiO <sub>2</sub> substrates.		
Tighilt F-Z. [20]	2007	Interaction of coatings on porous Si by SEM and FTIR	PMMA dip coated, spin coated and spreaded over Si substrate
	Experimental evidence of hydrogen bonds between hydroxyl groups in the porous silicon and the carbonyl groups of PMMA. Morphology of the composite depended on the nature of the solvent and coating technique used.		
Ahn S.I. [21]	2009	Effect of polarity in the surface and interface of thin films	PMMA, P4VP, PS and PAMS films of 20-35 nm spin coated over Si with native oxide
	Electron density (by XRR) near the interface is strongly dependant on the substrate-monomer interaction. A correlation between polarity of polymer pendant groups and surface density is suggested.		

## Thermal Properties

Main author [ref]	Year	Objective of study	Material
	Results relevant to this investigation		
Chu D. [22]	2001	Thermal conductivity of thin film resists	PMMA film spin coated over a SiO <sub>2</sub>
	Using non-contact thermo reflectance, the thermal conductivity of PMMA film of 400 nm thickness was found to be 0.16 W/m_K. The same value was obtained for the in-plane conductivity of a 800 nm film.		
Touzelbaev M.N. [23]	2001	Review of thin film thermal characterization methods	Thin films in general
	Explains theory behind thermo reflectance method, currently the only method to measure conductivity in ultra-thin polymer films		
Kurabayashi K. [24]	1999	Thermal conductivity of Polyimide films	Polyimide films from 500 to 2500 nm thickness spin coated over SiO <sub>2</sub>
	3 Experimental procedures were used to measure through-thickness K, which was found to be independent of thickness. In-plane conductivity, however, was 6 times higher at 500 nm indicating anisotropy in the films.		
Lee Y-C. [25]	1996	Through thickness wave velocity of by picosecond acoustic meas.	PMMA films, 25 to 133 nm thick, spin coated over Al coated Si substrate
	Wave speed increased from 2700 m/s (bulk) at 133 nm to 7000-8000 m/s at 20-25 nm. Increase began sharply at 40 nm thickness. See Figure 3. It is reported that a similar investigation on PMMA films over Al <sub>2</sub> O <sub>3</sub> substrate, increase in wave speed is only 10-20% for films under 60 nm.		

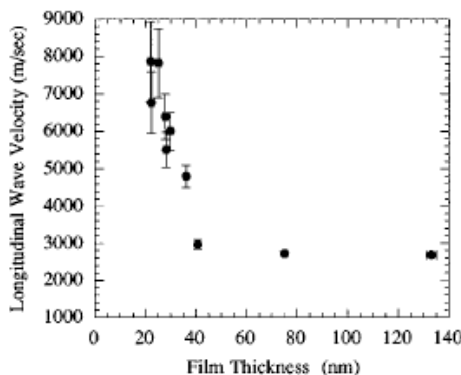
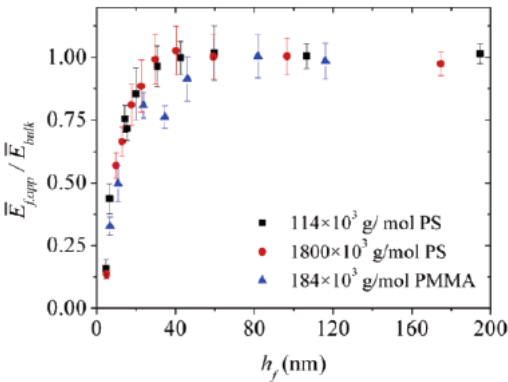


FIG. 3. The measured longitudinal wave velocity of PMMA films.

### Other Relevant Investigations

Main author [ref]	Year	Objective of study	Material
Stafford C. [26]	2006	Elastic moduli of ultra-thin films by buckling-based metrology	PMMA and PS films, 5 to 200 nm thickness, spin coated on Si, transferred to PDMS
	<p>PMMA films of thickness 40 nm and under showed a reduction in elastic modulus. Films of 5 nm showed 1/3 the module of a 80 nm film (or bulk). PS showed a similar trend. See Figure 5.</p>  <p>Figure 5. Reduced modulus (<math>\bar{E}_{app}/\bar{E}_{bulk}</math>) for the two PS (■, ●) and PMMA (▲) materials as a function of thickness (<math>h_f</math>). The error bars represent one standard deviation of the data, which is taken as the experimental uncertainty of the measurement.</p>		
Hideyuki I. [27]	2006	Entanglement of polymer chains in ultra-thin films	PMMA films, 4-88 nm thick, spin coated on quartz substrates
Experimental evidence of entanglement in ultra-thin polymer films, therefore change of properties in ultra-thin films is not due to lack of entanglement during spin coating			
Qi D. [28]	2008	Substrate and chain length dependence of surface dynamics	i-PMMA, ~60 nm thickness, spin coated over Si and Al substrate
The Surface nano-hole relaxation technique was used to study dynamics. Films over Si substrate showed slower surface dynamics (1-3 nm from surface) than films over Al substrate			
Alcoutlabi M. [29]	2005	Effect of confinement on material behavior at nano scale	Polymers in general
A thorough literature review on experimental investigations showing change of polymer properties in nano confinement (films, nano pores, etc.)			

### Other Relevant Investigations

Main author [ref]	Year	Objective of study	Material
		Results relevant to this investigation	
Scheidler P. [30]	2002	Relaxation dynamics near rough and smooth walls	Supercooled liquid of LJ particles
	Rough walls caused slower dynamics, while smooth walls accelerated dynamics in the near-wall region. See Fig. 1.  Fig. 1 – Structural relaxation time $\tau_q(z)$ at $q = 7.2$ as a function of particle distance $z$ from the wall for (a) rough and (b) smooth surface at different temperatures. The large diamonds are the bulk values and the long-dashed lines and the solid ones are fits according to eqs. (1) and (2), respectively.		
Gross S. [31]	2007	PMMA properties, mainly dielectric properties in hybrid films	PMMA
	Summary of investigations in dielectric properties and relaxation behavior of PMMA, both bulk and thin films		

**Appendix References**

- [1] Fukao, K., and Sakamoto, A., 2005, "Aging Phenomena in Poly(methyl methacrylate) Thin Films: Memory and Rejuvenation Effects," *Physical Review E*, **71**, 041803, pp. 1-12.
- [2] Tran, T.A., Said, S., and Grohens, Y., 2005, "Compared Study of Cooperativity in PMMA Nanocomposites and Thin Films," *Composites Part A*, **36**, pp. 461-465.
- [3] Fukao, K., 2008, "Dielectric Behavior of Glass Transition and Dynamics in Thin Films," *Journal of the Rheology Society of Japan*, **36(2)**, pp. 73-80.
- [4] Lavina, S., Negro, E., Pace, G., Gross, S., Depaoli, G., Vidali, M., and Di Noto, V., 2007, "Dielectric Low-k Composite Films Based on PMMA, PVC and Methylsiloxane-silica: Synthesis, Characterization and Electrical Properties," *Journal of Non-Crystalline Solids*, **353**, pp. 2278-2888.
- [5] Fukao, K., 2003, "Dynamics in Thin Polymer Films by Dielectric Spectroscopy," *European Physical Journal E*, **12**, pp. 119-125.
- [6] Kabomo, M.T., Blum, F.D., Kulkeratiyut, S., Kulkeratiyut, S., and Krisanangkura, P., 2008, "Effects of Molecular Mass and surface Treatment on Adsorbed Poly(methyl methacrylate) on Silica," *Journal of Polymer Science Part B*, **46**, pp. 649-658.
- [7] Mundra, M.K., Dunthu, S.K., Dravid, V.P., and Torkelson, J.M, 2007, "Effect of Spatial Confinement on the Glass Transition Temperature of Patterned Polymer Nanostructures," *Nano Letters*, **7(3)**, pp. 713-718.

- [8] Grohens, Y., Hamon, L., Spevacek, J., and Holl, Y., 2003, "The Gel-like Structure of Polymer in Thin Films: An Explanation of the Thickness Dependent Glass-Transition?," *Macromolecular Symposia*, **203**, pp. 155-164.
- [9] Ash, B.J., Siegel, R.W., and Schadler, L.S., 2004, "Glass-Transition Temperature Behavior of Alumina/PMMA Nanocomposites," *Journal of Polymer Science Part B*, **42**, pp. 4371-4383.
- [10] Shin, H.S., Lee, H., Jun, C-H., Jung, Y.M., and Kim, S.B., 2005, "Transition Temperatures and Molecular Structure of Poly(methyl methacrylate) Thin Films by Principal Component Analysis: Comparison of Isotactic and Syndiotactic Poly(methyl methacrylate)," *Vibrational Spectroscopy*, **37**, pp. 69-76.
- [11] Roth, C.B., Pound, A., Kamp, S.W., Murray, C.A., and Dutcher, J.R., 2006, "Molecular-weight Dependence of the Glass Transition Temperature of Freely-standing Poly(methyl methacrylate) Films," *European Physical Journal E*, **20** pp. 441-448.
- [12] Fryer, D.S., Nealy, P.F., and de Pablo, J., 2000, "Thermal Probe Measurements of the Glass Transition Temperature for Ultrathin Polymer Films as a Function of Thickness," *Macromolecules*, **33**(17), pp. 6439-6447.
- [13] Marceau, S., Tortai, J-H., Tillier, J., Vourdas, N., Gogolides, E., Partis, I., Beltsios, K., and van Werden, K., 2006, "Thickness-dependent Glass Transition Temperature of Thin Resist Films for High Resolution Lithography," *Microelectronic Engineering*, **83**, pp. 1073-1077.

- [14] Ju, S-P., Liao, M-L., Cheng, C-H., Lee, W-J., and Chang, J-G., 2009, "Chain-Length and Tacticity Effects on the Conformational Behavior of MMA-oligomer Thin Films on an Au (111) Substrate," *Computational Materials Science*, **45**, pp. 867-874.
- [15] Wallace, W.E., Beck Tan, N.C., and Wu, W.L., 1998, "Mass Density of Polystyrene Thin Films Measured by Twin Neutron Reflectivity," *Journal of chemical Physics*, **108**(9), pp. 3798-3804.
- [16] van der Lee, A., Hamon, L., Holl, Y., and Grohens, Y., 2001, "Density Profiles in Thin PMMA Supported Films Investigated by X-ray Reflectometry," *Langmuir*, **17**(24), pp. 7664-7669.
- [17] Wu, W-L., Orts, W.J., van Zanten, J.H., and Fanconi, B.M., 1994, "Density Profile of Spin Cast Polymethylmethacrylate Thin Films," *Journal of Polymer Science Part B*, **32** pp. 2475-2480.
- [18] Han, X., Dai, Y., Huang, Y., and Liu, H., 2009, "Effect of Polymer-substrate Interactions on the Surface Morphology of Polymer Blend Thin Films: Comparison Between Simulations and Experiment," *Journal of Macromolecular Science Part B*, **48**(4), pp. 723-735.
- [19] Maire, H. C., Ibrahim, S., Li, Y., and Ito, T., 2009, "Effects of Substrate Roughness on the Orientation of Cylindrical Domains in Thin Films of A Polystyrene-Poly(methylmethacrylate) Diblock Copolymer Studied Using Atomic Force Microscopy and Cyclic Voltammetry," *Polymer*, **50**(8), pp. 2273-2280.



- [20] Tighilt, F-Z., Gabouze, N., Sam, S., Belhousse, S., and Beldjilali, K., 2007, "Morphology and Specific Interaction of PMMA Coating with the Surface of Porous Silicon," *Surface Science* **601**, pp. 4217-4221.
- [21] Ahn, S.I., Kim, J-H., Kim, J. H., Jung, J. C., Chang, T., Ree, M., and Zin, W-C., 2009, "Polarity Effect Near the Surface and Interface of Thin Supported Polymer Films: X-ray Reflectivity Study," *Langmuir*, **25**(10), pp. 5667-5673.
- [22] Chu, D., Touzelbaev, M., Goodson, K.E., and Pease, F., 2001, "Thermal Conductivity Measurements on Thin-Film Resist," *Journal of Vacuum Science Technology B*, **19**(6), pp. 2874-2877.
- [23] Touzelbaev, M.N., and Goodson, K.E., 2001, "Impact of Experimental Timescale and Geometry on Thin-Film Thermal Property Measurements," *International Journal of Thermophysics*, **22**(1), pp. 243-263.
- [24] Kurabayashi, K., Asheghi, M., Touzelbaev, M.N., and Goodson, K.E., 1999, "Measurement of the Thermal Conductivity Anisotropy in Polyimide Films," *Journal of Electromechanical Systems*, **8**(2), pp. 180-191.
- [25] Lee, Y-C., Bretz, K.C., Wise, F.W., and Sasche, W., 1996, "Picosecond Acoustic Measurement of Longitudinal Wave Velocity of Submicron Polymer Films," *Applied Physics Letters*, **69**(12), pp. 1692-1694.
- [26] Stafford, C.M., Vogt, B.D., Harrison, C., Julthongpiput, D., and Huang, R., 2006, "Elastic Moduli of Ultrathin Amorphous Polymer Films," *Macromolecules*, **39**(15), pp. 5095-5099.

- [27] Itagaki, H., Nishimura, Y., Sagisaka, E., and Grohens, Y., 2005, "Entanglement of Polymer chains in Ultrathin Films," *Langmuir*, **22**(2), pp. 742-748.
- [28] Qi, F., Fakhraai, Z., and Forrest, J.A., 2008, "Substrate and Chain Size Dependence of the Near Surface Dynamics of Glassy Polymers," *Physical Review Letters*, **101**(9), 096101 pp. 1-4.
- [29] Alcoutlabi, M., and McKenna, B., 2005, "Effects of Confinement on Material Behaviour at the Nanometre Size Scale," *Journal of Physics: Condensed Matter*, **17**(15), pp. R461-R524.
- [30] Scheidler, P., Kob, W., and Binder, K., 2002, "Cooperative Motion and Growing Length Scales in Supercooled Confined Liquids," *Europhysics Letters*, **59**(5), pp. 701-707.
- [31] Gross, S., Camozzo, D., Di Noto, V., Armelao, L., and Tondello, E., 2007, "PMMA: A Key Macromolecular Component for Dielectric Low-k Hybrid Inorganic-organic Polymer Films," *European Polymer Journal*, **43**(3), pp. 673-696.

**VITA**

Name: Carlos Ardenis Silva Hernandez

Address: FMC Technologies Inc.  
11220 TC Jester  
Houston, TX 77067

Email Address: carlos.silva2 @fmcti.com

Education: B.S., Mechanical Engineering, IUPFAN, Venezuela, 1994  
M.S., Mechanical Engineering, Texas A&M University, USA, 2005  
Ph.D., Mechanical Engineering, Texas A&M University, USA, 2010